Characterisation of monolithic tandem solar cells containing strain balanced quantum well sub-cells

Andreas Ioannides

Imperial College London
Department of Physics

Submitted for the degree of Doctor of Philosophy

April 2015

Contents

1 Introduction to Photovoltaics **15**

1.1 EU policy and renewable energy goals 15
1.2 Current status of PV in Europe 16
1.3 Technology and Market Trends 16
1.4 PV cost and Third Generation PV 18
1.5 Solar Cell Basics 20
1.5.1 Dark Current 22
1.5.2 Photocurrent 22
1.5.3 Power and Efficiency 23
1.5.4 Parasitic Resistance Effects 25
1.5.5 Bandgap Effect on Efficiency 27
1.5.6 Solar Spectra 28
1.6 Practical Photovoltaics 31
1.6.1 Window layers 31
1.6.2 Cap layers and Metal Contacts 31
1.6.3 Back Surface Fields 32
1.6.4 Anti-Reflection Coatings 32
1.7 Quantum Well Solar Cells 32
1.7.1 Multi-Quantum Well Structures 33
1.7.2 Strain Balanced MQW Solar Cells 34
1.8 Multi-junction Solar Cells 35
1.8.1 Dual Junction Solar Cells 35
1.8.2 Multi-junction Structure Types 36
1.8.3 Tunnel Junctions 38
1.8.4 MQW multi-junction cells 39
1.9 Objectives of Thesis 41

2 Solar Cell Device Processing **46**
2.1 Wafer cleaning and front metal deposition 46
2.2 Front Contact Photolithography 47
2.2.1 Photoresist Profile 48
2.3 Gold Electrodeposition 48
2.4 Gold and Platinum Dry Etch 50
2.5 GaAs Cap Etch 51
2.6 Anti-Reflection Coat Deposition 51
2.7 Opening for Electrical Contact 52
2.8 Device Isolation (Mesa Etch) 52
2.8.1 Two Step Selective Mesa Etches 52
2.8.2 Isotropic Non-selective Mesa Etch 53
2.9 Back Surface Contact Deposition 53
2.10 Rapid Thermal Annealing and Device Separation 54
2.11 Device Mounting 54
2.11.1 Photodiodes and Fully Metallized Devices 54
2.11.2 Concentrator Devices Mounting 55
2.12 Summary of processing 55

3 Multi-junction MQW Solar Cell Characterisation **62**
3.1 Introduction 62
3.2 Dark Currents Measurements 62
3.3 External Quantum Efficiency Measurements 63
3.4 Reflectivity Measurements 66
3.5 Light I-V measurements 67
3.5.1 Dual Monochromatic Characterisation 67
3.5.2 Xenon Source Characterisation 69
3.6 Electroluminescence 70

4 Device Modelling **73**
4.1 Introduction to SOL 73
4.2 Quantum Efficiency Modelling 74
4.2.1 IQE Modelling of p- and n-regions 74
4.2.2 QE Modelling of i-region 75
4.3 Dark Current Modelling 77
4.3.1 Dark Current in the depletion region 78
4.3.2 Radiative Dark Current 78
4.3.3 Ideal Shockley Dark Current 80

4.4 Tandem Cell Modelling 81
4.5 Conclusions 83

5 Tandem Cell Results **87**
5.1 Device overview 89
5.2 Preliminary Devices 90
5.3 Top cell enhancement 94
5.4 Sheffield grown top cell 98
5.4.1 Top cell growth on Silicon substrate TS131-Si 98
5.4.2 Top cell growth on GaAs substrates 99
5.5 Current matched devices 102
5.6 QE Modelling 103
5.7 Dark Current Comparison & Modelling 104
5.8 Efficiency Results & Modelling 104
5.9 Conclusions 107

6 Concentrator Optics Design **110**
6.1 Concentrator System Overview 110
6.2 Preliminary Designs 112
6.2.1 ZEMAX light source and detector parameters 113
6.2.2 Buffon Concentrator Lens 114
6.3 Optimised Buffon Lens 117
6.3.1 Optimised 'Blank' Lens 117
6.3.2 Step Side Angle Optimisation and Tolerances 118
6.3.3 Cell Position Effects 119
6.3.4 Lens Dimensions Tolerances 119
6.3.5 Light Distribution 121
6.4 Waveguide Design 121
6.4.1 Waveguide Modelling 122
6.4.2 Experimental Results 127
6.5 Conclusions 128

7 Conclusions **132**

Appendix A List of Publications **134**

Appendix B Device Descriptions & Modelling Parameters 136
B.1 Preliminary Devices 136
B.2 MQW Tandem Solar Cells 141
B.3 Control Devices 145
B.4 Top Cell only Devices 148

List of Figures

1.1 Historical Development of Global cumulative PV power installed per Region [1]. 17
1.2 Solar module retail price index [5]. 19
1.3 Efficiency and cost projections for first, second and third generation photovoltaic technology [6]. 20
1.4 Electron promotion by light absorption in semiconductors. . . 21
1.5 Absorption and recombination mechanisms in p-n junctions. . 21
1.6 Typical light I-V curve. 24
1.7 Solar cell equivalent circuit with parasitic resistances. 25
1.8 Parasitic resistance effects on dark current. 26
1.9 Parasitic resistance effects on light IV characteristic curve. . . 27
1.10 Efficiency limit as a function of bandgap at 30x and 1000x concentration levels [8]. 28
1.11 Solar spectrum variation over the course of a day. 29
1.12 Standard solar spectra as defined in ASTM G-173 standard. . 30
1.13 Energy gap vs lattice constant for some common elementary and binary semiconductors [14]. 34
1.14 Absorption of AM1.5g spectrum by a dual junction cell 36
1.15 Optimum band gap combinations contour plot for dual junction cells under AM1.5 spectrum. Intersecting black lines depict lattice matched InGaP/GaAs tandem. The predicted efficiency of a Strain Balanced Quantum Well Solar Cell (SB-QWSC) is also depicted. 37
1.16 An idealised cascade two junction solar cell band diagram [23]. 39

1.17 (a) Static current-voltage characteristics of a typical tunnel diode. I_p and V_p are the peak current and peak voltage. I_v and V_v are the valley current and valley voltage. (b) The total static characteristics are broken down into three components [14]. 40

2.1 Photoresist profiles. 49
2.2 Gold contacts resulting from different deposition rates on samples developed by the author. 50
2.3 Processing steps. 59

3.1 Experimental setup for multi-junction cell external quantum efficiency measurements. 64
3.2 Reflectivity measurement setup. 66
3.3 Xenon arc lamp spectrum. 69
3.4 Electroluminescence images of concentrator cells. Darker patches denote poor absorption or high losses. 71

4.1 Effect of diffusion lengths and surface recombination on p- and n-regions. The total QE depicted is the SOL model output based on the growth details of device Qt1821AD. The contribution of each region is depicted and the model prediction for various diffusion lengths and surface recombination. 76
4.2 Dark current fitting of the low bias region ($n \approx 2$) based on one parameter fit. Fitting based on TS151 data and fitting parameters with $R_{s=0}\Omega$. 79
4.3 Energy band edge diagram of a p-i-n QWSC [7]. 80
4.4 Measured and modelled tandem cell external quantum efficiencies of device Qt1808U. 82
4.5 Tandem cell modelled dark current. Experimental data and model based on device TS151. 83

5.1 Device development cycle 88
5.2 Qt1808U Device Structure. 91
5.3 Qt1808U experimental and modelled Quantum Efficiency. . . . 92
5.4 ENE1595.4 External Quantum Efficiency and corresponding modelled top cell. 95
5.5 Qt1821AD External Quantum Efficiency and corresponding modelled top cell. 96

5.6 Internal Quantum Efficiency of samples Qt1821AD, ENE1595.4 and Qt1808U. Shaded region depicts decrease in QE of Qt1821AD as compared to ENE1595.4 97
5.7 Images of TS131-Si wafer during processing. 99
5.8 Experimental QE of devices TS131-alpha and TS131-beta. . . 100
5.9 SOL model of TS131alpha-5 QE. 101
5.10 Internal QE Comparison of devices TS131alpha-5, Qt1821AD, Qt884D-6 and ENE1595.4. 101
5.11 Experimental QE of devices TS151 and ENE1864.1. 102
5.12 Top cell band edge dependence on substrate material and orientation. 103
5.13 QE Modelling of TS151. 104
5.14 QE Modelling of Qt1821AD. 105
5.15 Dark Current Modelling of TS151. 105
5.16 Dark Current Modelling of Qt1821AD. 106
5.17 Efficiency comparison of TS151 and ENE1864. 107
5.18 Efficiency prediction from SOL Modelling. 108

6.1 Solar window concentrator system concept. 112
6.2 Modified AM1.5g Spectrum as used in ZEMAX. 114
6.3 Preliminary concentrator lens designs. (a) Four even step design (b) Fourteen even step design (c) Forty-two even step design (d) Fourteen uneven step design 116
6.4 Output images for (a) four even step, (b) fourteen even step, (c) forty-two even step and (d) fourteen uneven step designs. . 117
6.5 Effect of image position on output efficiency 120
6.6 Output images (a) with lens alone and (b) with 15mm waveguide. 121
6.7 Waveguide ZEMAX model setup. 122
6.8 Ray tracing diagrams of waveguide with vertical displacements of (a) 0.0mm and (b)-0.1mm at 60° rotation. 124
6.9 Total internal reflection losses at exit side of waveguide. 125
6.10 Experimental setup for F2 glass waveguide characterisation. . 128
6.11 Experimental output efficiencies for a 52mm, F2 glass waveguide. 129

List of Tables

5.1 Summary of fabricated devices. 89
5.2 Preliminary Devices. 90
5.3 Summary of Jsc for AM1.5g and AM0 spectra. 93
5.4 Tandem Cell Efficiencies under simulated AM1.5g spectrum. . 93
5.5 Tandem Cell Efficiencies under simulated AM0 spectrum. . . . 94
5.6 Top cell models with varied intrinsic region thickness compared to Qt1808U top cell IQE current density. 94
5.7 AM1.5g top cell short circuit current density comparison. . . . 96
5.8 Measured efficiencies for 15 finger concentrator device Qt1821AD using flash tester (AM1.5g spectrum). 98
5.9 TS131 Top cell samples growth details. 99

6.1 Summary of preliminary concentrator Buffon lens designs. . . 115
6.2 Efficiency contribution when having the step side at angle. . . 118
6.3 Efficiency change with No. 2 step side angle change. 119
6.4 Concentrator output efficiencies for PMMA waveguide. 123
6.5 Concentrator output efficiencies for PMMA waveguide with -0.1mm displacement. 124
6.6 Concentrator output efficiencies with PMMA waveguide with -0.1mm displacement and detector inside the waveguide 126
6.7 Concentrator system efficiencies with F2 glass waveguide. . . . 126
6.8 Concentrator system output efficiencies for various lengths of F2 glass waveguide. 127

B.1 Qt1772AD device structure. 137
B.2 Qt1772AD modelling parameters. 137
B.3 Qt1772AU device structure. 138
B.4 Qt1772AU modelling parameters. 138
B.5 Qt1772BD device structure. 139

B.6 Qt1772BD modelling parameters. 139
B.7 Qt1772BU device structure. 140
B.8 Qt1772BU modelling parameters. 140
B.9 Qt1808U device structure. 141
B.10 Qt1808U modelling parameters. 142
B.11 Qt1821AD device structure. 142
B.12 Qt1821AD modelling parameters. 143
B.13 TS151 device structure. 143
B.14 TS151 modelling parameters. 144
B.15 ENE1595.4 device structure. 145
B.16 ENE1595.4 modelling parameters. 146
B.17 ENE1864 device structure. 146
B.18 ENE1864 modelling parameters. 147
B.19 TS131 device structure. 148
B.20 TS131 modelling parameters. 148

Declaration of Originality

I hereby declare that this thesis is my own work and that all else is appropriately referenced.

Copyright Declaration

The copyright of this thesis rests with the author and is made available under a Creative Commons Attribution Non-Commercial No Derivatives licence. Researchers are free to copy, distribute or transmit the thesis on the condition that they attribute it, that they do not use it for commercial purposes and that they do not alter, transform or build upon it. For any reuse or redistribution, researchers must make clear to others the licence terms of this work.

Acknowledgements

Over the course of my work I was fortunate to be surrounded by people whose support and contribution was invaluable in both my academic and personal endeavours.
I would like to express my gratitude to Keith, firstly for giving me the opportunity and privilege to work under his wings and secondly for always going beyond of what is expected for PhD supervision. His enthusiastic approach and positive attitude has kept me going even at times of crisis.
To James Connolly for his contribution to my theoretical understanding and his willingness to help whenever needed. Many thanks go to Ian Ballad for his extraordinary help in the lab. To Tom Tibbits for introducing me to the wonderful world of semiconductor processing and just for being 'shebab'. I would like to thank Dan, Markus, Marianne, Dave, Rahul and Ben for being such a wonderful group both in and out of college.
Special thanks to Massimo Mazzer for all his contributions and supervision. Thanks to Barry Clive of Optical Products for all his ideas on the concentrator system.
Without the samples and contribution of the staff at EPSRC National Center for III-V Technologies and in particular John Roberts, Geoff Hill and Rob Airey, none of this would be possible. I would like to thank all the staff at CIP for all their invaluable processing help.
Guy Smekens and Jose Van Begin for all the top cell overgrowth and their support in the characterisation process.

This thesis is dedicated to my parents and my wife, Marilena for their unconditional love and never-ending support.

Abstract

This thesis presents the milestone efficiency of 30.6% under 54x concentration achieved by a monolithic tandem solar cell containing strain balanced quantum well sub-cells. This is the first demonstration of tandem cells containing quantum well sub-cells. Characterisation and modelling of the quantum efficiency and dark currents of monolithic tandem cells containing quantum well sub-cells are also presented for the first time. Predictions performed by a simulation program indicate that 32.3% efficiency at 500x concentration can be achieved and in combination with an active Ge substrate efficiencies of 37.5% are possible. The model created in the simulation program is presented which makes possible the accurate fitting of quantum efficiency and prediction of dark current. The procedure developed to process tandem solar cells into concentrator devices is presented. A detailed account of the characterisation methods used for tandem solar cells are also described. Going further, a new optical concept for building integrated PV design was examined in this thesis. The design is based on a Buffon lens as an alternative to convex and Fresnel lens designs. The low cost design presented can be accommodated in the space of a double glazing window for glass facades.

Chapter 1

Introduction to Photovoltaics

Over the last decade photovoltaics have established themselves as the leading market in the field of renewables with a strong presence in the small scale domestic sector. From an emerging market in the late nineties the total global installed PV capacity by 2013 is estimated at 139GW [1]. Over 160TWh of solar electricity is produced each year, equivalent to 32 large coal power plants capable of supplying 45 million households. This goes to prove that PV has crossed the threshold from being an eco-warrior and an alternative source of energy to a dependable solution and a mainstream market.

1.1 EU policy and renewable energy goals

The 1997 Kyoto Protocol on climate change has committed the world's industrial nations to reduce their Green House Gas (GHG) emissions by 5.2% from 1990 levels. The European Union, under the Protocol, has committed itself to reduce the GHG emissions by 8%. Prior to the Kyoto summit the EU published the White Paper on Renewable Energy Sources upon which a target for renewable energy sources was set to 12% of the energy consumption to be reached by 2010 [2]. In the continuous re-assesment of targets set by the EU, Directive 2001/77/EC defined that by the year 2010 a total of

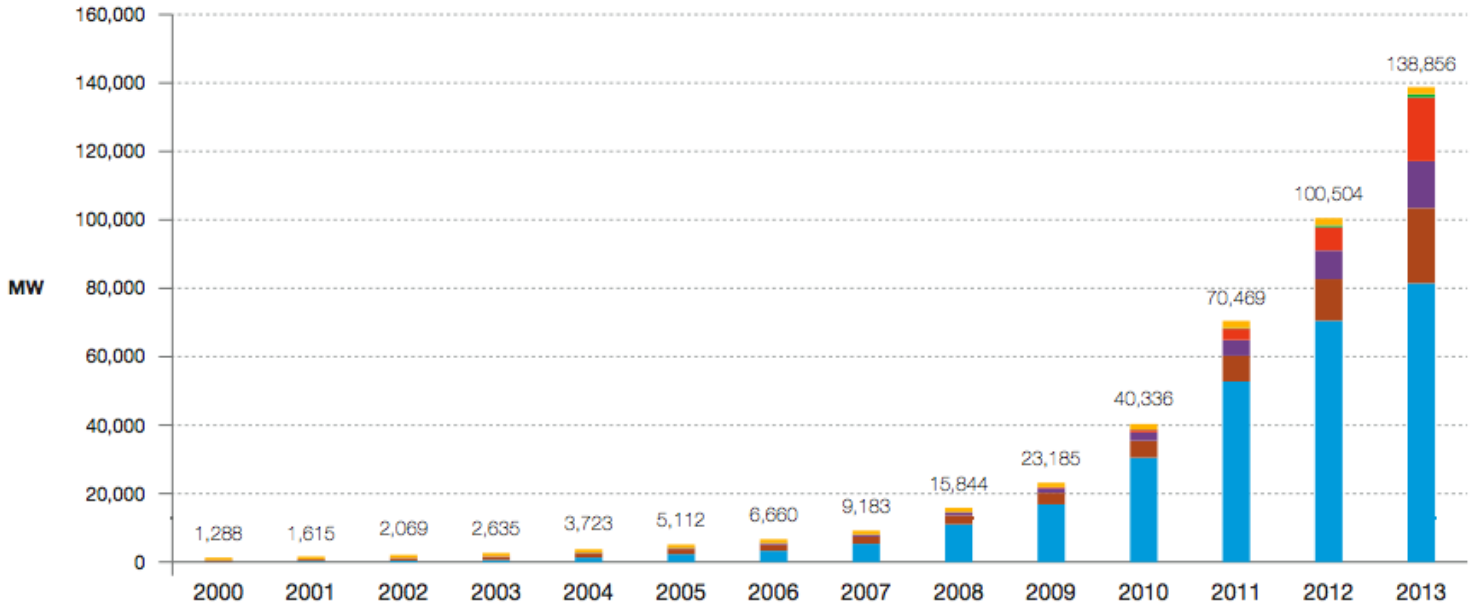
22% of the electricity production should be from renewable energy sources setting also the national indicative targets. In 2009 the Renewable Energy Directive 209/28/EC redifined the targets to 20% reduction in greenhouse gas emissions and 20% renewable energy of end user consumption. Following these the Republic of China on the 28th February 2005 endorsed the Renewable Energy law by which renewable energies should cover 10% of the energy consumption in China by the year 2020 [3]. The notion of renewable energy was finally put into effect, although the United States of America have not agreed to uphold the Kyoto Protocol.

1.2 Current status of PV in Europe

Following the photovoltaic Spanish market boom of 2008 over the subsequent years the current total installed PV capacity has reached 81.5GWp, which represents approximately 59% of the Global installed capacity as can be seen in Figure 1.1. Over the last three years however the annual installed power is decreasing with only 11GW installed in 2013 compared to 17.7GW in 2012 and 22.4GW in 2011. The current stable prices, caused mainly due to imposing anti-dumping and anti-subsidy levies on Chinese produced modules and cells, and the drastic reduction of subsidies since 2009 in Germany the European market has declined over the last three years. According to the European Photovoltaic Industry Association (EPIA) 'moderate scenario' (scenario based on 'business as usual' without a major change in subsidy policies) further shrinking of the market is expected with a steady positive outlook from 2016 onwards [1].

1.3 Technology and Market Trends

The major technology player in the PV market has remained silicon and in particular polycrystalline silicon modules. During late 2008 and early 2009



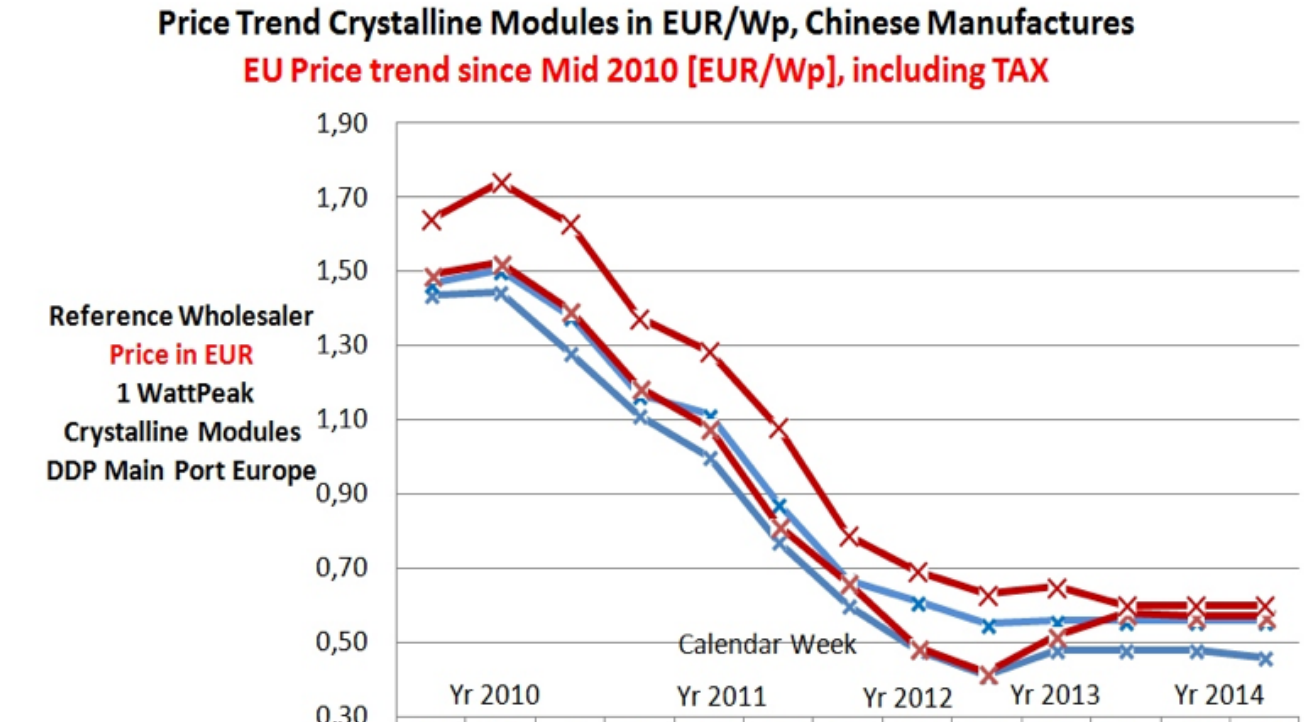
	2000	2001	2002	2003	2004	2005	2006	2007	2008	2009	2010	2011	2012	2013
RoW	751	807	887	964	993	1,003	1,108	1,150	1,226	1,306	1,590	2,098	2,098	2,098
MEA	n/a	n/a	n/a	n/a	1	1	1	2	3	25	80	205	570	953
China	19	24	42	52	62	70	80	100	140	300	800	3,300	6,800	18,600
Americas	21	24	54	102	163	246	355	522	828	1,328	2,410	4,590	8,365	13,727
APAC	368	496	686	916	1,198	1,502	1,827	2,098	2,628	3,373	4,951	7,513	12,159	21,992
Europe	129	265	399	601	1,306	2,291	3,289	5,312	11,020	16,854	30,505	52,764	70,513	81,488
Total	**1,288**	**1,615**	**2,069**	**2,635**	**3,723**	**5,112**	**6,660**	**9,183**	**15,844**	**23,185**	**40,336**	**70,469**	**100,504**	**138,856**

Figure 1.1: Historical Development of Global cumulative PV power installed per Region [1].

the PV world had seen the rise of numerous start-up companies in the thin-film PV sector with an estimate of $8.4 billion of venture capital being secured [4]. The following financial crisis caused a halt in this emerging technology with a lot of start-up companies closing and most struggling to secure funds in order to ensure financial survival. However a steady re-growth of the thin-film industry has led to 20% of PV production to be thin-film technology in 2012.

1.4 PV cost and Third Generation PV

Several companies that have invested in multi-junction solar cell concentrator technologies currently have a number of modules commercially available. The cost still remains prohibitive compared to mainstream market technologies. Prices had a sharp decreasing trend but this was due to the sudden emergence of China as major producer leading to oversupplies. The anti-dumping and anti-tariff levies imposed both by the U.S. Government and E.U. have halted the prices to a steady level since 2013. The average price per Watt has decreased since 2010 to over 60%. Figure 1.2 below depicts the retail price index for modules in Europe by Chinese manufacturers from 2010 to 2014. Further prices decreases are not expected however and the module cost is now a small part of the system costs therefore price reduction can only be achieved through an efficiency increase. As depicted in Figure 1.3 below in order to achieve lower costs per Watt the technology trend needs to shift to next generation PV with higher efficiencies [6]. High efficiencies are only offered by 3rd generation PV known as concentrator photovoltaics (CPV). The union of high efficiency multi-junction PV with cheap concentrating optics offers the most cost effective solution. This thesis describes the first examples of a novel 3rd generation CPV cell: the multi-junction quantum well solar cell.



	36	42	2	14	17	38	2	32	3	20	51	17	35
Min Price Non Bankable, EUR/W	1,44	1,44	1,28	1,11	1,00	0,77	0,60	0,48	0,41	0,48	0,48	0,48	0,46
Max Price Non Bankable, EUR/W	1,47	1,50	1,38	1,17	1,11	0,87	0,67	0,61	0,55	0,56	0,56	0,56	0,56
Min Price Bankable, EUR/W	1,49	1,53	1,40	1,19	1,08	0,81	0,66	0,49	0,42	0,52	0,58	0,57	0,57
Max Price Bankable, EUR/W	1,64	1,74	1,63	1,38	1,28	1,08	0,79	0,69	0,63	0,65	0,60	0,60	0,60

Figure 1.2: Solar module retail price index [5].

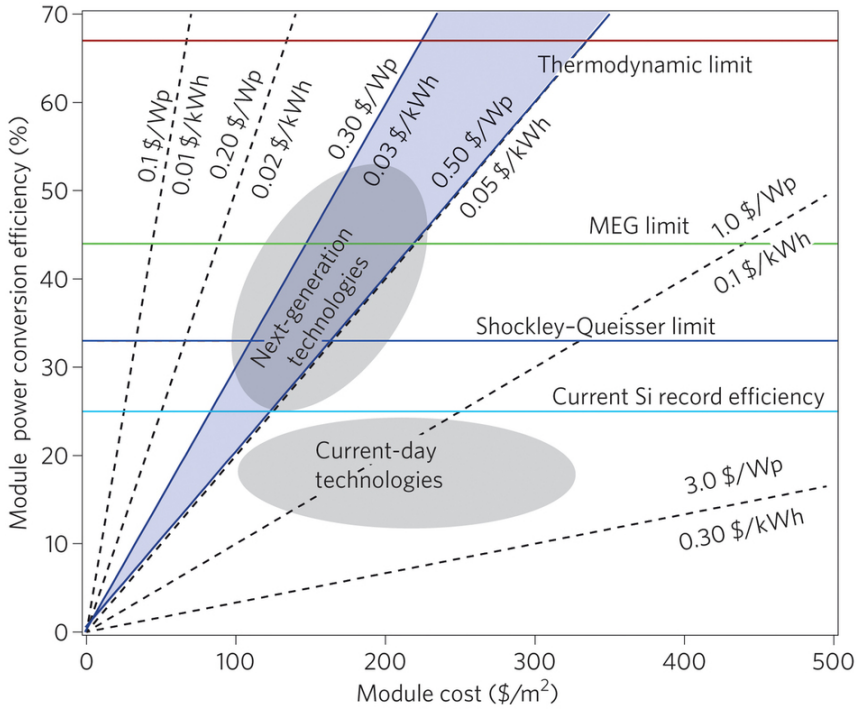


Figure 1.3: Efficiency and cost projections for first, second and third generation photovoltaic technology [6].

1.5 Solar Cell Basics

Solar cells are based upon the effect of sunlight absorption in semiconductors, such as silicon, with band gaps within the solar spectrum energy. Absorbed photons in the semiconductor produce electron-hole pairs with the absorption determined by the band-gap, i.e. the energy separation of the conduction band from the valence band, as illustrated in Figure 1.4 below.

These photo-generated electron-hole pairs must be separated before recombination occurs if they are to contribute to an output current. This can be achieved by arranging the semiconductor in the form of a p-n junction. The inherent electric field in the depletion region of p-n junction is sufficient

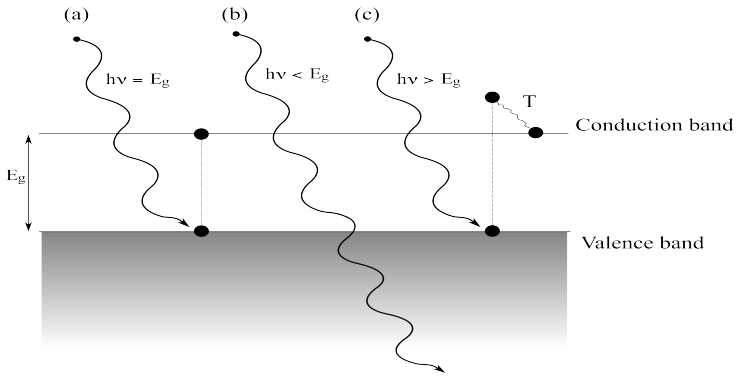


Figure 1.4: Electron promotion by light absorption in semiconductors.

to separate the electron-hole pairs if these are generated approximately one diffusion length from the junction. Figure 1.5 below shows a p-n junction under illumination along with possible carrier recombination losses.

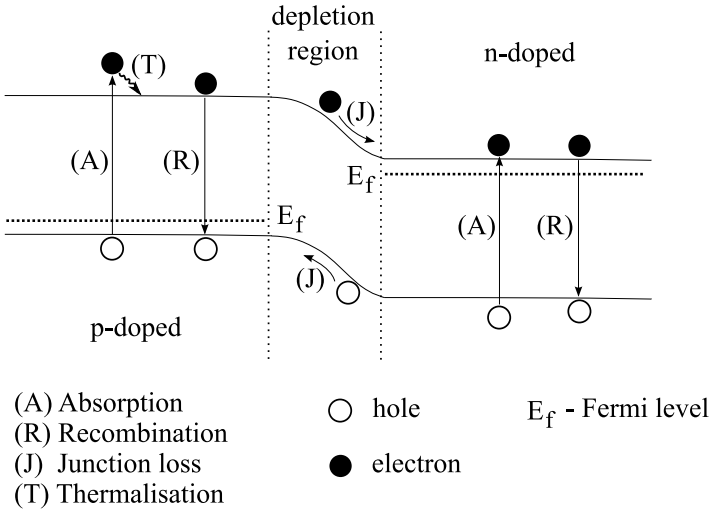


Figure 1.5: Absorption and recombination mechanisms in p-n junctions.

1.5.1 Dark Current

By incorporating a p-n junction in the semiconductor, the inherent features of the junction play a significant part in determining the solar cell behavior. If the p-n junction is in a forward bias a forward diode current is generated. This current, termed dark current, in an ideal diode is defined by the Shockley ideal diode equation

$$J_{dark}(V) = J_0(e^{\frac{qV}{kT}} - 1) \tag{1.1}$$

where J_0 is the ideal reverse saturation current, V is the applied bias, k is the Boltzmann constant, q is the electron charge and T the temperature [7]. In real diodes however radiative and non-radiative recombination occurs as depicted in Figure 1.5. Recombination that occurs in the depletion region via a trap state is described in the Shockley-Read-Hall (SRH) model. Therefore the dark current is described as

$$J_{dark}(V) = J_0(e^{\frac{qV}{nkT}} - 1) \tag{1.2}$$

where n is the ideality factor. In real devices under low bias the ideality factor dominating is n≈2 and under high bias the ideality factor approaches n=1. These contributions to the dark current are further discussed in Chapter 4.

1.5.2 Photocurrent

The electron-hole pairs generated when photons with energy equal or higher than the semiconductor bandgap are absorbed, can be separated to establish a photocurrent. In direct bandgap materials electrons are promoted directly from the valence band to the conduction band. For indirect bandgap materials, the electrons promoted require also a change in momentum as the valence band maximum and the conduction band minimum lie at different wavevector values. The change in momentum is usually provided by lat-

tice vibrations, called phonons, but phonons are required to have the correct momentum. This means that indirect bandgap materials are less efficient absorbers compared to direct bandgap materials.
The short circuit current density produced by the semiconductor depends on the incident spectrum and is calculated as follows:

$$J_{sc} = \int QE(\lambda)F(\lambda)d\lambda \tag{1.3}$$

where QE(λ) is the quantum efficiency of the semiconductor and F(λ) is the incident spectrum.
Therefore to calculate the total output current of the device, the generated photocurrent is subtracted from the existing dark current as it flows in the opposite direction giving:

$$J_{tot}(V) = J_0(e^{\frac{qV}{nkT}} - 1) - J_{sc} \tag{1.4}$$

The assumption that the total current is given as the sum of the photocurrent and the dark current is known as additivity.

1.5.3 Power and Efficiency

The power output of a solar cell depends both on incident illumination as well as the applied bias. Under fixed illumination conditions and varying applied bias the I-V characteristic curve of a device can be obtained. A typical I-V curve is shown below in Figure 1.6.
The efficiency of a solar cell is defined as

$$\eta = \frac{V_{mpp}J_{mpp}}{P_{in}} \tag{1.5}$$

where V_{mpp} and J_{mpp} are the voltage and current density at the maximum power point and P_{in} is the incident power on the device.
The maximum power point of the solar cell is compared to the ideal power

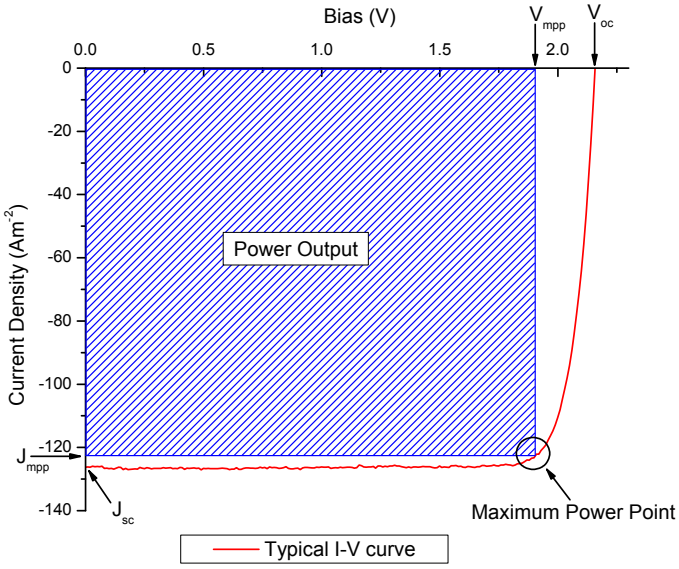


Figure 1.6: Typical light I-V curve.

output of the cell, at the short circuit current and the open circuit voltage, through the fill factor (FF) as described in equation 1.6 below.

$$FF = \frac{V_{mpp}J_{mpp}}{V_{oc}J_{sc}} \tag{1.6}$$

The Fill Factor is important as it directly indicates the presence of any parasitic resistances and any departure from additivity.

The open circuit voltage is the maximum voltage reached across the diode and occurs when the photocurrent equals the dark current. Therefore from equation 1.4 the V_{oc} is related logarithmically to the short circuit current and the dark current as shown below:

$$V_{oc} = \frac{kT}{q} ln \frac{J_{sc}}{J_0} \tag{1.7}$$

Therefore for a linear increase of the J_{sc} with concentration there is an efficiency increase since the V_{oc} also increases logarithmically with light intensity.
The efficiency in terms of V_{oc} and J_{sc} can also be expressed as

$$\eta = \frac{V_{oc} J_{sc} FF}{P_{in}} \tag{1.8}$$

1.5.4 Parasitic Resistance Effects

A solar cell will seldom operate as an ideal device. It can contain inherent parasitic resistance or these might be present due to non-ideal device processing. Parasitic resistance effects materialise in the form of series and shunt resistance as depicted in Figure 1.7 below.

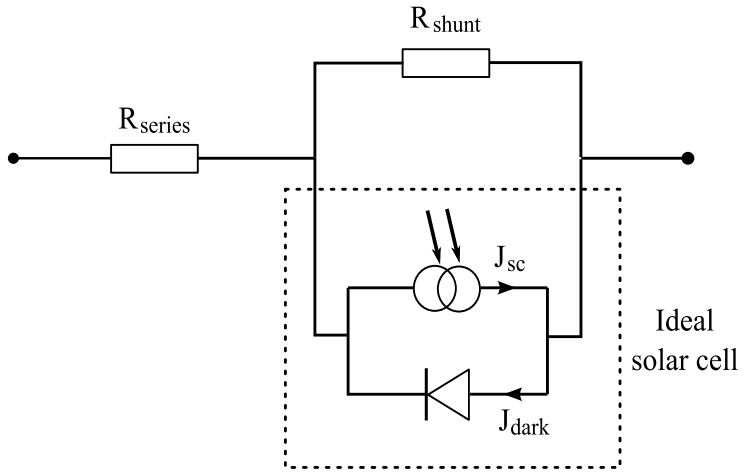
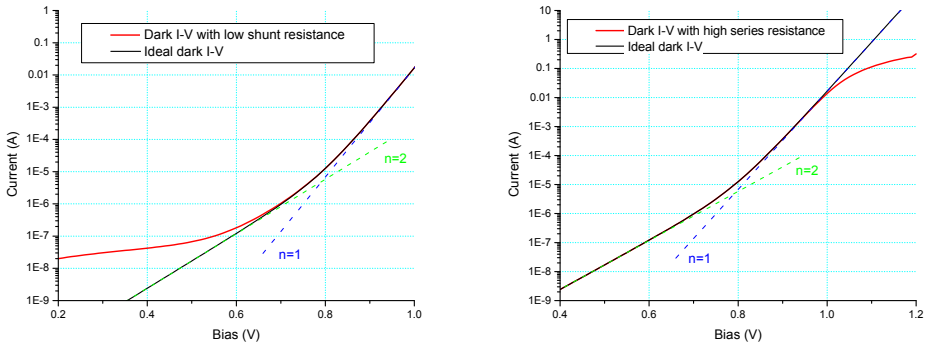


Figure 1.7: Solar cell equivalent circuit with parasitic resistances.

Series resistance builds up from the solar cell wiring, resistance in the top and bottom cell metallization contacts and sheet resistance in the conducting layer inside the front surface of the solar cell between the contacts. Current

leakage at the edges of the solar cell device appears in the form of low shunt resistance.

The parasitic resistance effects can be seen in both the dark current measurements and the characteristic light I-V curve of the solar cell. In the dark current measurement these effects appear as high current tails in the low voltage bias regime for the case of low shunt resistance and low current tails at high bias voltage for the case of high series resistance. Both effects can be seen below in Figure 1.8.

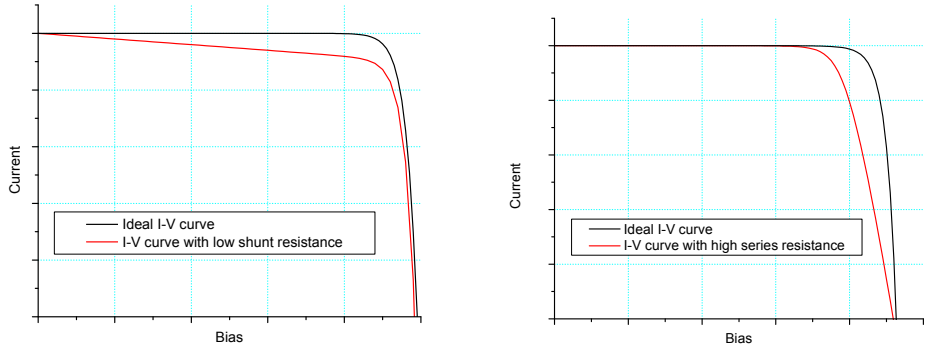


(a) Low shunt resistance

(b) High series resistance

Figure 1.8: Parasitic resistance effects on dark current.

A low shunt resistance will cause a gradual decrease in the photocurrent from the short-circuit current to the maximum power point current as a bias voltage is increased. High series resistance appears as a gradual photocurrent drop from the maximum power point current to the open circuit voltage point instead of a sharp transition in the ideal case. Both effects are depicted in Figure 1.9 below.



(a) Low shunt resistance

(b) High series resistance

Figure 1.9: Parasitic resistance effects on light IV characteristic curve.

1.5.5 Bandgap Effect on Efficiency

Setting all losses aside, the size of the semiconductor bandgap plays the most prominent role in determining the overall efficiency of a solar cell for a given spectrum. Photons can only be absorbed if they possess energy equal or greater than the bandgap. Having a narrow bandgap translates into more photons being absorbed and thus a higher photocurrent. On the other hand a narrow bandgap also means a smaller V_{oc} and the dark current, which limits the V_{oc}, will be large due to the rise in reverse saturation current, J_0, since

$$J_0 \propto exp - \frac{E_g}{kT} \tag{1.9}$$

As the overall efficiency depends on the product of the J_{sc} and the V_{oc}, the optimum bandgap must satisfy this condition 1.9. This optimum value is dependent on the chosen spectrum and in the case of the AM1.5 global spectrum (see Section 1.5.6) the optimum value for the bandgap was calculated to be 1.37eV [9]. A suitable material that exhibits a bandgap value close to the theoretical optimum is InP with a 1.34eV bandgap. However GaAs with

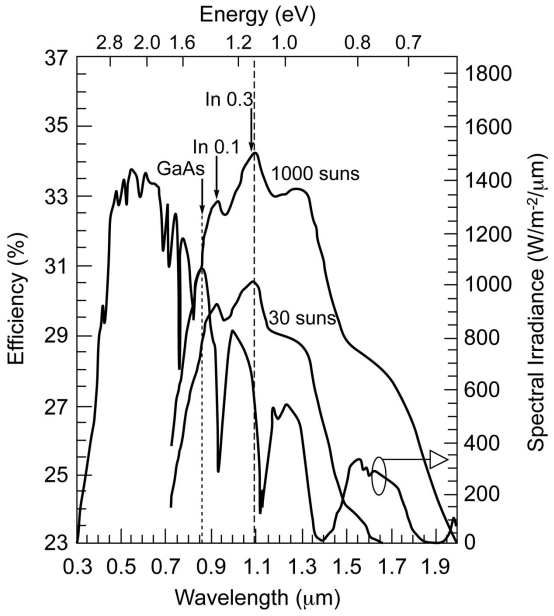


Figure 1.10: Efficiency limit as a function of bandgap at 30x and 1000x concentration levels [8].

a bandgap at approximately 1.43eV is more widely used due to its robustness and lower cost. Silicon, which is the most widely used material for solar cells exhibits a bandgap around 1.2eV.

The theoretical limit on efficiency of a single junction solar cell with optimum bandgap for AM1.5 spectrum is around 33%. This theoretical limit reaches 37% under 1000x concentration [9]. Currently the world efficiency record under AM1.5g spectrum is 28.8% under one sun concentration and 29.1% under 117x concentration [10].

1.5.6 Solar Spectra

The extra terrestrial spectrum does not show significant yearly variation. However the terrestrial solar spectrum varies throughout the day and depends

mainly on the atmospheric depth that the extra terrestrial spectrum passes through. The atmospheric depth is typically referred to as Air Mass (AM). The Air Mass is defined as the cosec of the zenith angle (Z) and can be calculated by Equation 1.10 below. The Air Mass can also be calculated by the latitude, longitude, date and time.

$$Airmass = \frac{1}{cos(Z) + 0.50572 - (96.07995 - Z)^{-1.6364}} \tag{1.10}$$

Figure 1.11 below depicts measured solar spectra over the course of a day. Shorter wavelengths suffer more scattering than longer wavelengths thus spectra early in the morning and late in the afternoon have a stronger long wavelength component i.e. become 'red-rich'.

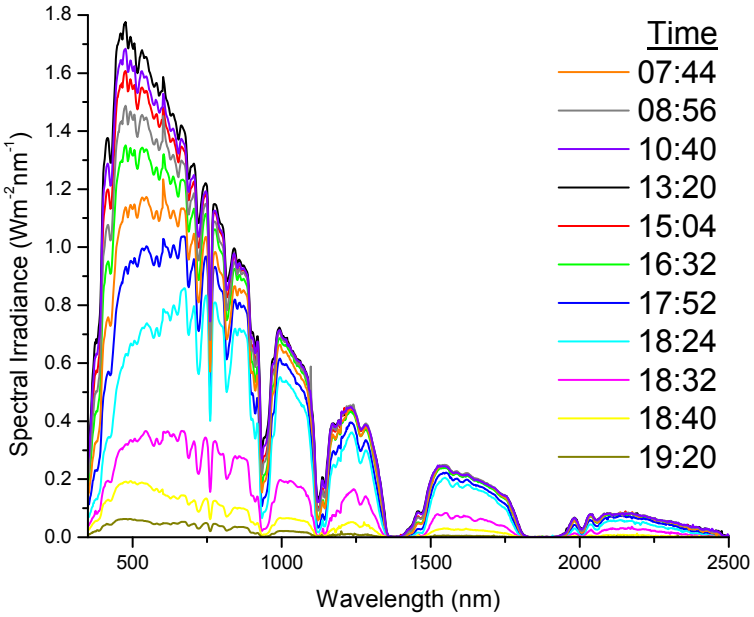


Figure 1.11: Solar spectrum variation over the course of a day.

A standard spectrum was therefore required to provide a benchmark for solar cell inter-comparison. A set of standard spectra was developed by the American Society for Testing and Materials (ASTM) based on daily spectra of mid-latitude America. Figure 1.12 shows the AM0 (extra terrestrial spectrum), AM1.5 global and AM1.5 direct spectra as defined in the ASTM G-173 standard [11].

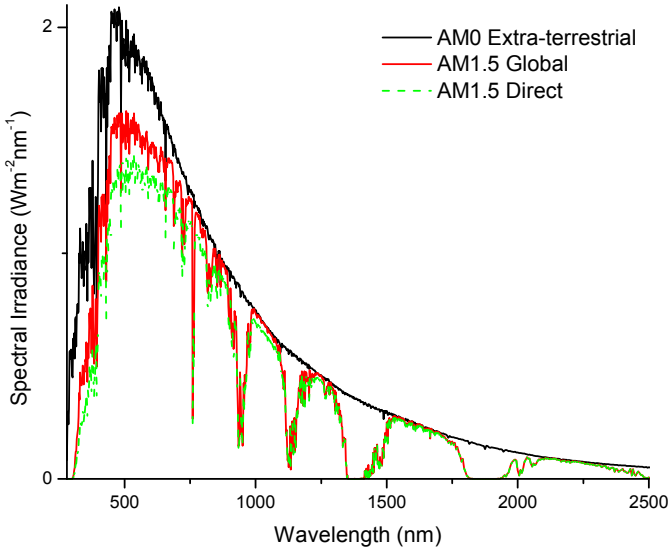


Figure 1.12: Standard solar spectra as defined in ASTM G-173 standard.

Global spectra are defined as the total incident spectrum on a flat surface originating from a hemispherical direction thus including diffuse radiation and albedo effects. Direct spectra are defined as the spectral component originating from the solar and circumsolar disks. These are important for GaAs cells as the direct can be concentrated by a lens or mirror to reduce costs. New standards are also being developed that will take into account a low aerosol optical depth (low - AOD). Aerosols are air-suspended solid and liquid particles such as dust, salt and smoke that prevent light transmission by reflection, scattering or absorption.

1.6 Practical Photovoltaics

Practical solar cell structures contain additional features that serve the purpose of reducing losses that are inherent in real devices.

1.6.1 Window layers

The front surface, due to the high number of trap states present in the band gap, is a significant source of recombination losses for minority carriers. A practical way of reducing the front surface recombination is with the addition of a high band gap material on the front surface. The high band gap material reflects the minority carriers back to the field-bearing region of the cell whilst allowing all the light through. These high band gap layers are typically referred to as window layers. For GaAs devices typical window layers used are lattice matched AlGaAs or InGaP windows. In the case of InGaP cells typical window structures are made of lattice matched AlInP.

1.6.2 Cap layers and Metal Contacts

Most window layers are susceptible to oxidisation. In order to prevent this a GaAs cap layer is grown on top of window layer. This cap layer has a dual purpose as it can be heavily doped in order to provide a low resistance contact with the front metal contact. The front metal contact is required to be an ohmic contact and in addition it must cover the minimum device area possible in order to allow the light to reach the device. Typical ohmic contacts used for GaAs p junctions are Ti/Pt/Au layered contacts. The front contact is defined as a grid using a photolithographic process with front surface cover ratios ranging from 1% to 9% excluding the busbar. The rear surface contacts are less complicated as they can cover the whole device area. For n type GaAs substrates, Ge/Au/Ni/Au layered contacts provide good ohmic rear contacts.

1.6.3 Back Surface Fields

Minority carriers will be lost in a similar fashion at the rear of the n-type region. The substrate, typically around 300μm, is far longer than the diffusion length of the minority carriers. Thus any minority carriers entering the substrate will unquestionably be lost by recombination. This can be avoided by inserting a heavily doped region n-type region, which will create a small electric field in the base region. This field will reflect the minority carriers, in this case holes, back to the depleted region. Another way of achieving this is by inserting a layer of larger band gap semiconductor similar to the window layer.

1.6.4 Anti-Reflection Coatings

The high difference between the refractive indices of GaAs and air would mean a substantial reflective loss. In order to minimise reflections and enhance absorption anti-reflection coatings (AR) are applied on the front surface of the solar cell. The cap layer absorbs a significant portion of the incident radiation which cannot be utilised due to the presence of the window. It is therefore removed prior to the deposition of the AR coat which now serves a dual purpose of protecting the window layer and minimising reflections. Typical AR coats can consist of either a single layer of SiN_x or a dual layer of SiN_x and SiO_2 deposited using a plasma enhanced chemical vapour deposition process (PECVD). The optimum thickness of the dielectric layers is determined using the Fresnel relations.

1.7 Quantum Well Solar Cells

Quantum wells consist of thin layers of low band gap material sandwiched between thick layers of bulk cell material. The thickness of the quantum well layer is comparable to the electron wavelength in the material and the

depth is defined by the band gap of the well material minus the 'zero point energy'. The solar cell absorption can be extended with the use of quantum wells as the effective band gap of the material is lowered with the added advantage that the dark current of the device lies between the characteristic dark current of the bulk and well materials. In addition the open-circuit voltage observed in these devices is higher than expected for bulk material of that band-gap [12].This enables band gap engineering of the solar cell to a great extend as the structures can be grown by Metal Organic Vapour Phase Epitaxy (MOVPE) or Molecular Beam Epitaxy (MBE) which have angstrom precision growth over the well structures. In the case of GaAs, past work includes AlGaAs, InGaP and InGaAs quantum well structures. An updated review of the recent advancements in Quantum Well solar cells can be found at Ref. [13].

1.7.1 Multi-Quantum Well Structures

Quantum wells can be grouped together in multi-quantum well (MQW) structures with higher band gap material between the wells acting as barriers. MQW structures create strong excitons even at room temperatures unlike bulk material where excitons are only demonstrated at low temperatures.If the quantum well structure is inserted in an undoped intrinsic region the excitations are particularly strong. The intrinsic region is typically 1-1.5μm wide, which is sufficient to host the MQW structure and maintain throughout the electric field between the p and n regions if the background doping is small enough. In order to achieve higher cell efficiencies the excess photocurrent generated must over-compensate the drop in open-circuit voltage due to the lower-band gap material.

1.7.2 Strain Balanced MQW Solar Cells

The drawback of incorporating MQW structures in GaAs solar cells is the absence of lattice matched binary or ternary alloys with a lower band gap. Figure 1.13 below depicts a graph of the lattice constants of various binary and tertiary III-V compounds along with their corresponding band gap energies.

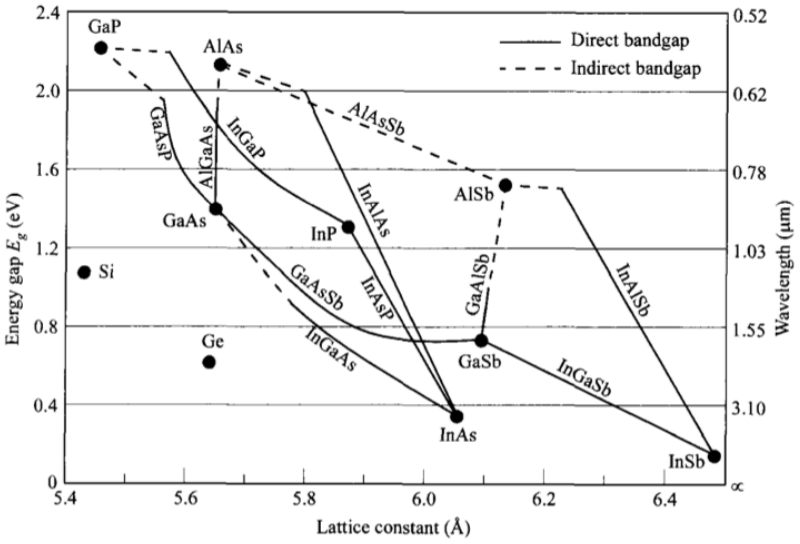


Figure 1.13: Energy gap vs lattice constant for some common elementary and binary semiconductors [14].

Incorporating lattice mismatched quantum wells will result in creation of misfit dislocations which will increase the non-radiative recombination component (n≈2) of the dark current. Strain balancing is the method developed to compensate this effect by incorporating well barriers with the opposite strain to the well to balance the stresses at the interfaces [15]. Incorporating InGaAs quantum wells in GaAs will result in a compressive strain in the material. By containing each well in appropriate GaAsP barriers, which induce a tensile strain of the same magnitude, will result in a barrier-well-barrier

structure of zero effective strain. As long as the layers do not exceed a critical thickness, where the material will relax during growth, the strain balancing technique can produce 'zero stress' structures with high well numbers. Solar cells with up to 80 wells of 1.24eV band gap have been demonstrated with the stress-balancing technique [16].

1.8 Multi-junction Solar Cells

In order to achieve higher efficiencies than the theoretical single bandgap efficiency other means have to be employed. Absorbed photons with higher energy than the bandgap excite electrons above the conduction band, which in turn lose the excess energy through thermalisation to drop to the conduction band edge. For efficient absorption without thermalisation losses, the bandgap must correspond to the absorbed photon energy. One way to minimise this loss is by stacking cells of decreasing bandgap material in a multi-junction configuration. Subcells are transparent to photons with energy below their bandgap. A photon is therefore absorbed in the first sub-cell with lower energy bandgap. Hence the thermalisation energy loss is minimised. In a dual junction solar cell the spectrum is therefore split between the cells as shown in Figure 1.14. As the number of sub-cells increases the thermalisation losses are minimised. The theoretical limiting efficiency of an infinite multi-junction cell is estimated to 86.8% using a detailed balance approach [17].

1.8.1 Dual Junction Solar Cells

Figure 1.15 portrays the maximum theoretical efficiency of dual junction solar cells for different combinations of top and bottom cell band gaps. The highest possible dual junction efficiency of 42% can be achieved using 1.6 - 1.8eV top cells and 0.9 - 1.2eV bottom cells. In practice however, lattice matched devices grown on GaAs substrates prohibit the above combinations.

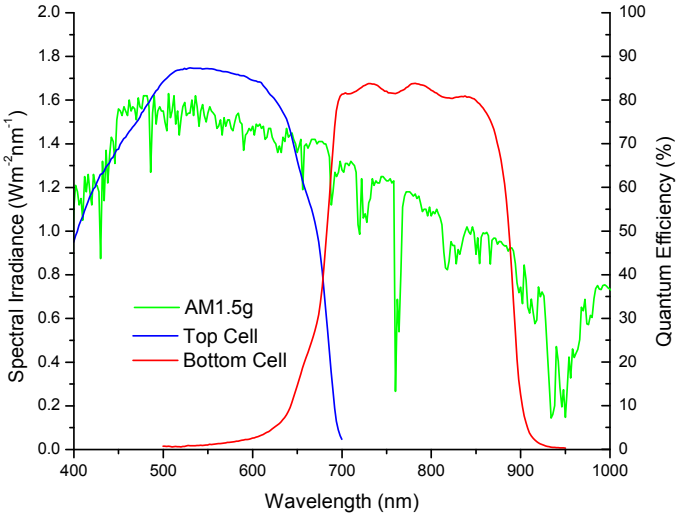


Figure 1.14: Absorption of AM1.5g spectrum by a dual junction cell

Current world record efficiency for dual-junction cells is 34.1% achieved with an InGaP/GaAs device and the highest recorded efficiency is 46% [18] by a four-junction wafer-bonded solar cell [19].

1.8.2 Multi-junction Structure Types

The constituent junctions of a multi-junction solar cell can be arranged in a series or parallel configuration. Arranging the junctions in a parallel configuration provides addition of the photocurrents while maintaining the bias voltage across all junctions the same. The optimum bias voltage is therefore limited by the narrowest band gap junction. Therefore the high open circuit voltage of the wider band gap junctions is not utilised and in addition increasing the concentration does not offer significant eficiency increase. Another detrimental effect inherent in parallel configurations is that the devices are high current and low voltage which translates into higher resistive losses. Therefore the most common configuration for multi-junction solar cells is

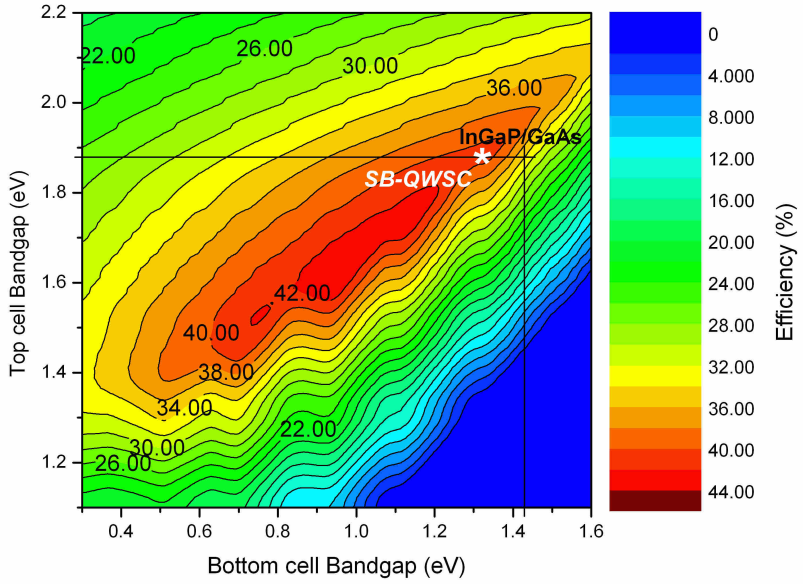


Figure 1.15: Optimum band gap combinations contour plot for dual junction cells under AM1.5 spectrum. Intersecting black lines depict lattice matched InGaP/GaAs tandem. The predicted efficiency of a Strain Balanced Quantum Well Solar Cell (SB-QWSC) is also depicted.

with the junctions in series; either in a mechanical or monolithic stack. Mechanical stacks offer the advantage of choosing freely the material for each junction and thus no constraints are imposed on the choice of band gap for each junction. However mechanical stacks are difficult to manufacture and optical losses dominate in the interfaces between junctions due to poor light coupling.

Monolithic structures can be easily grown in a single growth process. The material choice is limited though by the lattice matching constrains. Only specific composition combinations give lattice matched, hence dislocation

free, monolithic structures. Therefore the band gap combination choices are limited, prohibiting efficiencies that near the theoretical limits. Lattice mismatched, more commonly known as metamorphic, devices have reported efficiencies of 44.4% [20]. However this type of devices are not dislocation free and under normal operating conditions the efficiency of the devices might decrease with increased usage. The latest generation of multi-junction devices currently holding the record efficiency of 46% utilises a technique named wafer bonding which essentially enables the electro-mechanical bonding of lattice mismatched materials with electrically conductive, transparent bonds [21].

1.8.3 Tunnel Junctions

Monolithic devices require the addition of tunnel junctions for inter-junction connections. The tunnel junction effect was first described by L. Esaki in 1958 [22]. The junction consists of a heavily doped p-n junction which allows an Ohmic contact between the p-junction of one cell to the n-junction of the other. The energy band diagram of an ideal dual junction solar cell was studied by Lamorte et al [23] and is depicted in Figure 1.16 below.
The tunnel junction positioned between the two cells allows excited electrons in the conduction band of the top cell to tunnel through to the valence band of the bottom cell. There absorption of a lower energy photon can excite the electron to the conduction band of the bottom cell.
The current-voltage characteristic curve of the tunnel diode is depicted in Figure 1.17. For small forward bias the tunnelling current increases linearly to a maximum thus we can assume a low resistance and minimum voltage drop between the junctions. If however the voltage increases beyond V_p then the tunnelling current diminishes drastically. This effect of tunnel junctions limiting the solar cell is often exhibited at high concentrations where currents in excess of $14A/cm^2$ are expected [24].

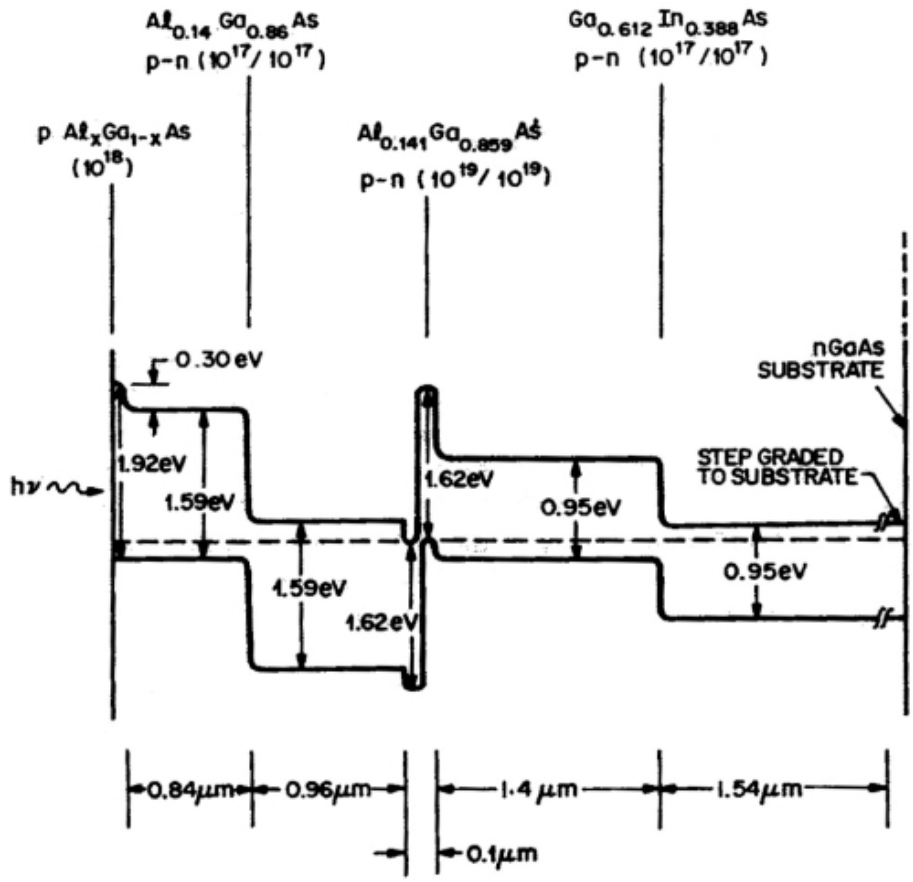
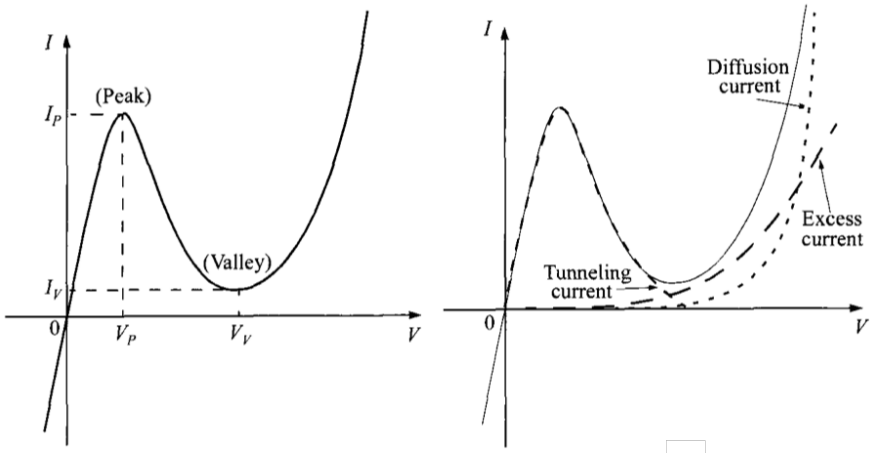


Figure 1.16: An idealised cascade two junction solar cell band diagram [23].

1.8.4 MQW multi-junction cells

As mentioned in section 1.8.1 the record efficiency for a dual junction cell was achieved by a InGaP/GaAs solar cell. This cell was however current limited, as with most dual junction devices, by the GaAs bottom cell. If the band gap of the GaAs bottom cell is decreased, in order to generate more photocurrent, the band gap of the top cell is also lowered to maintain the lattice matching condition. This does not yield an efficiency increase because as seen in Figure 1.15 decreasing both cell band gaps would result in moving



(a) (b)

Figure 1.17: (a) Static current-voltage characteristics of a typical tunnel diode. I_p and V_p are the peak current and peak voltage. I_v and V_v are the valley current and valley voltage. (b) The total static characteristics are broken down into three components [14].

parallel to the graph's contour lines.

Insertion of MQW structures in the bottom GaAs cell would however decrease the effective band gap of the GaAs cell without affecting the top cell band gap. This would result in substantial efficiency increase according to Figure 1.15. A Strain Balanced MQW GaAs solar cell (SB-QWSC) is proven to yield higher photocurrents than bulk GaAs solar cells [25]. Therefore SB-QWSC are ideal candidates for bottom cells in dual junction solar cells. The flexibility in band gap engineering of the SB-QWSC enables the multi-junction cell designer to achieve current matching between top and bottom cell thus achieving maximum device efficiency.

1.9 Objectives of Thesis

The main objectives of this thesis were:

i. Experimental Characterisation of the World's first dual junction cell with quantum wells in the bottom cell.

ii. Modelling of the results of the characterisation and assessment of performance with a simulation program.

iii. Optimisation of dual-junction quantum well cells and extrapolation using a simulation program to investigate performance at high concentrations.

iv. Design and modelling of a concentrator optics setup for use with dual junction solar cells.

Bibliography

[1] European Photovoltaic Industry Association, "EPIA Global Market Outlook 2014-2018." http://www.epia.org/news/publications/, 2014.

[2] European Commission, "Energy for the future: Renewable sources of energy, white paper for a community strategy and action plan," November 1997.

[3] Renewable Energy World.com, "China Passes Renewable Energy Law." http://www.renewableenergyworld.com/rea/news/article/2005/03/china-passes-renewable-energy-law-23531, March 2005.

[4] CleanTech Group LLC, "Clean technology venture investment reaches record $8.4 billion in 2008 despite credit crisis and broadening recession." http://cleantech.com/about/pressreleases/010609.cfm, March 2009.

[5] Solarbuzz.com, "Solar Module Price Highlights - January 2006." http://www.solarbuzz.com/Moduleprices.htm, Januray 2006.

[6] M. C. Beard, J. M. Luther, and A. J. Nozik, "The promise and challenge of nanostructured solar cells," *Nat Nano*, vol. 9, no. 12, pp. 951–954, 2014.

[7] J. Nelson, *The Physics of Solar Cells*. London: Imperial College Press, 2003.

[8] J. S. Ward, M. W. Wanlass, K. A. Emery, and T. J. Coutts, "GaInAsP Solar Cells with the Ideal Band Gap for Terrestrial Concentrator Applications," in *Photovoltaic Specialists Conference, 1993, 23rd IEEE*, pp. 650–654, May 1993.

[9] C. Henry, "Limiting efficiencies of ideal single and multiple energy gap terrestrial solar cells," *Journal of Applied Physics*, vol. 51, no. 8, 1990.

[10] M. A. Green, K. Emery, Y. Hishikawa, W. Warta, and E. D. Dunlop, "Solar Cell Efficiency Tables (Version 44)," *PROGRESS IN PHOTOVOLTAICS: RESEARCH AND APPLICATIONS*, vol. 22, pp. 701–710, July 2014.

[11] A. S. G173-03, "Standard Tables for Reference Solar Spectral Irradiances: Direct Normal and Hemispherical on 37° Tilted Surface," tech. rep., ASTM International, West Conshohocken, PA, 2012.

[12] K. W. J. Barnham, J. P. Connolly, P. Griffin, G. Haarpaintner, J. Nelson, E. Tsui, A. Zachariou, and J. Osborne, "Voltage enhancement in quantum well solar cells," *Journal of Applied Physics*, vol. 80, pp. 1201–1206, July 1996.

[13] L. Tsakalakos, ed., *Nanotechnology for Photovoltaics*. CRC Press, March 2010.

[14] S. Sze and K. K. Ng, *Physics of Semiconductor Devices*. John Wiley and Sons, 3 ed., April 2006.

[15] K. W. J. Barnham, I. M. Ballard, J. Barnes, J. P. Connolly, P. Griffin, B. Kluftinger, J. Nelson, E. Tsui, and A. Zachariou, "Quantum Well Solar Cells," *Applied Surface Science*, vol. 113-114, pp. 722–733, 1997.

[16] M. C. Lynch, *Modelling and Optimisation of Single Junction Strain Balanced Quantum Well Solar Cells*. PhD thesis, Imperial College of Science, January 2008.

[17] A. Marti and G. L. Araujo, "Limiting efficiencies for photovoltaic energy conversion in multigap systems," *Solar Energy Materials & Solar Cells*, vol. 43, pp. 203–222, 1996.

[18] M. A. Green, K. Emery, Y. Hishikawa, W. Warta, and E. D. Dunlop, "Solar Cell Efficiency Tables (Version 45)," *PROGRESS IN PHOTOVOLTAICS: RESEARCH AND APPLICATIONS*, vol. 23, pp. 1–9, January 2015.

[19] Fraunhofer ISE, "New world record for solar cell efficiency at 46% French-German cooperation confirms competitive advantage of European Photovoltaic inductry." http://www.ise.fraunhofer.de/en/press-and-media/press-releases/press-releases-2014/new-world-record-for-solar-cell-efficiency-at-46-percent, December 2014.

[20] Sharp Corporation, "Sharp Develops Concentrator Solar Cell with World's Highest Conversion Efficiency at 43.5%." http://sharp-world.com/corporate/news/120531.html, May 2012.

[21] T. N. D. Tibbits, P. Beutel, M. Grave, C. Karcher, E. Oliva, G. Siefer, A. Wekkeli, M. Schachtner, F. Dimroth, A. W. Bett, R. Krause, M. Piccin, N. Blanc, M. Munoz-Rico, C. Arena, E. Guiot, C. Charles-Alfred, C. Drazek, F. Janin, L. Farrugia, B. Hoarau, J. Wasselin, A. Tauzin, T. Signamarcheix, T. Hannappel, K. Schwarzburg, and A. Dobrich, "New Efficiency Frontiers with Wafer-Bonded Multi-Junction Solar Cells," in *29th EUPVSEC*, pp. 1975–1978, 2014.

[22] L. Esaki, "New phenomenon in narrow germanium p-n junctions," *Physics Review*, vol. 109, January 1958.

[23] M. F. Lamorte and D. Abbott, "Analysis of AlGaAs-GaInAs Cascade Solar Cell under AM0-AM5 Spectra," *Solid State Electronics*, vol. 22, pp. 467–473, May 1979.

[24] W. Guter and A. W. Bett, "I-V Characterization of Tunnel Diodes and Multijunction Solar Cells," *IEEE Transactions on electron devices*, vol. 53, pp. 2216–2222, September 2006.

[25] K. W. J. Barnham, I. M. Ballard, B. C. Browne, D. B. Bushnell, J. P. Connolly, N. J. Ekins-Daukes, M. Fuhrer, R. Ginige, G. Hill, A. Ioannides, D. C. Johnson, M. C. Lynch, M. Mazzer, J. S. Roberts, C. Rohr, and T. N. D. Tibbits, "Recent Progress in Quantum Well Solar Cells," in *Nanotechnology for Photovoltaics* (L. Tsakalakos, ed.), ch. 5, pp. 187–210, CRC Press, 2010.

Chapter 2

Solar Cell Device Processing

The solar cell structures grown on semiconductor substrates require additional work in order to obtain functional devices. This work is referred to as device processing and is a set of steps involving dry and wet chemistry. The processing recipe described below was used by the author at the Center for Integrated Photonics (CIP) to manufacture concentrator solar cell devices as well as photodiodes and fully metallised devices that are more suitable for characterisation. A schematic diagram of the processing recipe is depicted in Figure 2.3.

2.1 Wafer cleaning and front metal deposition

Prior to the front surface metal deposition the wafer requires to be cleaned and de-oxidized. The GaAs cap layer forms an oxide layer as it slowly reacts with air. To remove this oxide the wafer is dipped for 60 seconds in an HCl(36%):H_2O (1:1) solution which removes any oxides but does not affect the GaAs cap. Once the wafer is rinsed and dried the front metal can then be deposited.

The front surface metallization is formed in two steps: the ohmic contact is formed using a load-locked RF sputtering system and the desired thickness of the gold contacts is then achieved using chemical electrodeposition.
The RF sputter deposition utilises an argon ion beam to release ions of material from the sputter target, i.e the material source. The released ions are subsequently accelerated in a DC field towards the susceptor, i.e the wafer. This method yields high adhesion contacts as some penetration in the susceptor is achieved during the deposition process. Any crystallographic damage incurred during the deposition can be reversed through an annealing stage. Typical contacts deposited on the highly doped GaAs cap are 50nm of Titanium followed by 100nm of Platinum and 100nm of Gold. This creates an ohmic type contact with a low contact sheet resistance where the dominant carrier transport is field emission quantum tunnelling [1, 2].

2.2 Front Contact Photolithography

The front contact surface is defined using a photolithographic process. The masks for the photolithographic process were designed by Tom Tibbits and are based upon the solar cell grid developed at Polytechnic University of Madrid (UPM) [3, 4]. The masks were designed for use with a 'negative' photoresist, which becomes soluble in the developer once exposed. Prior to coating, the wafer is dried on a 200°C hot-plate for 30 minutes to remove any residual humidity. The wafer is then placed on a spin coater where an adhesion promoter coat of HexaMethyldiSilazane (HMDS) is applied for 30 seconds at 4000rpm. The photoresist, Shipley Microposit S1828, is then applied for 30 seconds at 400rpm. With this specific resist a 3μm coat is obtained with these settings. The wafer then undergoes a 'soft bake' where it is heated at 90°C for 10 minutes to remove the organic solvent present in the photoresist. Using a Karl-Zeiss aligner the front grid is exposed on the wafer according to local instructions. The exposure time depends on

the intensity of the UV source in the aligner. Typical exposure values for a 3μm S1828 resist layer are 40-50 seconds. The exposed resist is removed by dipping the wafer in MF319 developer for 60 seconds. The unexposed resist is also 'hardened' during this step to prevent further exposure. Any residual organic traces are removed during a 3 minute 'ashing' step in an oxygen plasma.

2.2.1 Photoresist Profile

The ideal photoresist profile defines a metallisation profile which does not cast any shadow on the cell. The ideal shape therefore should produce rectangular contacts upon metal deposition. In reality however the photoresist creates an inverted conical profile [5]. In the case of photoresist S1828, used by the author in the device processing, the profile created widens significantly for photoresist thicknesses exceeding 3μm. Deposition depth was kept below 3μm to prevent the metal contacts from spreading at the top and shading the active cell area. Another method used to avoid this was subjecting the photoresist to an additional baking step prior to developing the photoresist. This resulted in a small amount of water being removed from the upper layer of the photoresist thus slowing the developing process and producing a profile similar to the one shown in Figure 2.1(c).

2.3 Gold Electrodeposition

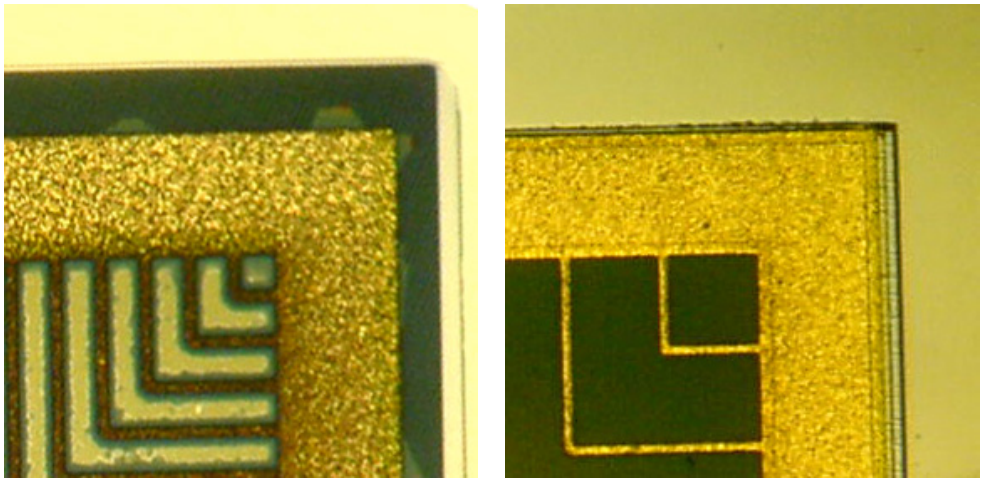
The front metallization thickness of 3μm necessary for high current conductivity cannot be achieved by the sputtering process used for good metal adhesion through the narrow fingers of a solar cell grid. The alternatives are either by evaporation deposition or electrodeposition. The latter was chosen as the gold waste in the case of evaporation deposition is too great when only small test samples are coated and this technique is scalable and cost effective [6]. The electrolyte solution of gold thiosulphate was kept at a



(a) Ideal Profile (b) Actual Profile (c) Profile with pre-developing bake

Figure 2.1: Photoresist profiles.

constant temperature of 50°C. The sample was placed on the cathode where the positive gold ions precipitate. To ensure a uniform deposit the anode is formed by a cylindrical Ti metal mesh plated with Pt around the beaker. The deposition rate depends on the current density supplied which is controlled by the external voltage source. A small current density translates into fine gold deposition at a very slow rate whereas a larger current density means faster deposition with larger grains and a sandy appearance (see Figure 2.2). Different sample sizes mean re-adjusting of the current in order to maintain the correct current density needed for deposition. To avoid this current re-adjustment for each sample a glass plate with a large metallisation area on the periphery was used on the cathode with both the sample connected with the metallisation. In this way the total metallisation area changes marginally with different sample area sizes which in turn translates into similar current densities for the same current setting on the power supply thus improving repeatability.



(a) Coarse Gold formed by a high deposition rate

(b) Fine Gold formed by a low deposition rate

Figure 2.2: Gold contacts resulting from different deposition rates on samples developed by the author.

2.4 Gold and Platinum Dry Etch

Upon completion of the electro-deposition process the photoresist defining the front contacts needs to be removed in order to expose the unwanted metallization. The resist is removed by rinsing the sample in acetone and subsequently in isopropyl alcohol (IPA). The sample undergoes an additional ashing step to remove any residual organic deposits.

The excess gold and platinum are removed in a reactive ion etching (RIE) machine using an argon and oxygen plasma. The titanium layer is removed using a CF_4, O_2 plasma. To remove any residual titanium which might still be present on the sample in the form of titanium oxide (titania) the sample undergoes another 'cleaning' dry etch in an argon plasma for an additional 60 seconds. This guarantees a clean free surface with no titania blemishes.

Unfortunately any titania blemishes cannot be seen after the titanium etch stage and are only pronounced once the anti-reflection coating is applied. Improved results were obtained following suggestion by Malcom Pate (private communication) using by a 60 second dry etch in an argon plasma. This method produced blemish-free surfaces with higher repeatability.

2.5 GaAs Cap Etch

The next step is to remove the GaAs highly doped cap in order to expose the window layer. This step is crucial as the etch used must not affect the window layer and in addition it should be controlled so that no undercutting of the cap layer occurs underneath the fingers and busbar. Several wet etches were examined including citric acid with hydrogen peroxide. The best results were obtained with a 1:20:333 NH_4OH:H_2O_2:H_2O solution. This gave a clear colour change from grey on a GaAs surface to brownish on a AlInP surface with a dark blue (oxidized GaAs) intermediate stage after a 30 second dip. A variation of this etch using only 1:19 NH_4OH:H_2O_2 gave good results as well with a very fast etch of under 5 seconds [7].

2.6 Anti-Reflection Coat Deposition

The anti-reflection (AR) coating deposition should follow immediately after the GaAs cap etch to avoid any oxidation of the window layer. The anti-reflection coat is deposited using a plasma enhanced chemical vapour deposition (PECVD) method. Deposition of SiN_x and SiO_2 is obtained from precursor gases of SiH_4, NH_3 and N_2O and is enhanced using a plasma.
To minimize the reflection losses that would occur at an air/AlInP interface a dual layer anti-reflection coating of silicon nitride and silicon oxide has been developed [4]. The composition of the anti-reflection coating was optimized for an AlGaAs window but it provided excellent results for the AlInP layer

as well. Typical layer thickness deposited were 60nm of SiN_x followed by 100nm of SiO_2.

2.7 Opening for Electrical Contact

The opening of the anti-reflection coating for the electrical contacts was defined on the sample using another photolithography step as described above using an appropriate mask. In addition the AR coat is removed from the periphery of the devices to enable etching of the excess material (mesa etch) in order to electrically isolate the devices. The sample was then placed in a Reactive Ion Etching (RIE) machine. The SiO_2 was etched using a CHF_3 and O_2 plasma and the SiN_x was etched using a CF_4 plasma. The sample was then rinsed with acetone and IPA to remove the photoresist and ashed to remove any residual organic deposits.

2.8 Device Isolation (Mesa Etch)

The devices are isolated from each other and the device active area is defined using a wet mesa etch. Several mesa etches were tried with the following two producing the best results:

2.8.1 Two Step Selective Mesa Etches

The mesa etch was performed using two distinct etchants The first etches selectively the GaInP top layers and the second etches the GaAs bottom layers. To etch selectively the top GaInP layers a solution of 1:1 HCl:H_3PO_4 was used with an etch rate of 0.60μm/minute. The etchant is selective and stops at the first GaAs layer. The GaAs layers were etched using a 1:1:10 H_2SO_4:H_2O_2:H_2O solution [8]. This etch rate depends on the GaAs composition and for the typical cell structure the etch rate was around 0.60μm/minute at 20°C.

2.8.2 Isotropic Non-selective Mesa Etch

The mesa etch was performed using a single step using a non-selective isotropic etch. The etch chosen was an 1:1:1 HBr:CH_3COOH:$K_2Cr_2O_7$. This particular etch had to be mixed in the order specified otherwise it became ineffective if any component was diluted in any way. For the etching to take place the sample was dipped first in a 1:1 HCl:H_2O solution for a few seconds and then placed in the etching solution. A similar approach, which was equally effective, was to prepare the solution as 1:1:1:2:2 HBr:CH_3COOH:$K_2Cr_2O_7$:HCl:H_2O in this order. The etch rate was very fast at 2-5μm/minute depending on the III-V compound[9].

Prior to the mesa etch the profile height was measured using a DekTak profiler. The mesa profile height was re-measured after each mesa etch step and the process was repeated until the desired height was achieved. The DekTak profiler used a 50μN force contact probe to scan the surface with Angstrom ($\mathring{A}$) resolution.

2.9 Back Surface Contact Deposition

Upon completion of the mesa definition the sample was ready for the back surface deposition. Typically the back surface did not require any further cleaning as any blemishes on the surface were removed during the mesa etching. The metal contact was deposited in a multi-source evaporator system. The sample was placed on a semi-spherical rotating stage and the chamber was subsequently brought to a vacuum. The metal sources to be deposited were moved into position underneath the sample in order of deposition and were heated using an electron beam. The deposition rate was controlled with the aid of a film thickness monitor, which stopped the deposition depending on the inputted desired thickness.

For an n-type GaAs substrate the typical contact deposited consists of 170$\mathring{A}$ Ge, 480$\mathring{A}$ Au, 170$\mathring{A}$ Ni and 2000$\mathring{A}$ Au which create an ohmic type contact.

The dominant carrier transport mechanism in this type of contact is quantum tunnelling.

2.10 Rapid Thermal Annealing and Device Separation

Both the top surface and back surface contacts were annealed simultaneously. The sample was placed in a small chamber with a dry nitrogen gas atmosphere. It was subsequently heated rapidly from room temperature to 420°C and cooled back down. This created an anneal ramp from 400 to 420°C and cooled back down to 400°C which lasted approximately 20 seconds. This allowed annealing of the front and rear gold metallisation and also for Ge diffusion in the back surface contact to create the n+ GaAs region.
A scoring and cleaving method was used to separate the devices. A Karl Zeiss diamond tipped scribe was used to score the devices in the intermediate space between them. The cleaving as performed on a blunt knife edge; the sample was placed on a taut acetate plastic strip and pressed upon the blunt knife edge along the score line until cleaved. The scoring of the devices could also be performed prior to the back surface contact deposition.

2.11 Device Mounting

2.11.1 Photodiodes and Fully Metallized Devices

The photodiodes and fully metallized devices were mounted on standard TO5 12-pin headers. Typically four cells were mounted on a single header; two photodiodes and their corresponding fully metallized devices. The devices were glued on the TO5 header using a silver conductive paint. They were subsequently bonded to the pads in a '4-point measurement' configuration.

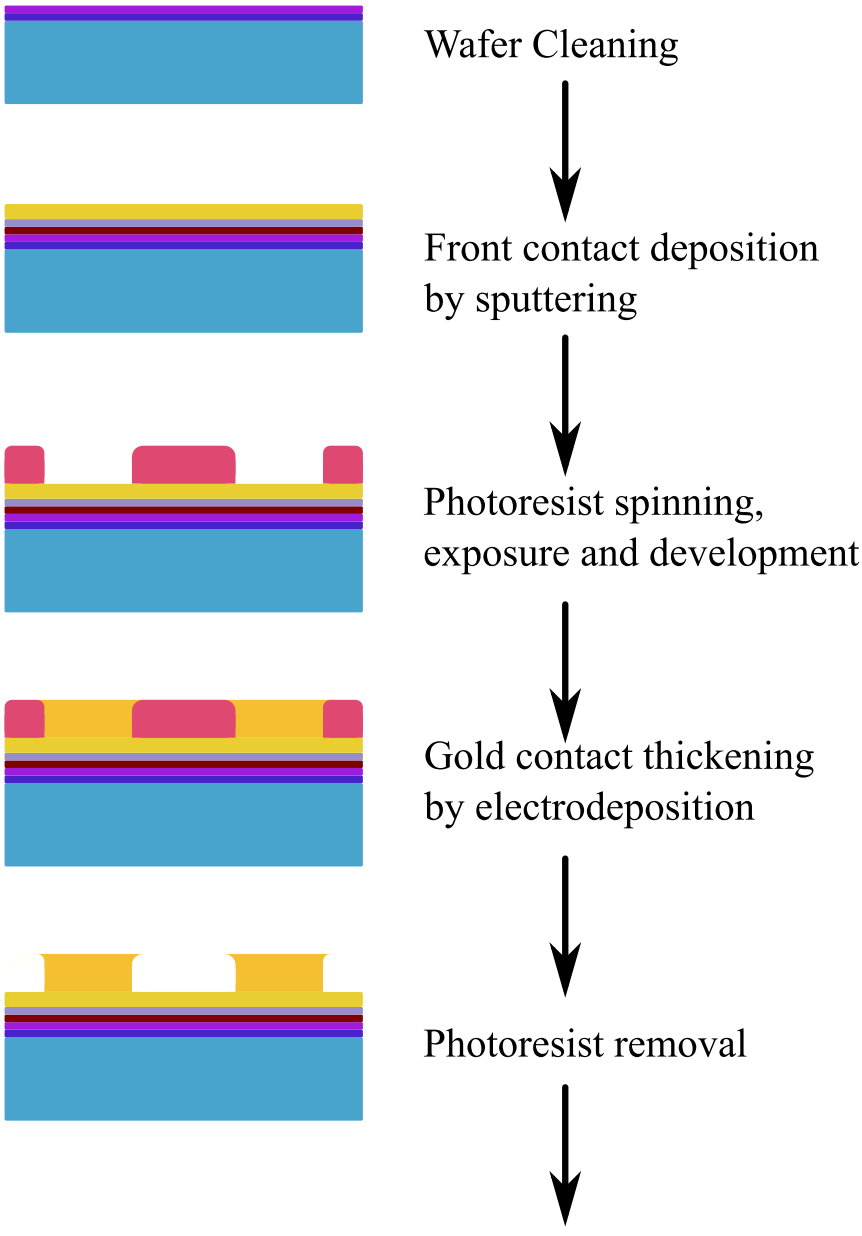
The bonding was performed using an ultrasonic wire bonder and 25μm diameter gold wires with two wires bonded for each connection.

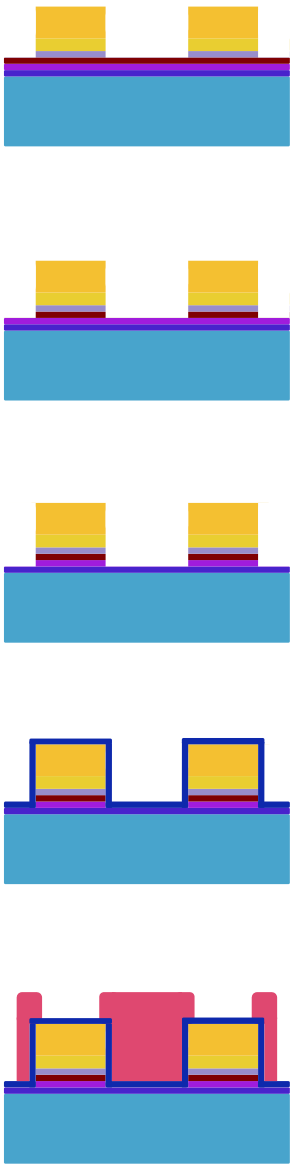
2.11.2 Concentrator Devices Mounting

Due to the high heat dissipation at high concentrations the concentrator devices required mounting on copper disc which acted as a heatsink. Each 25mm copper disc had two holes to allow mounting. Typically either one or two devices were mounted on a single copper disc. Prior to mounting the copper disc was polished using a grade 1000 sandpaper. This removed any oxides and allowed better bonding of the devices to the disc which also acquired a polished appearance.
Front contacts were prepared using silicon wafers which were coated with a silicon oxide and then gold plated on both sides. The copper block was placed on a hot plate with the front contact pads and the contact wires placed on the block with slivers of flux-cored solder wire underneath them. Once the solder wire melted and bonding occurred the copper block was removed from the hot plate and placed on a much larger copper block to dissipate the heat quickly and avoid excess heat treatment and tarnishing of the block. The device was mounted on the block using a silver conductive paint. Depending on the concentration level the device was to be characterised, 20 to 50 bond wires were placed from the device busbar to the front surface conducting pad. More than one pad was used if bonding all around the device was required. The pairs of contact wires were used to enable the performance of 4-point measurements.

2.12 Summary of processing

The schematic in Figure 2.12 shows the main stages in the processing chain.


Wafer Cleaning
Front contact deposition
by sputtering
Photoresist spinning,
exposure and development
Gold contact thickening
by electrodeposition
Photoresist removal



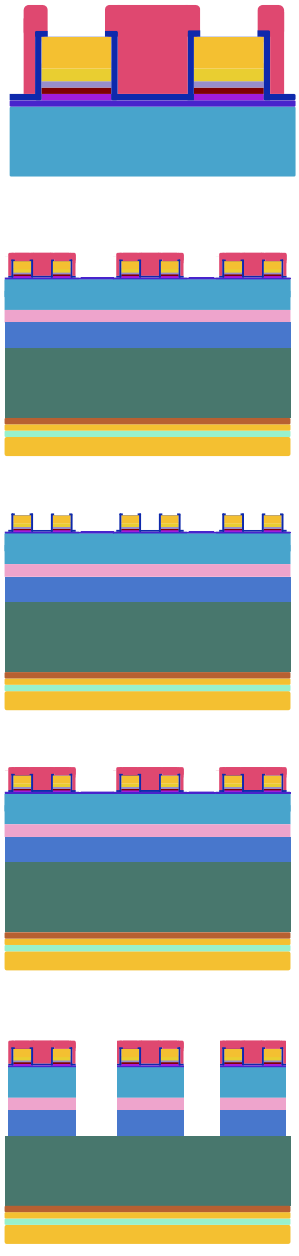
Dry etching of Au and Pt

Dry etching of Ti

Cap removal

Anti-reflection coating deposition

Photoresist coating and exposure of contact openings



A-R coat dry etch
(opening contacts)

Back contact depositon

Photoresist removal

Photoresist spining, mesa
definition and exposure.

Mesa wet etch

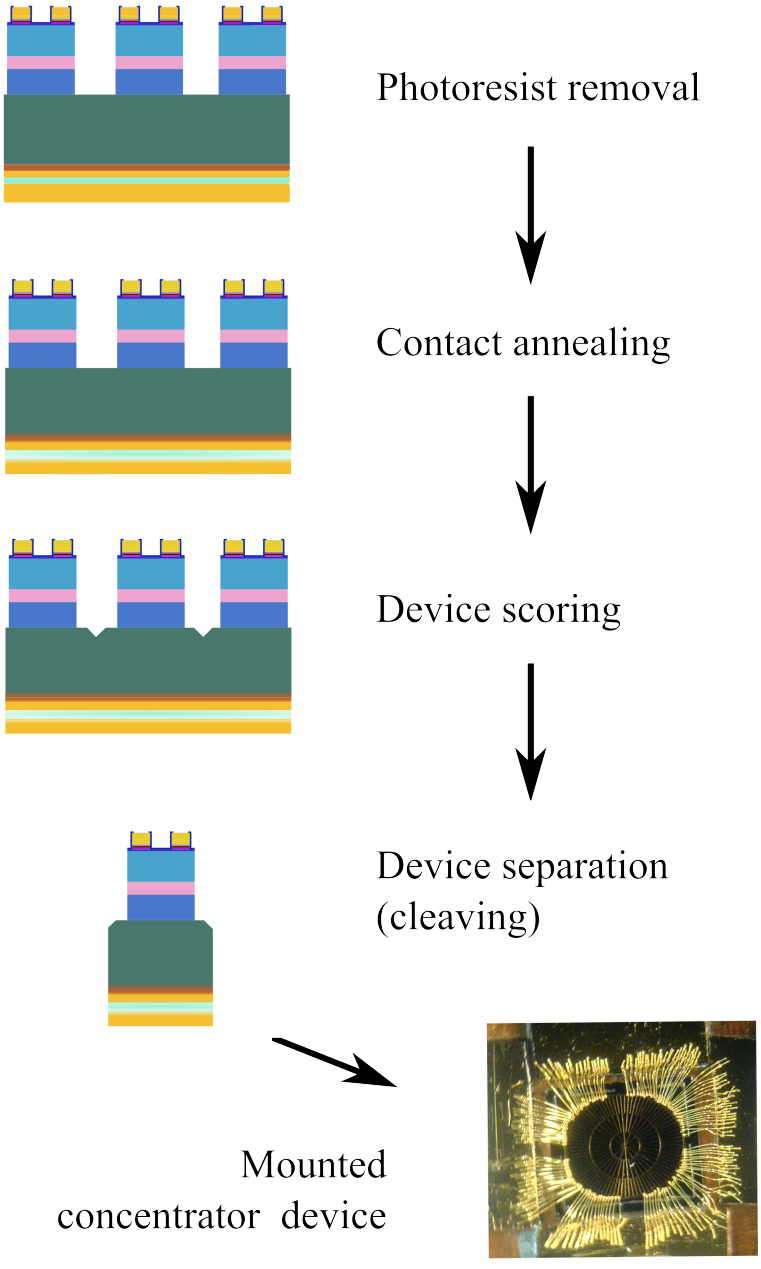


Figure 2.3: Processing steps.

Bibliography

[1] G. Stareev, "Formation of extremely Low resistance Ti/Pt/Au ohmic contacts to p-GaAs," *Applied Physics Letters*, vol. 62, no. 22, pp. 2801–03, 1993.

[2] A. Katz, C. R. Abernathy, and S. J. Pearton, "Pt/Ti ohmic contacts to ultrahigh carbon-doped p-GaAs formed by rapid thermal processing," *Applied Physics Letters*, vol. 56, pp. 1028–1030, March 1990.

[3] C. Algora and V. Diaz, "Influence of series resistance on guidelines for manufacture of concentrator p-on-n gaas solar cells," *Progress in Photovoltaics: Research and Applications*, vol. 8, no. 2, pp. 221–225, 2000.

[4] T. N. D. Tibbits, *Optimisation of strain-balanced quantum well solar cells for concentrator and multijunction (tandem) structures*. PhD thesis, Imperial College of Science, May 2006.

[5] M. J. Madou, *Fundamentals of Microfabrication: The Science of Miniaturization, Second Edition*. Taylor & Francis, 2nd ed., 2002.

[6] W. Ruythooren, K. Attenborough, S. Beerten, P. Merken, J. Fransaer, E. Beyne, C. V. Hoof, J. D. Boeck, and J. P. Celis, "Electrodeposition for the synthesis of microsystems," *Journal of Micromechanics and Microengineering*, vol. 10, no. 2, p. 101, 2000.

[7] G. M. Peake, S. J. Sun, and S. D. Hersee, "GaAs microlens arrays grown by shadow masked MOVPE," *Journal of Electronic Materials*, vol. 26, no. 10, 1997.

[8] R. Williams, *Modern GaAs Processing Methods*. Boston: Artech House, 2nd ed., 1990.

[9] A. R. Clawson, "Guide to references on III-V semiconductor chemical etching," *Materials Science and Engineering*, vol. 31, pp. 1–438, January 2001.

Chapter 3

Multi-junction MQW Solar Cell Characterisation

3.1 Introduction

This chapter describes the measurements that are crucial to the understanding of solar cell performance. The dark current as a function of cell bias and internal quantum efficiency (IQE) as a function of the wavelength of the absorbed photons can be compared with the simulation program SOL thus making it possible to understand cell performance in terms of the basic semiconductor parameters as described in Chapter 4. Different methods for determining cell efficiency were used and assessed. Electroluminescence images aided the device processing procedure as it provided visual feedback on device quality.

3.2 Dark Currents Measurements

The dark current measurement determines the inherent current generated in the device when this is subjected to a forward bias voltage with no photocurrent generation i.e. in the 'dark'. This measurement helps to determine

the amount of series and shunt resistance present in the device and is an initial indication of a 'good' or 'bad' device. The device under test can be mounted on a Peltier cooling stage whose temperature is controlled by a platinum resistance thermometer and monitored on a Keithley digital multimeter (DMM). The device temperature is kept constant at $(25 \pm 0.1)^{\circ}$C in order to comply with standard testing conditions. The measurements are performed by a Keithley source measure unit (SMU) Model 238 or 2410. Both instruments are computer controlled via a general purpose interface bus (GPIB). The software for the control and data acquisition were developed by Dr. D. Bushnell [1]. Two-point or four-point measurements can be used with the latter having the advantage of eliminating lead resistance effects such as voltage drops on the leads or connections to the device. Furthermore, fully metallised devices are used in order to eliminate the effects of emitter spreading resistance. Pulsed measurements can also be employed at high bias. This is necessary to minimise heating effects generated by the high current levels. This method can also be employed on unmounted samples using a probe method. The flexibility and ease of the measurement process enables it to be used on samples in mid-processing to determine processing quality.

3.3 External Quantum Efficiency Measurements

The IQE of a sub-cell of a tandem device is defined in Equation 4.1 in Chapter 4. The challenge in measuring the quantum efficiency of dual junction tandem cells arises from the fact that the junctions are connected in series. According to Kirchoff's rules, the output current is limited by the least producing junction, therefore during characterisation, the junction not under test will not pass any current unless illuminated. To overcome this, a light-bias needs to be applied to the junction not under test without affecting the junction being characterised [2]. For this purpose a blue LED (470nm) was

used as the light bias source for the top cell and a red LED (750nm) for the bottom cell. This system, which was developed by Dr. T. Tibbits [3], enabled the QPV group to make QE measurements on tandem cells for the first time.
The complete setup for the quantum efficiency measurements is shown in Figure 3.1 below.

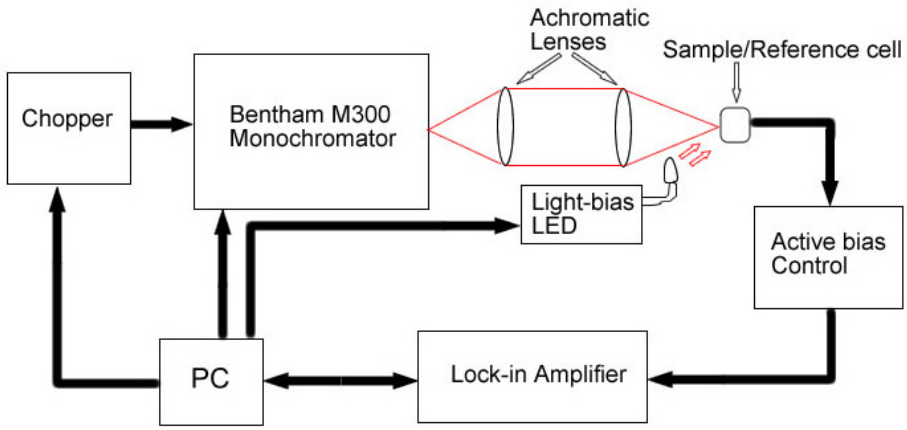


Figure 3.1: Experimental setup for multi-junction cell external quantum efficiency measurements.

A lock-in technique is used for the measurements in order to reduce background signal noise and obtain valid results even at low intensity measurements. Also the lock-in technique makes it possible to distinguish between the monochromator signal and the external light bias.
A tungsten light source chopped at 165Hz (frequency depends on lab conditions) is coupled into a Bentham M300 monochromator. Monochromatic light output from the 0.2mm exit pinhole is then focused onto the sample using an achromatic pair of lenses. Meanwhile the sample is kept at a constant voltage bias of 0V using an active bias control. The output current is measured on a Stanford SR510 lock-in amplifier at the chopper frequency.

The measured photocurrent is then recorded on a PC through an IEEE-488 interface bus.

The procedure for measuring the top cell is as follows: The light bias LED, in this case the infra-red LED, is set at maximum intensity and a low resolution scan is performed at 20nm steps. The wavelength where the peak photocurrent occurs is determined and the monochromator is set at that value. The current through the LED is then increased from 0mA to 20mA while the photocurrent is recorded. The point of saturation of the photocurrent is then determined and the LED current is set at the specified level.The quantum efficiency scan is then performed at this light bias level ensuring that the top cell is always the current limiting cell.

It is important to determine the saturation point accurately due to the adverse effects that might occur due to over light biasing. Excessive light biasing will force the light-biased junction into forward voltage bias. This in turn will force the junction under test into reverse voltage bias as both junctions are kept at zero volts by the active bias control. For more accurate results the quantum efficiency scan can be broken up into several smaller scans where the photocurrent does not vary greatly and with the light bias LED set at values near the peak photocurrent for each scan.

Immediately after the QE scan another scan is performed over the full range, in this case in the absence of the light bias, with a calibrated reference photodiode of known response. The device quantum efficiency can be calculated by taking the ratio of the device photocurrent and the reference cell photocurrent as shown in Equation 3.1 below.

$$QE_{DEVICE}(\lambda) = \frac{I_{DEVICE}(\lambda) \times QE_{REF}(\lambda)}{I_{REF}(\lambda)} \tag{3.1}$$

The same procedure can be repeated for characterising the bottom cell using the blue light bias LED.

3.4 Reflectivity Measurements

Measuring the reflectivity of the devices provides vital information on two important aspects; the quality of the anti-reflection coating and the internal quantum efficiency of the device. The internal quantum efficiency is a vital measurement as it provides the ratio of converted photons into electrons over the total number of absorbed photons. Using the internal quantum efficiency direct comparison between different devices can be performed. In addition the IQE is directly related to the basic semiconductor parameters by the simulation programme SOL, as described in Chapter 4.
To measure the reflectivity of a device a similar setup to the quantum efficiency measurements is used as depicted in Figure 3.2 below.

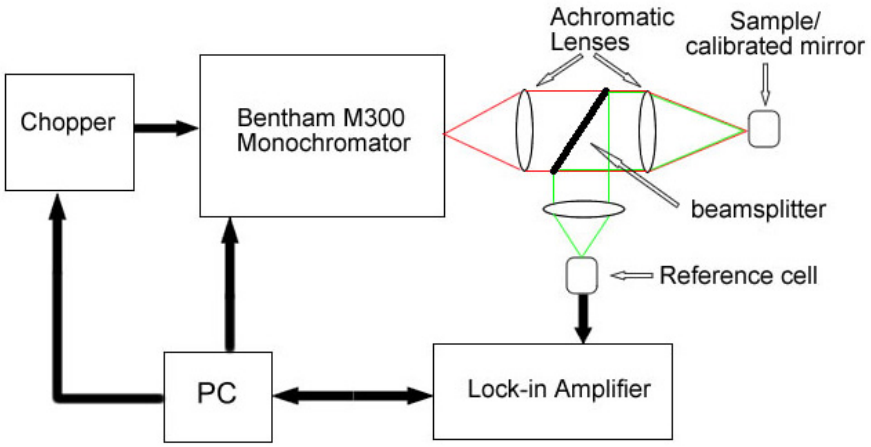


Figure 3.2: Reflectivity measurement setup.

The beam-splitter is used to guide the reflected light from the device onto the reference cell, which in turn is measured using the lock-in amplifier. The scan over the full wavelength range is repeated twice; once with the device and once with a calibrated mirror of known reflectivity. The reflectivity of the device is then calculated using Equation 3.2 below.

$$R_{DEVICE}(\lambda) = \frac{I_{DEVICE}(\lambda) \times REFL_{MIRROR}(\lambda)}{I_{MIRROR}(\lambda)} \tag{3.2}$$

The internal quantum efficiency is calculated using the following equation:

$$IQE(\lambda) = \frac{EQE}{1 - \frac{R(\lambda)}{100}} \tag{3.3}$$

Once the internal quantum efficiency is known an ideal anti-reflection coating can be applied to the device IQE. The ideal external quantum efficiencies obtained in this fashion can be used to calculate ideal short circuit current densities under various spectra using Eq. 1.3.

3.5 Light I-V measurements

The benchmark test for solar cell performance is the I-V measurement under illumination. This test provides the maximum conversion efficiency of the cell under a specific illumination condition. Terrestrial solar cells are characterised using AM.15g spectrum whereas AM1.5d spectrum is used for concentrator solar cells at various concentration levels. The characterisation spectrum needs to be closely matched to the standard spectrum. This is more significant in the case of multi-junction cell characterisation as slight changes in the spectrum shape can result into significant shifts in efficiency. Two methods were used for the light IV characterisation: a dual monochromatic source setup was used for low concentration measurements and a xenon source was used for a wider range of concentration levels.

3.5.1 Dual Monochromatic Characterisation

In the absence of a light source matching the standard AM1.5 spectra or a multi-source solar simulator a different approach was used in performing low concentration IV measurements. The main idea, as proposed by Dr. Tibbits

[3], was to simulate the photocurrent from each junction expected under AM1.5g conditions with two distinct laser sources centred at each junction's spectral response. For the purposes of this measurement a blue, 404nm laser and a near-infra-red, 780nm laser were used.

Having already measured the external quantum efficiency of the device, the photocurrent produced by each junction under AM1.5g conditions can be calculated by the convolution of the EQE and AM1.5g standard spectrum using Eq. 1.3. The photocurrent expected from the device is equal to the lowest current producing junction as the junctions are in series. The procedure depends on which junction is current limiting the device. For a top cell limited dual-junction device the procedure is as follows:

Both lasers are set to maximum intensity in order for the short-circuit current to be higher than the calculated current expected from the bottom cell. The intensity of the near-infra-red laser is then driven down so that the current output matches the calculated short circuit current of the bottom cell. The tandem cell is now bottom cell limited. The blue laser intensity is then adjusted until the current output matches the calculated top cell photocurrent thus making the tandem cell top cell limited. At this stage both junctions are biased as if under AM1.5g spectral conditions and the photocurrent equals the expected device photocurrent. By performing a voltage sweep and recording the current in a similar fashion as the dark current measurements a light I-V curve can then be obtained.

In a similar fashion a bottom cell limited dual-junction solar cell can be characterised by reversing the order that the laser intensities are adjusted. This method provides accurate results as compared with measurements performed using an AM1.5g source despite the uncertainty in calibrating the light intensity of the two laser sources to match the spectrum. The major limitation of this method is the maximum intensity provided by the laser sources at hand which limited the maximum concentration possible. For larger devices this method would not be cost effective due to the need of large area, high inten-

sity lasers. The simplicity of the method eliminates the need for multi-source solar simulators and single source simulators with bias light adjustment [4].

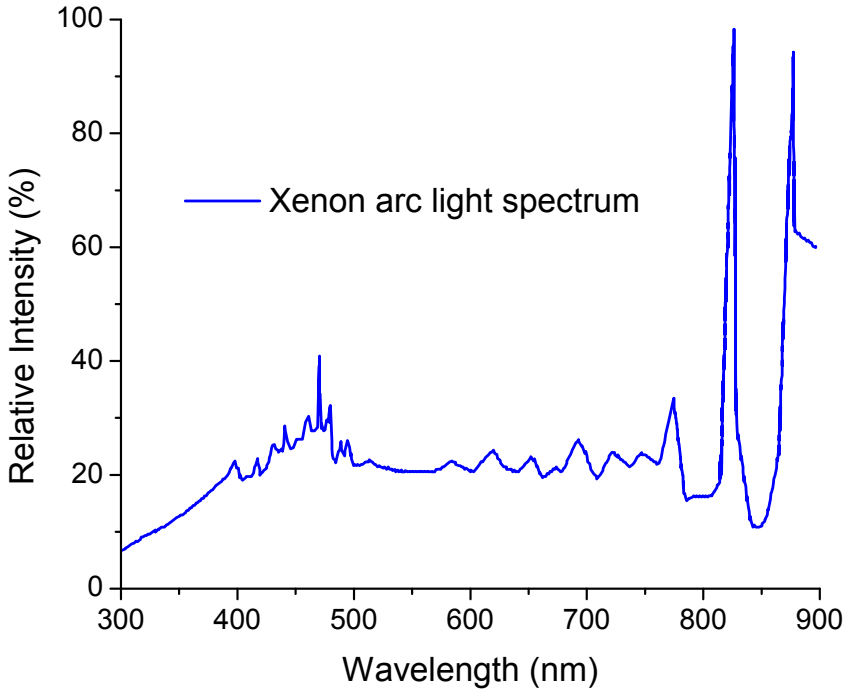


Figure 3.3: Xenon arc lamp spectrum.

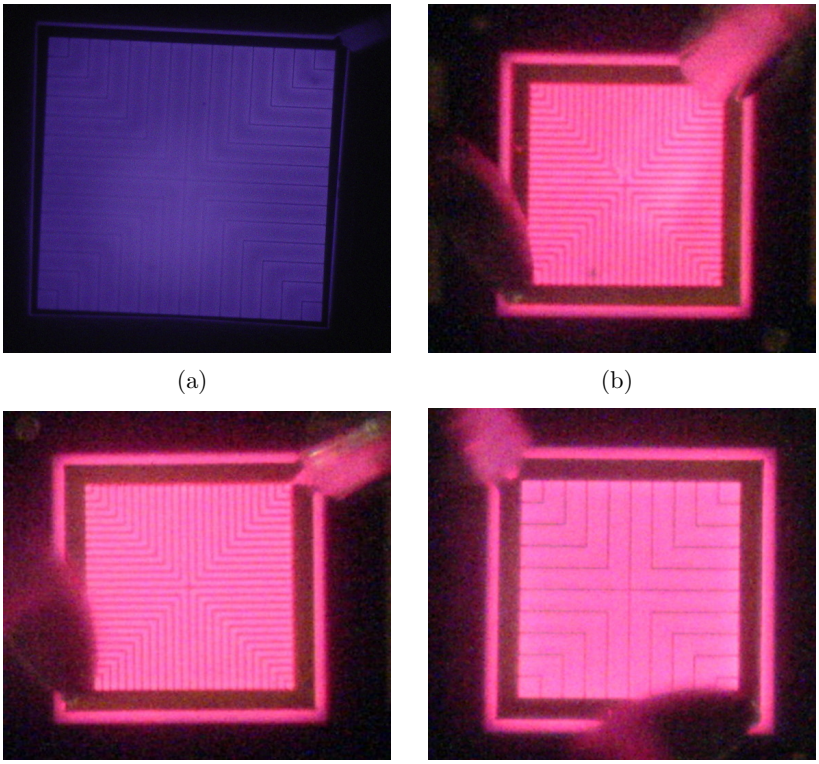
3.5.2 Xenon Source Characterisation

Xenon arc light sources provide a continuous light spectrum that is necessary to simulate the solar spectrum. This spectrum, as seen in Figure 3.3, contains a number of peaks in the near-infrared region. Several filters can be utilised in order to remove these peaks and adjust the spectral shape for a close matching to the AM1.5g spectrum. A single water filter [5] can reproduce some of the absorption effects produced by the earth's atmosphere. Using suitable optics the concentration level of the xenon light source can be

adjusted and concentration levels up to 1000x can be achieved. This characterisation was performed in collaboration with ENE which possessed a Xenon source solar simulator.

3.6 Electroluminescence

Electroluminescence images provide visual information on the quality of the solar cells. By sourcing a current through a solar cell light emission is generated in the reciprocal way photocurrent is generated by light absorption. Several electroluminescence images are depicted in Figure 3.4 below.
Dark patches depict areas that have poor emission thus poor absorption or high losses. By using different filters distinctions in the absorption of different wavelengths can be made qualitatively. This procedure was useful to visually assess the concentrator devices fabricated as described in Chapter 2.



(a) (b)

(c) (d)

Figure 3.4: Electroluminescence images of concentrator cells. Darker patches denote poor absorption or high losses.

Bibliography

[1] D. B. Bushnell, *Optimisation of strain-compensated multi-quantum well solar cells*. PhD thesis, Imperial College of Science, Technology and Medicine, University of London, 2003.

[2] G. F. Virshup, "Measurement techniques for multijunction solar cells," in *Photovoltaic Specialists Conference, 1990., Conference Record of the Twenty First IEEE*, vol. 2, pp. 1249–1255, 1990.

[3] T. N. D. Tibbits, *Optimisation of strain-balanced quantum well solar cells for concentrator and multijunction (tandem) structures*. PhD thesis, Imperial College of Science, May 2006.

[4] S. Kurtz, K. Emery, and J. Olson, "Methods for analysis of two-functional, two-terminal photovoltaic devices," in *Photovoltaic Energy Conversion, 1994., Conference Record of the Twenty Fourth. IEEE Photovoltaic Specialists Conference - 1994, 1994 IEEE First World Conference on*, vol. 2, pp. 1733–1737, 1994.

[5] Newport Corporation, "Newport Resource e-Catalog," 2015.

Chapter 4

Device Modelling

Over the past two decades a detailed simulation model named SOL, has been developed at Imperial. SOL can perform simulations and fits to real device experimental data and in addition can be used as a tool for the design and simulation of new devices. It can perform simulations for both quantum efficiency and dark current behaviour of lattice matched, strained and strained-balanced MQW solar cells. SOL has been used throughout the project to simulate experimental data and perform predictions on future devices.

4.1 Introduction to SOL

Originally developed by Dr. J. Nelson in FORTRAN the model has been steadily developed in the Quantum Photovoltaics Group of Imperial College for over 15 years. SOL is considered to be an analytical model which explores the physical phenomena taking place rather than performing exact numerical methods [1]. Using numerical methods, SOL solves the transport equations of the modelled device in order to extract the quantum efficiency. In order to enable the analytic solution of the transport equations the model assumes uniform doping, low injection and abrupt changes in composition at the

heterojunctions. The fact that the model uses an analytical approach it limits the accuracy of the model. This however increases the understanding of the underlying physical phenomena. Recent improvements to the model by Dr. J. P. Connolly have allowed modelling of multi-junction devices. The quantum efficiency of each junction was calculated in series taking into account the absorption of the preceding junctions.

4.2 Quantum Efficiency Modelling

SOL simulates internal quantum efficiency (IQE) and the dark current. The IQE can then be converted to an external quantum efficiency (EQE) with measured or ideal anti-reflection coefficients as described in Section 3.4. It uses parameters from fitting the IQE in the simulations for fitting the dark current. Therefore accurate modelling of the quantum efficiency is necessary for fitting the dark current. The following sections analyse the key features of SOL used to model the quantum efficiency.

4.2.1 IQE Modelling of p- and n-regions

The IQE contribution in the p- and n-regions is largely determined by the minority carrier diffusion lengths. The IQE can be derived by evaluating the spectral photocurrent $J(\lambda)$ which in the p-region is given according to Equation 4.1 below as given by Lumb et al. [2]:

$$J_p(\lambda) = qF_0(\lambda)\left\{\frac{L_pF_1(\lambda) + \frac{S_pL_p}{D_p}F_2(\lambda) - F_3(\lambda)\left(sinh\frac{d_p}{L_p} + \frac{S_pL_p}{D_p}cosh\frac{d_p}{L_p}\right)}{\left(cosh\frac{d_p}{L_p} + \frac{S_pL_p}{D_p}sinh\frac{d_p}{L_p}\right)} - L_pF_4(\lambda)\right\} \tag{4.1}$$

where D_p is the minority carrier diffusion coefficient, L_p is the minority carrier diffusion length in the p-region. S_p is the surface recombination velocity at

the interface between the high band-gap window or minority carrier reflector and the p-region and d_p is the quasi-neutral region in the emitter. The $F(\lambda)$ are absorption factors listed by Lumb et al as shown below.

$$F_0(\lambda) = \frac{L_p(1-R_1)\alpha\phi_0}{(1-\alpha^2 L_p^2)} \tag{4.2}$$

$$F_1(\lambda) = \alpha \tag{4.3}$$

$$F_2(\lambda) = 1 \tag{4.4}$$

$$F_3(\lambda) = e^{-\alpha d_p} \tag{4.5}$$

$$F_4(\lambda) = \alpha e^{-\alpha d_p} \tag{4.6}$$

Here α is the absorption coefficient of the material, ϕ_0 is the incident flux and R_1 is the front surface reflectivity. A similar expression holds for the n-region.

In SOL the diffusion length can be manually determined or calculated using the material parameters. Equally important is the determination of the surface recombination velocities, S_p and S_n for accurate fit of the QE. The effects of the diffusion length and recombination velocity on the contributions are depicted in Figure 4.1. It can be seen that there is a trade-off between the two parameters which requires data on different region thicknesses (d_1) studied in a number of earlier PhD theses from the Imperial group.

4.2.2 QE Modelling of i-region

SOL assumes that, in the presence of a built-in field, all photo-generated carriers reaching the depletion region or generated in the depletion region are collected. The IQE in the intrinsic region is mainly determined by the quan-

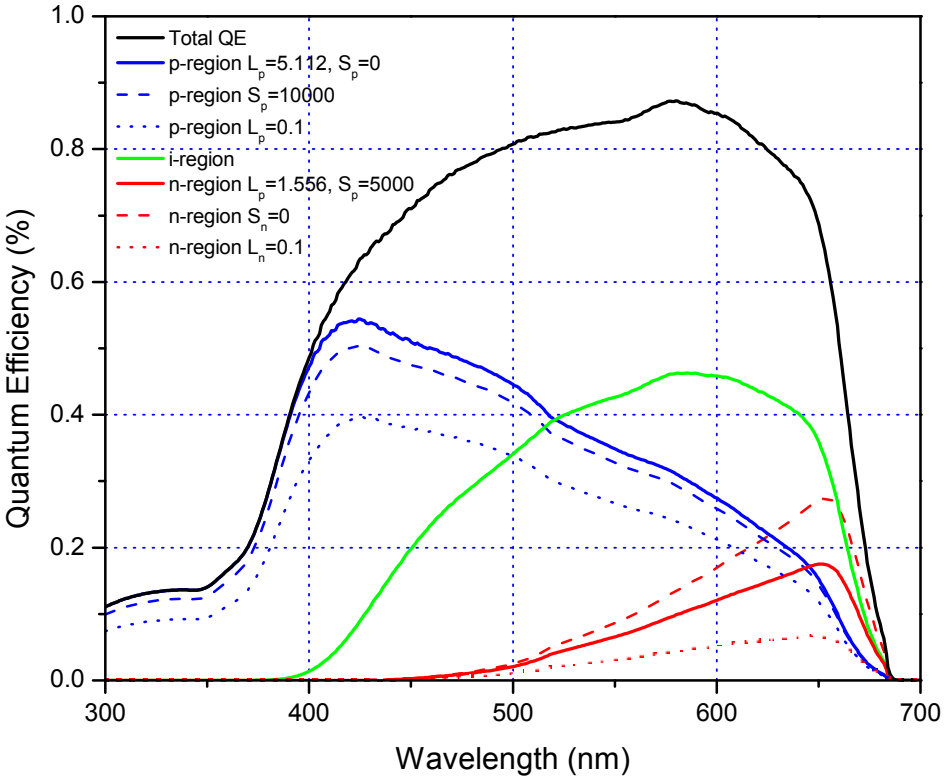


Figure 4.1: Effect of diffusion lengths and surface recombination on p- and n-regions. The total QE depicted is the SOL model output based on the growth details of device Qt1821AD. The contribution of each region is depicted and the model prediction for various diffusion lengths and surface recombination.

tum well absorption. Using a first-principles quantum mechanical approach the energy levels of the quantum wells are calculated. The density of states of a QW within the envelope function approximation are calculated using the boundary conditions as set by Bastard [3] and solving the one-dimensional Schrödinger equation for a finite square well. The built-in field across the depletion region is small and can thus be neglected.

The photogenerated carriers in the depletion region are defined by Equation

4.7 shown below as described by Paxman et al. [4].

$$J_{dr} = qF(\lambda)[1 - R(\lambda)]e^{-\sum z_j \alpha_j} \times (1 - e^{-\alpha_p w_p - \alpha_j z_j - \alpha_n w_n}) \tag{4.7}$$

where $R(\lambda)$ is the surface reflectivity, α_p and α_n the absorption coefficients in the p- and n-regions respectively and $\alpha_i z_i$ the optical depth of the intrinsic region. In the case of MQW present in the intrinsic region the equation becomes

$$J_{dr} = qF(\lambda)[1 - R(\lambda)]e^{-\sum z_j \alpha_j} \times (1 - e^{-\alpha_p w_p - N(\alpha_w L_w + \alpha_b L_b) - \alpha_n w_n}) \tag{4.8}$$

where N is the number of quantum wells, α_w and α_b the well and barrier absorption coefficients and L_w and L_b the corresponding diffusion lengths. The total current produced in the device is therefore defined as

$$J_{sc}(\lambda) = f_i[J_n(\lambda) + J_p(\lambda) + J_{dr}(\lambda)] \tag{4.9}$$

where f_i is a transport factor to account for intrinsic region recombination losses. Assuming an electric field is maintained across the depletion region f_i is assumed to be unity. Finally the quantum efficiency can be calculated using the incident spectrum flux $F(\lambda)$

$$IQE(\lambda) = \frac{J_{sc}(\lambda)}{qF(\lambda)} \tag{4.10}$$

4.3 Dark Current Modelling

In order to fit the dark current we assume that ideality $n \sim 2$ dominates in the low bias region and ideality $n = 1$ dominates in the high bias region. The $n = 1$ high bias dark current comprises of two contributions: the radiative

recombination contribution and the ideal Shockley injection current.

4.3.1 Dark Current in the depletion region

Modeling the low bias ideality $n \sim 2$ region is made possible by using a one parameter effective lifetime fit. Assuming the depletion approximation holds and using the QW states based on the energy levels calculated in the IQE, SOL calculates the variation in the carrier distributions n(x) and p(x) with position x throughout the i-region. Using the Shockley-Hall-Read (SHR) approach, a recombination rate can be determined from the carrier densities. The SHR approach requires the non-radiative lifetimes of the carriers. It has been found [5] that the electron and hole lifetimes can be equated thus leaving only two parameters that depend on the material quality these being the carrier lifetimes in the barrier τ_b and the well τ_w. Having no bulk material with similar band gap to the QW and barrier, an assumption is made that for low P and In fractions the lifetimes τ_b and τ_w are equal since the well and barrier quality is the almost the same.
Figure 4.2 below depicts dark current fitting with no attempt to fit the high bias region where $n = 1$ dominates and SOL makes predictions from QE fit as discussed later. As can been seen a good fit is achieved in the low bias region where SHR recombination dominates with one parameter fit.

4.3.2 Radiative Dark Current

The first contribution is radiative recombination in the QW and barriers in the depletion region. The electron in the lowest energy state in the conduction band well and the hole in the highest energy state in the valence band well exhibit the highest probability for radiative recombination. This energy E_a is depicted in Figure 4.3 which shows the energy band diagram of a p-i-n QWSC. This contribution can be estimated using a detailed balance argument relating the photons absorbed to the photons radiated as discussed in

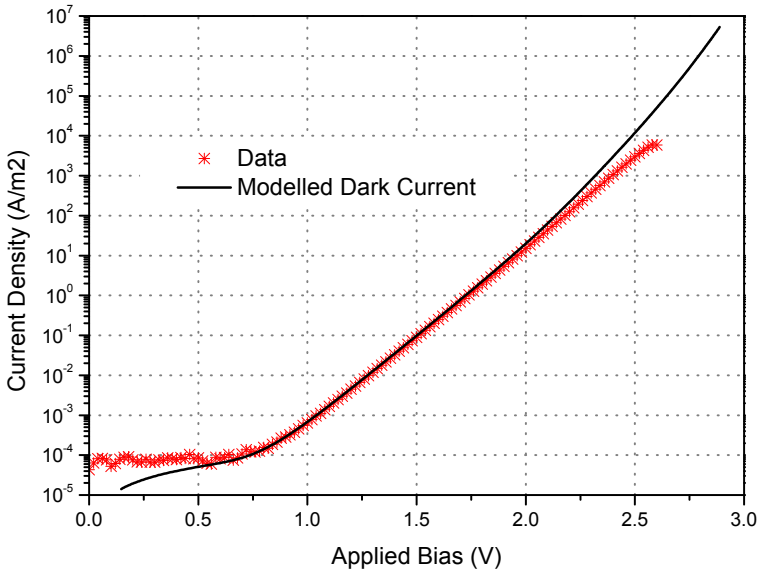


Figure 4.2: Dark current fitting of the low bias region ($n \approx 2$) based on one parameter fit. Fitting based on TS151 data and fitting parameters with $R_{s=0}\Omega$.

Nelson et al. [6]. The generalised Planck equation determines the radiated spectrum, $L(E,F)dE$ as a function of photon energy E in an electrostatic field F as follows:

$$L(E,F)dE = \frac{2\pi n^2 L_W}{h^3 c^2} \frac{\alpha(E,F)E^2}{e^{(E-\Delta E_F/k_B T}-1} dE \tag{4.11}$$

where ΔE_F is the quasi-Fermi level separation and $\alpha(E,F)$ the absorption coefficient as a function of energy and field. The total radiative current is derived by integrating this spectrum over the energy and cell geometry as described by Nelson et al. [6]. The absorption coefficient $\alpha(E,F)$ is calculated from first principles and can be compared with the measured IQE assuming the efficiency of escape from the wells (f_i in Eq. 4.9) equals one. This function peaks at energy $E_a$in Figure 4.3, so the radiative current is determined by how well the $\alpha(E,F)$ calculated from first principles fits the

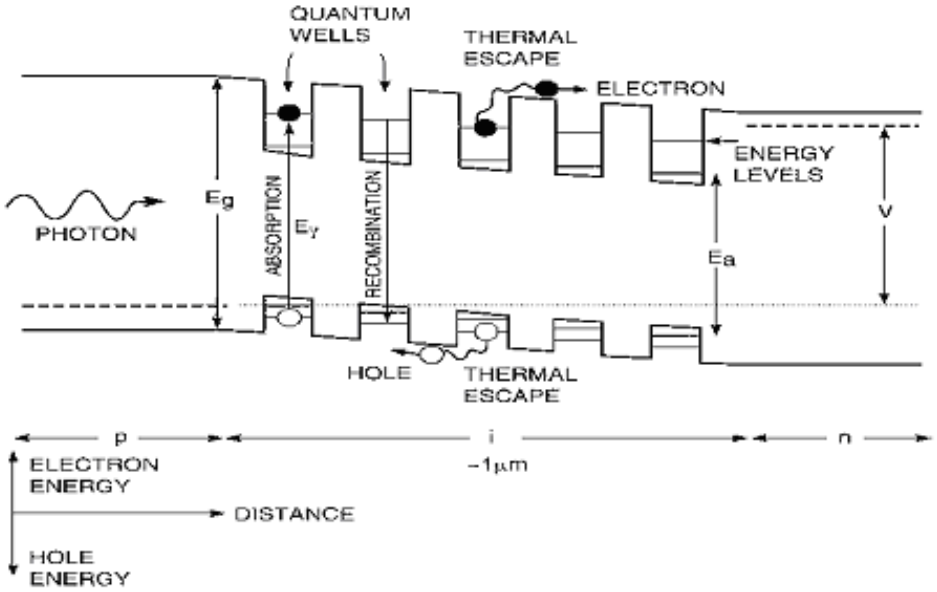


Figure 4.3: Energy band edge diagram of a p-i-n QWSC [7].

experimental QE at the bottom of the quantum well. The radiative current contribution to the dark current in SOL is therefore essentially a prediction [5]. It does not depend on any parameters if the QE fits at long wavelength.

4.3.3 Ideal Shockley Dark Current

The second contribution to the $n = 1$ is the ideal Shockley injection current. This contribution arises from the radiative and non-radiative recombination of injected minority carriers with the majority carriers in the field-free regions. The magnitude of the contribution depends on the minority carrier diffusion lengths, the doping levels and the surface recombination as described by Equation 4.12 below [1].

$$J_S(V) = q(e^{\frac{qV}{K_B T}} - 1) \left[\begin{array}{l} \frac{n_{ip}^2}{N_A}\frac{D_n}{L_n}\left(\frac{\frac{S_n L_n}{D_n}cosh\frac{x_p}{L_n} + sinh\frac{x_p}{L_n}}{\frac{S_n L_n}{D_n}sinh\frac{x_p}{L_n} + cosh\frac{x_p}{L_n}}\right) \\ +\frac{n_{in}^2}{N_D}\frac{D_p}{L_p}\left(\frac{\frac{S_p L_p}{D_p}cosh\frac{x_n}{L_p} + sinh\frac{x_n}{L_p}}{\frac{S_p L_p}{D_p}sinh\frac{x_n}{L_p} + cosh\frac{x_n}{L_p}}\right) \end{array} \right] \tag{4.12}$$

where n_{ip}^2 and n_{in}^2 are the p and n intrinsic carrier concentrations, N_A and N_D the p and n doping concentrations, x_p and x_n the p and n layer widths and the other terms have their usual meaning as in Eq. 4.1. The current can therefore be estimated by obtaining the minority carrier parameters S_n, L_n, D_n and S_p, L_p, D_p in Eq. 4.1 from the spectral response fitting in the bulk regions of the cell as explained in Section 4.2.1. Therefore an accurate fit of the spectral response with SOL in the bulk and QW regions determines the injection and radiative $n = 1$ dark currents respectively without free parameters. As will be demonstrated in the next chapter, fitting the QE of a SB-MQW cell with SOL enables one to fit the dark current over many decades with only one effective lifetime in the $n \approx 2$ region.

4.4 Tandem Cell Modelling

In order to model tandem cells and obtain the separate characteristics of each junction, separate cells are created in SOL which are then modelled in series to assess the total effect. The top cell can be modelled on its own as the bottom cell has no effect on the top cell quantum efficiency. Tunnel junctions are modelled simply as parasitic absorbers, usually in the form of a cap layer, with no voltage loss in the junction. The quantum efficiency modelling of the bottom cell is performed using the resulting flux not absorbed by the top cell.

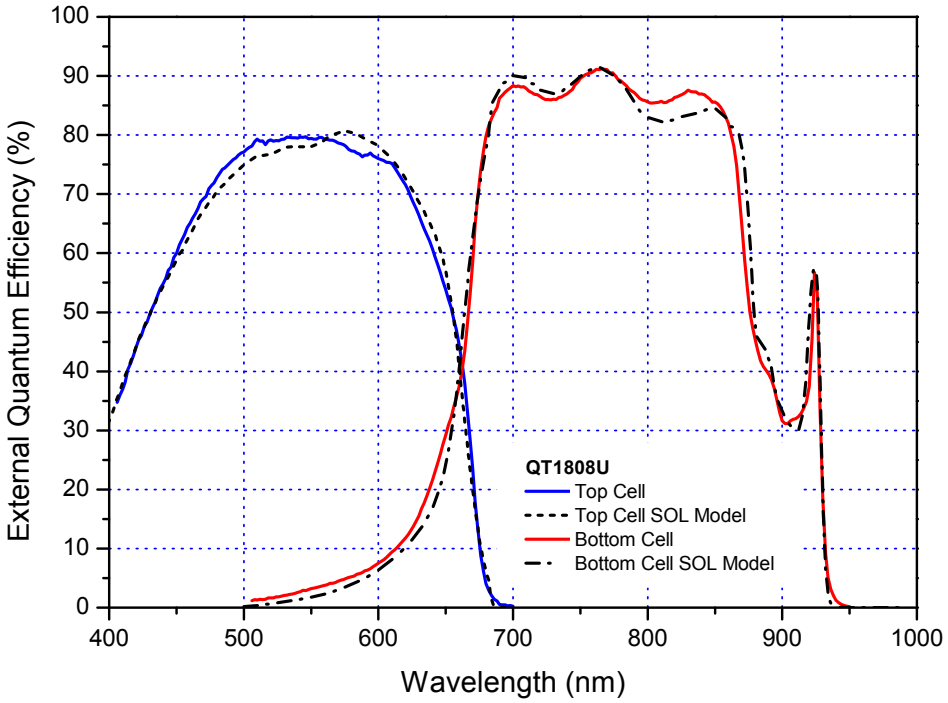


Figure 4.4: Measured and modelled tandem cell external quantum efficiencies of device Qt1808U.

Having also measured during characterisation, as described in Section 3.3, the individual cell quantum efficiency a direct comparison between model and experiment can be performed. Figure 4.4 depicts the measured and modelled quantum efficiency for tandem cell Qt1808U. The device structure and modelling data used can be found in Appendix B.

The short circuit current density is limited by the lowest current producing cell when the QE is integrated over the spectrum according to Equation 4.13 below:

$$J_{sc} = q \int F(\lambda) QE(\lambda) d\lambda \tag{4.13}$$

The dark current of the tandem cell is derived from the constituent cells by

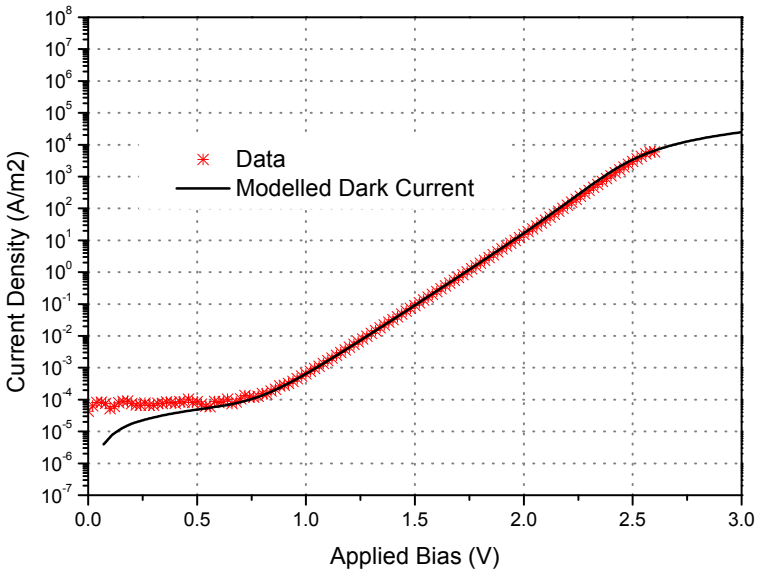


Figure 4.5: Tandem cell modelled dark current. Experimental data and model based on device TS151.

adding the voltage of each cell when the current from both cells is the same. Figure 4.5 illustrates the power of this fitting technique with the accurate fitting of the experimental data over the entire dark current range. Having the ability to model accurately the QE and dark current SOL can perform efficiency predictions using additivity as defined by Eq. 1.4.

4.5 Conclusions

In this chapter an analysis of SOL modelling has been presented. The important parameters for modelling the QE have been shown to be D the minority carrier diffusion coefficient, L the minority carrier diffusion length and S the surface recombination velocity. For the low bias region the dark current can be fitted using a single parameter, the carrier non-radiative recombination lifetime τ over many orders of magnitude. By fitting the quantum well re-

gion QE the radiative recombination contribution to the dark current can be determined. The last contribution to the dark current, the ideal Shockley injection current, according to Eq. 4.12, can be determined using the important parameters deduced from the QE fitting in the bulk regions. The power to model accurately the quantum efficiency and to predict the dark current establishes SOL as a powerful tool for developing future devices.

Bibliography

[1] J. P. Connolly, "Analytical Models of Bulk and Quantum Well Solar Cells and Relevance of the Radiative Limit," in *Advanced Solar Cell Materials, Technology, Modeling, and Simulation* (L. Fara and M. Yamaguchi, eds.), ch. 5, pp. 59–77, IGI Global, July 2012.

[2] M. P. Lumb, C. G. Bailey, J. G. J. Adams, G. Hillier, F. Tuminello, V. C. Elarde, and R. J. Walters, "Extending the 1-D Hovel Model for Coherent and Incoherent Back Reflections in Homojunction Solar Cells," *Quantum Electronics, IEEE Journal of*, vol. 49, pp. 462–470, May 2013.

[3] G. Bastard, *Wave Mechanics Applied to Semiconductor Heterostructures*. Editions de Physique, Paris, 1988.

[4] M. Paxman, J. Nelson, B. Braun, J. P. Connolly, K. W. J. Barnham, C. T. Foxon, and J. S. Roberts, "Modelling the spectral response of the quantum well solar cell," *Journal of Applied Physics*, vol. 74, pp. 614–621, July 1993.

[5] K. W. J. Barnham, I. M. Ballard, B. C. Browne, D. B. Bushnell, J. P. Connolly, N. J. Ekins-Daukes, M. Fuhrer, R. Ginige, G. Hill, A. Ioannides, D. C. Johnson, M. C. Lynch, M. Mazzer, J. S. Roberts, C. Rohr, and T. N. D. Tibbits, "Recent Progress in Quantum Well Solar Cells," in *Nanotechnology for Photovoltaics* (L. Tsakalakos, ed.), ch. 5, pp. 187–210, CRC Press, 2010.

[6] J. Nelson, J. Barnes, N. J. Ekins-Daukes, B. Kluftinger, E. Tsui, K. W. J. Barnham, C. T. Foxon, T. Cheng, and J. S. Roberts, "Observation of suppressed radiative recombination in single quantum well p-i-n photodiodes," *Journal of Applied Physics*, vol. 82, no. 12, pp. 6240–6246, 1997.

[7] K. W. J. Barnham, I. M. Ballard, J. P. Connolly, N. J. Ekins-Daukes, B. Kluftinger, J. Nelson, and C. Rohr, "Quantum Well Solar Cells," *Physica E*, vol. 14, no. 1, pp. 27–36, 2002.

Chapter 5

Tandem Cell Results

The emphasis of this project was placed on the optimisation of dual junction solar cells in a monolithic structure where the bottom cell incorporated a strain-balanced quantum well structure. This work was based on the previous theoretical work described in Chapter 1 and the preliminary experimental work performed by Tom Tibbits [1]. These were the first examples of tandem solar cell structures containing quantum wells grown anywhere. Several samples were grown, processed and characterised during the course of this project. The development of the samples was based on a feedback cycle as shown in Figure 5.1.

Using the modelling software SOL described in Chapter 4, a model of the device to be fabricated was created based on the parameters of previously grown devices. Once the desired device model was obtained the actual device structure was grown according to the model. The devices processed were then characterised both optically and electrically as described in Chapter 3. The results of the characterisation were compared to the model's expected results. The sample parameters i.e. p-i-n junction widths, were adjusted in order to agree with the growth parameters. In addition the material parameters used i.e. diffusion length, composition etc, were also adjusted accordingly in order to obtain accurate modelling of the experimental results. Using the

new model parameters optimised devices could then be modelled until the optimum device structure was achieved.

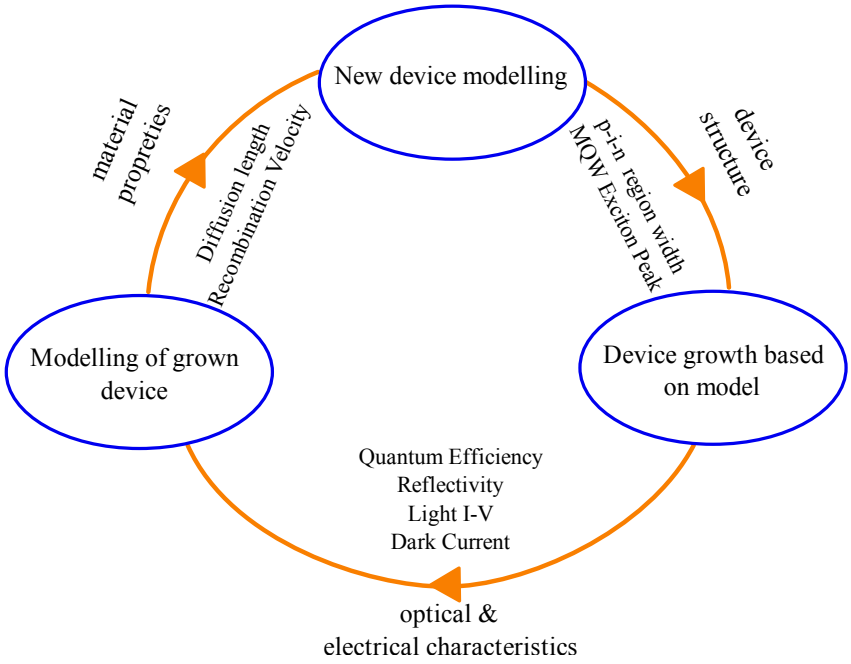


Figure 5.1: Device development cycle

The main focus of the project was to create a current matched dual-junction device. In order for this to be achieved the optimum band gap combination needed to be accomplished.

As described in Section 1.8.4, in traditional dual-junction InGaP-GaAs solar cells the current-limiting junction is the GaAs bottom cell. This however is not the case when a SB-MQW GaAs bottom cell is used. The current limiting junction is the InGaP top cell. Therefore the top cell had to designed in such a way in order to match the current produced in the strain balanced multi-quantum well bottom cell under AM1.5d conditions.

5.1 Device overview

The comprehensive list of devices fabricated for the purposes of this project are given in chronological order in Table 5.1 below. The major changes in each subsequent device growth are given in the table. The full growth details and the modelling parameters for all the devices presented in this thesis can be found in Appendix B.

Device	**InGaP Top Cell** (widths in microns)			**SB-MQW Bottom Cell**		**Remarks**
	p-region	i-region	n-region	**No. of Wells**	**Exciton Peak** (nm)	
Qt1808U	0.10	0.10	0.52	50	925	Sheffield grown bottom cell with ENE top cell overgrowth
ENE1595.4	0.10	0.20	0.57	0	—	ENE top cell with GaAs bottom cell
Qt1821AD	0.10	0.34	0.57	50	921	Low-doped top cell emitter
TS131	0.10	0.34	0.57	No bottom cell		Sheffield grown top cell
TS151	0.10	0.34	0.57	50	919	Sheffield grown bottom cell with ENE top cell overgrowth
ENE1864.1	0.10	0.34	0.57	0	—	ENE cell control cell for TS151

Table 5.1: Summary of fabricated devices.

5.2 Preliminary Devices

Preliminary results on the first tandems quantum well solar cells to be grown for the QPV group are presented in the thesis of Tom Tibbits [1]. These results have been used as the basis of further developments of tandem cells. These devices have been remeasured by the author and in addition detailed models in SOL have been developed.

During the course of that work two wafers, Qt1772AU and Qt1772AD, with a shallow MQW structure were grown at Sheffield along with their corresponding control p-n wafers Qt1772BU and Qt1772BD. A GaInP top cell overgrowth was subsequently performed at Energies Nouvelles et Environment (ENE) as at the time Sheffield had not developed a top cell or tunnel junction growth capability. The precise structure of the top cell overgrowth was not disclosed as it was covered by commercial confidentiality and an estimate of the top cell structure was determined by SOL modelling. An overview of the preliminary cell structures is given in Table 5.2 below.

Device		Qt1772AD	Qt1772AU	Qt1772BD	Qt1772BU
Top cell					
p	InGaP	0.30	0.15		
n	InGaP	0.82	0.47		
Bottom cell					
p	GaAs	0.50		0.50	
i	GaAs	1.285		No i-region	
n	GaAs	3.00		3.00	
Wells	InGaAs	50 wells, 0.83μm		No Wells	

Table 5.2: Preliminary Devices.

Both dual-junction MQW devices grown demonstrated a current limiting top InGaP junction. The thicker top cell of Qt1772AD indicated an enhanced longer wavelength absorption compared to the thin top cell of Qt1772AU. However it also showed a decrease in short wavelength absorption and thus

the overall efficiency of both devices was almost identical. Therefore a different approach was to be followed for subsequent devices.
This led to the development of Qt1808U which was the first tandem cell device to be designed by the author. As with the previous devices the bottom cell was grown at Sheffield and the top cell overgrowth was performed at ENE. The test devices were processed at Sheffield. The tandem cell structure of Qt1808U structure is depicted in Figure 5.2 below:

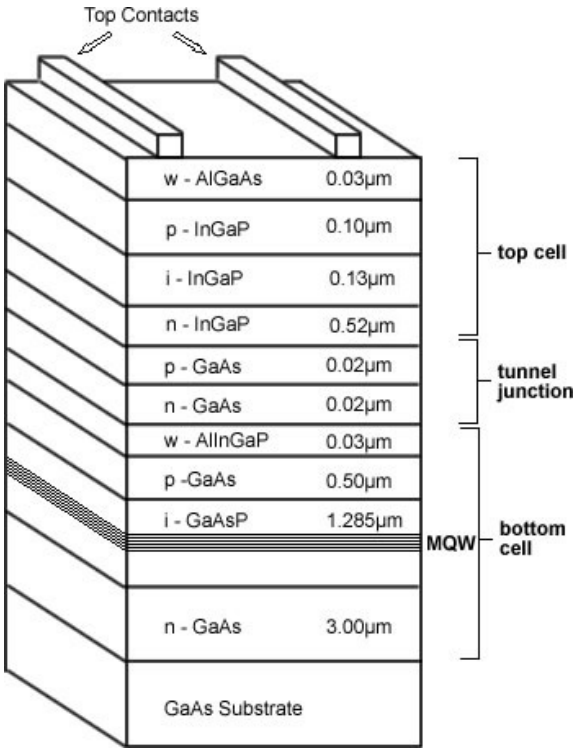


Figure 5.2: Qt1808U Device Structure.

The significant change in the device was the addition of an intrinsic region in the top InGaP cell which would extend the long wavelength absorption without affecting the emitter and the short wavelength absorption ability of the junction. The experimental EQE is depicted in Figure 5.3 below. The

modelled EQE using SOL is also depicted showing the contributions for the constituent regions of the top cell. The modelled EQE is within 1.0% of the experimental data. As in the case of the preliminary devices some parameters of the top cell growth were not disclosed by ENE due to commercial confidentiality. The accurate fitting of the EQE provided assumptions on these parameters such as the doping levels which where later on confirmed by ENE. The modelling results further justify in using SOL to perform predictions for a current-matching top cell.

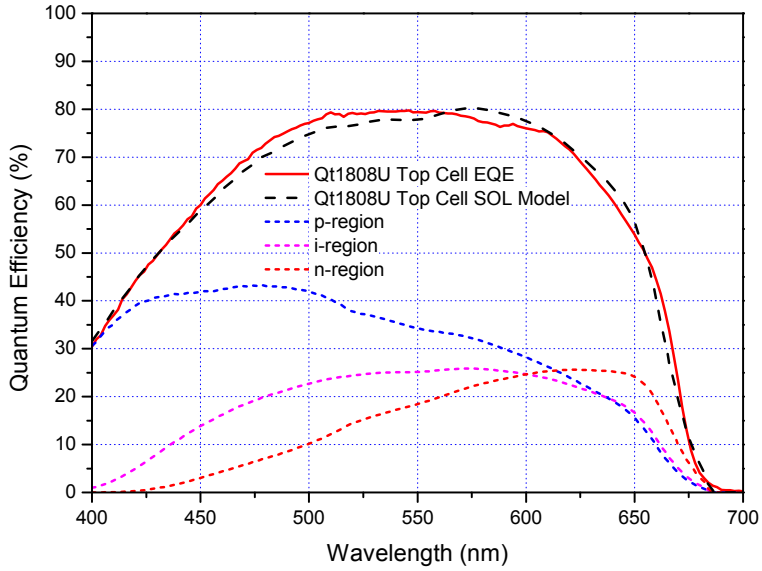


Figure 5.3: Qt1808U experimental and modelled Quantum Efficiency.

For the results to be independent of differences in AR coatings, the Internal Quantum Efficiency (IQE) was calculated using the measured reflectivities as described in Section 3.4. A short-circuit current calculation was performed using the IQE and the standard AM1.5g and AM0 spectra with the results of the calculation summarised in Table 5.3.

The calculation reveals an increase in Qt1808U top cell photocurrent density by 4.8% and 5.0% compared to preliminary devices for AM1.5g and AM0

		$J_{sc} A/m^2$	
Device		AM1.5g	AM0
Qt1808U MQW	Top Cell	126.4	151.1
	Bottom Cell	149.1	166.6
Qt1772AU MQW	Top Cel	120.3	143.5
	Bottom Cell	157.1	175.4
Qt1772AD MQW	Top Cell	121.0	143.3
	Bottom Cell	140.9	157.5
Qt1772BU Control	Top Cell	119.2	142.2
	Bottom Cell	133.1	144.5
Qt1772BD Control	Top Cell	119.3	142.2
	Bottom Cell	129.7	148.2

Table 5.3: Summary of Jsc for AM1.5g and AM0 spectra.

spectra respectively.

Utilising the above calculated values a dual-monochromatic characterisation was performed as described in Section 3.5.1. The results are presented in Tables 5.4 and 5.5. An increase in efficiency of 1.2% absolute was recorded for device Qt1808U in the case of AM1.5g. The uncertainty in determining the efficiency is estimated at 5% due to physical limitations in adjusting the intensity of the two laser sources to match the desired spectrum as explained in Section 3.5.1.

Sample	Efficiency (%)	Fill Factor (%)	Efficiency Error ± (%)
Qt1808U	23.4	85.2	5
Qt1772AU	22.2	86.8	
Qt1772AD	23.0	87.5	
Qt1772BU	23.0	85.3	
Qt1772BD	22.1	82.7	

Table 5.4: Tandem Cell Efficiencies under simulated AM1.5g spectrum.

The addition of an intrinsic region in the top cell improved the efficiency of the tandem cell. The main limiting factor for efficiency was the fact that the

Sample	Efficiency (%)	Fill Factor (%)	Efficiency Error ± (%)
Qt1808U	20.6	86.0	5
Qt1772AU	20.1	86.4	
Qt1772AD	20.2	86.9	
Qt1772BU	20.0	83.9	
Qt1772BD	19.6	82.7	

Table 5.5: Tandem Cell Efficiencies under simulated AM0 spectrum.

top cell is still current limiting the tandem as can be seen from Table 5.3. A further increase in the top cell QE was necessary to match the current produced by the top and bottom cells.

5.3 Top cell enhancement

Based on the results obtained from the initial cell Qt1808U, the key factor in extending the top cell quantum efficiency and hence the top cell photocurrent was determined to be the thickness of the intrinsic region. To explore this effect further, a series of models were created in SOL having as a basis the top cell of Qt1808U and gradually increasing the intrinsic region thickness. The three models are shown in Table 5.6 below:

Model	i-region Thickness (μm)	Predicted Current Density ($J_{sc}A/m^2$)	
		AM1.5g	AM
Qt1808U	0.10	126.4	151.1
1	0.20	134.7	166.4
2	0.27	138.3	171.0
3	0.34	141.1	174.3

Table 5.6: Top cell models with varied intrinsic region thickness compared to Qt1808U top cell IQE current density.

Using the modelled cells two new devices were grown both to test the model predictions and create a current-matched device. The first device grown at

ENE facilities, ENE1595.4 was tandem cell grown on an inactive Germanium substrate with a the top cell having an intrinsic region of 0.2μm as per Model 1. The purpose of the device was to be used as a control device as well as to be able to fully test the top cell. For the second device an MQW bottom cell, Qt1821AD, was grown at Sheffield according to the author's prescription. The MQW cell was grown on a GaAs substrate. A top cell, based on Model 3, was subsequently overgrown at ENE. The top cells were grown based on Models 1 and 3 respectively with the exact growth details shown in the Appendix B.

The experimentally measured EQE's of devices ENE1595.4 and Qt1821AD top cell are shown in Fig. 5.4 and Fig. 5.5 respectively. Both cells were fitted using SOL to an accuracy of 1%, which is within the experimental error.

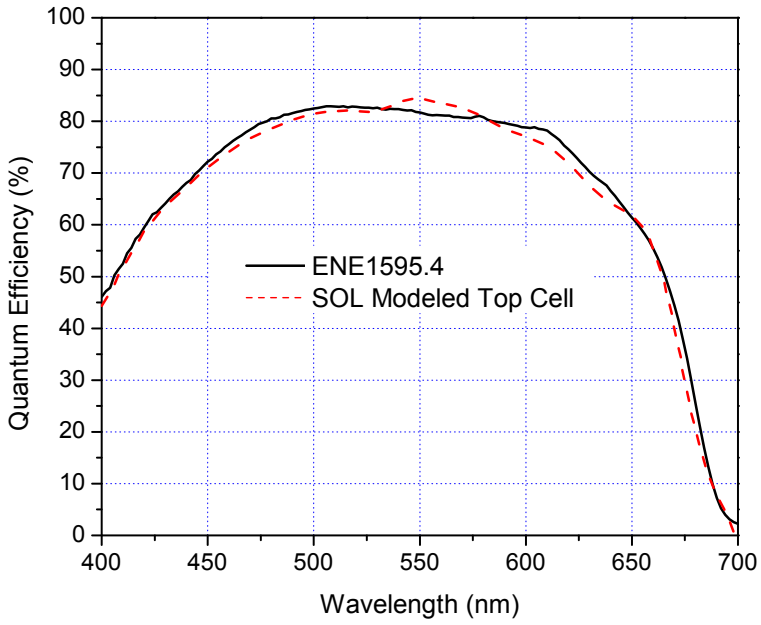


Figure 5.4: ENE1595.4 External Quantum Efficiency and corresponding modelled top cell.

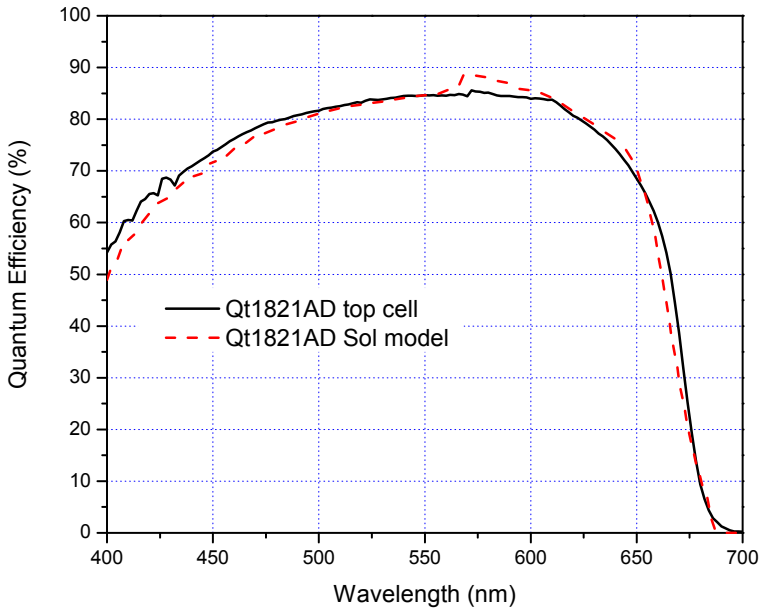


Figure 5.5: Qt1821AD External Quantum Efficiency and corresponding modelled top cell.

Comparing the calculated short current densities both samples exhibited an increase compared to sample Qt1808U as seen in Table 5.7 below.

Device	J_{sc} (A/m^2)	Increase (%)
Qt1808U	126.4	—
ENE1595.4	136.2	7.8
Qt1821AD	133.2	5.4

Table 5.7: AM1.5g top cell short circuit current density comparison.

The increase in QE in Qt1821AD is in agreement with the predictions of the SOL model. A comparison of the IQE's of the three devices is depicted in Figure 5.6. Device ENE1595.4 has been grown directly on 3° Ge substrate. It has been proven that growth at the specific angle allows a higher degree of InGaP lattice order to be achieved thus lowering the effective band gap

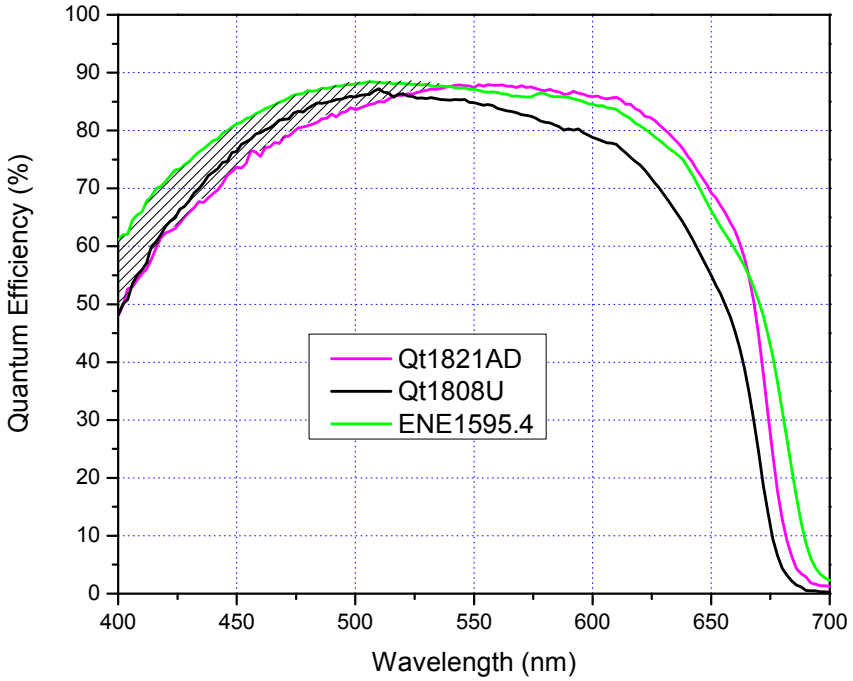


Figure 5.6: Internal Quantum Efficiency of samples Qt1821AD, ENE1595.4 and Qt1808U. Shaded region depicts decrease in QE of Qt1821AD as compared to ENE1595.4

and increasing absorption. This shift in band edge is evident in Fig. 5.6. The same applies to the window layer which appears to be optimised for deposition on Ge substrate.

Device Qt1821AD was subsequently processed into concentrator devices using the procedure described in Chapter 2. In the absence of an in-house solar simulator the devices were tested under concentration using a Xenon flash tester at ENE facilities in Belgium. A new record efficiency of 27.2% was recorded at 22x concentration. At higher concentrations the efficiency dropped and the fill factor deteriorated significantly as seen in Table 5.8. This was attributed to the high series resistance possibly due to the low emitter doping used.

Concentration (Suns)	Fill Factor (%)	Efficiency (%)
12	86.3	25.8
22	80.4	27.2
54	73.8	26.2
108	68.7	24.9

Table 5.8: Measured efficiencies for 15 finger concentrator device Qt1821AD using flash tester (AM1.5g spectrum).

5.4 Sheffield grown top cell

The results above suggest that the ability to grow high efficiency monolithic tandem cells was highly compromised by the fact that the growth was performed in two separate processes at ENE and Sheffield. Also there is evidence showing that the top cell quality depends on whether it is grown on a GaAs or Ge substrate. The Quantax 235 MOVPE reactor used for GaAs MQW cell growth at the EPSRC National Centre for III-V Technologies at Sheffield was not capable of growing high quality InGaP devices required for top cell growth thus required performing the top cell overgrowth at ENE in Belgium. In 2006 a new Thomas-Swan showerhead, multi-wafer growth reactor was commissioned which enabled the growth of both the bottom GaAs MQW cell and the top InGaP cell to be grown in a single run.
As there was no prior experience in growing InGaP devices at Sheffield the first step was to grow devices TS131-alpha, TS131-beta and TS131-Si, which consisted of an effort to reproduce the top cell present in device Qt1821AD. The top cell was grown on two GaAs and a single Si substrate to examine the effects of crystal growth on cell efficiency and bandgap. The growth details are shown in Table B.19 below.

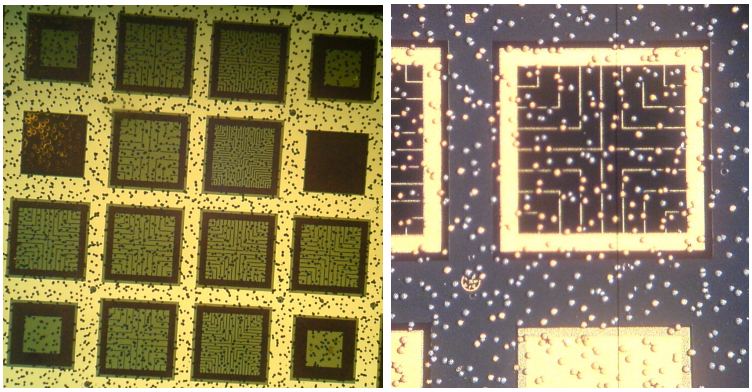
5.4.1 Top cell growth on Silicon substrate TS131-Si

All wafers were processed by the author at CIP facilities at Ipswich according to the procedure in Chapter 2. The TS131-Si wafer prior to processing

Sample	Substrate	Orientation	Band Edge EL
TS131-alpha	GaAs	10° off <111>A	655nm
TS131-beta	GaAs	3° off <110>	661nm
TS131-Si	Si	—	—

Table 5.9: TS131 Top cell samples growth details.

appeared to be hazy. It was nevertheless processed and from the measured dark currents the top cell appeared to be destroyed or non-existent. Due to this, it proved impossible to obtain a quantum efficiency measurement for the devices processed. Figure 5.7 depicts photos of the wafer taken during processing and indicate that the hazing being the InGaP top cell relaxed on the silicon substrate. Methods of growing InGaP/GaAs solar cells on silicon substrates have however been developed [2].



(a) (b)

Figure 5.7: Images of TS131-Si wafer during processing.

5.4.2 Top cell growth on GaAs substrates

Device TS131-beta was processed using the concentrator cell recipe described in Chapter 2. However device TS131-alpha was processed using a lift-off procedure with the aid of Dr. Ravin Ginige [3]. Instead of depositing directly

the front contact as described in Section 2.1, a photoresist step is carried initially and the front contact is deposited only where required. The excess material is thus 'lifted-off' when the photoresist is removed. This eliminates the front contact etching steps where precise etching was difficult to achieve. From the QE characterisation it was deduced that on sample TS131-beta the cap was not etched completely or the window layer was also etched during the process, due to the significantly lower QE as depicted in Figure 5.8. The band edge shift is also apparent in the measured quantum efficiency which is consistent with a higher degree of crystal ordering in the case of 3° off <110> GaAs substrate.

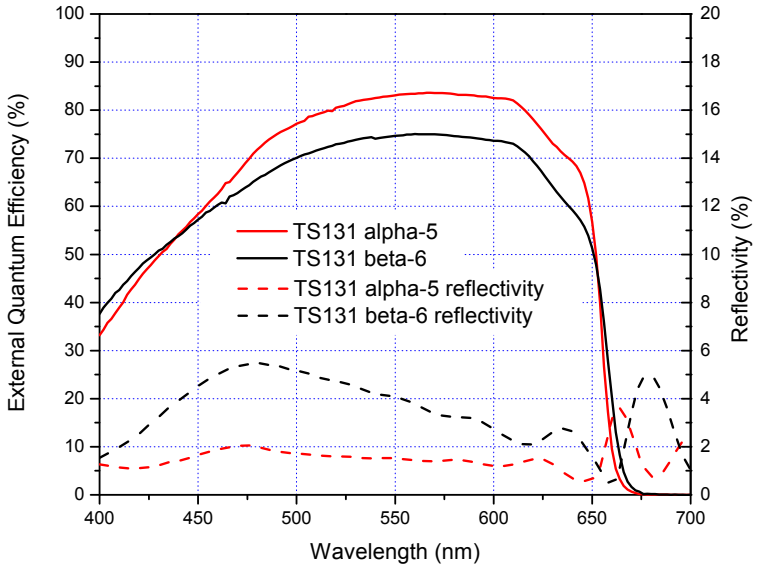


Figure 5.8: Experimental QE of devices TS131-alpha and TS131-beta.

In order to obtain a good match of the band edge in SOL, a composition of InGa(0.515)P was used and the model results are depicted in Figure 5.9 below.

Upon comparison of the top cell quantum efficiencies, as seen in Figure 5.10, it is evident that the band edge is significantly blue-shifted due to the high

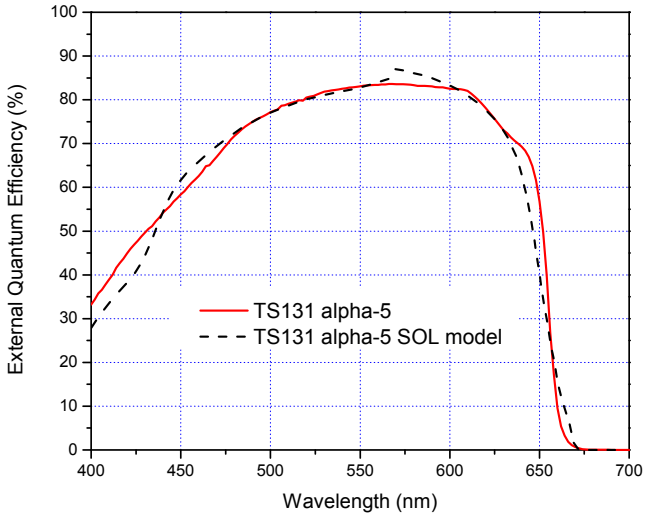


Figure 5.9: SOL model of TS131alpha-5 QE.

crystal disorder.

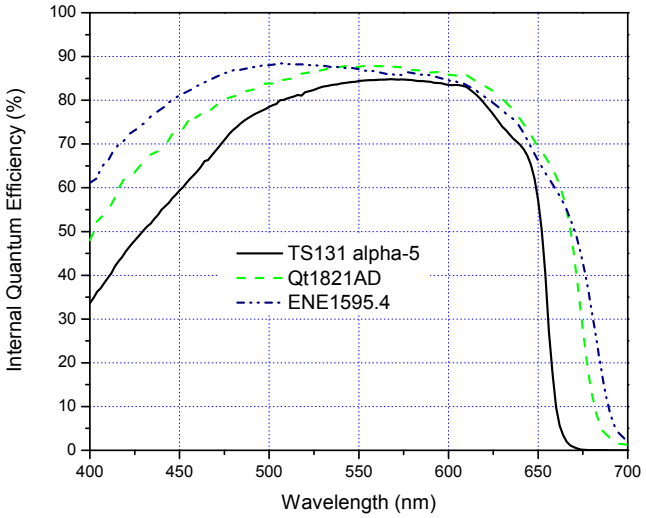


Figure 5.10: Internal QE Comparison of devices TS131alpha-5, Qt1821AD, Qt884D-6 and ENE1595.4.

5.5 Current matched devices

The highly successful top cell structure present in devices Qt1821AD and TS131 was repeated on device TS151, an SB-MQW GaAs cell specifically grown for top cell overgrowth on 3° off <110> GaAs substrate. The overgrowth was performed at ENE facilities in Belgium along with a control device, ENE1864.1, containing a commercial GaAs bottom cell on a germanium substrate.

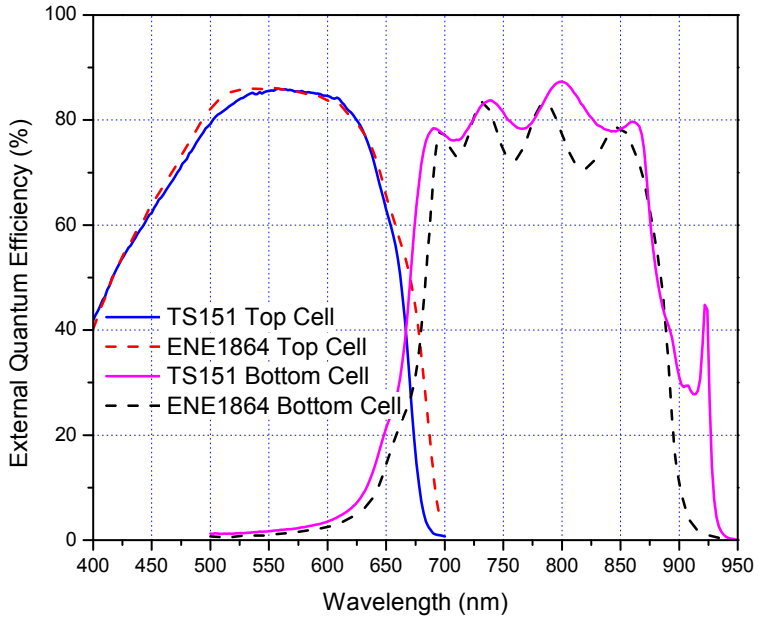


Figure 5.11: Experimental QE of devices TS151 and ENE1864.1.

As seen in Figure 5.11 the control device ENE1864.1 top cell band edge compares to the band edge seen in device ENE1595.4 which was also grown on Ge substrate. This is another indication how the InGaP top cell band edge shift depends on the substrate material and crystal orientation. Figure 5.12 demonstrates the extend of the band edge shift between the different devices where a shift of almost 30nm is observed.

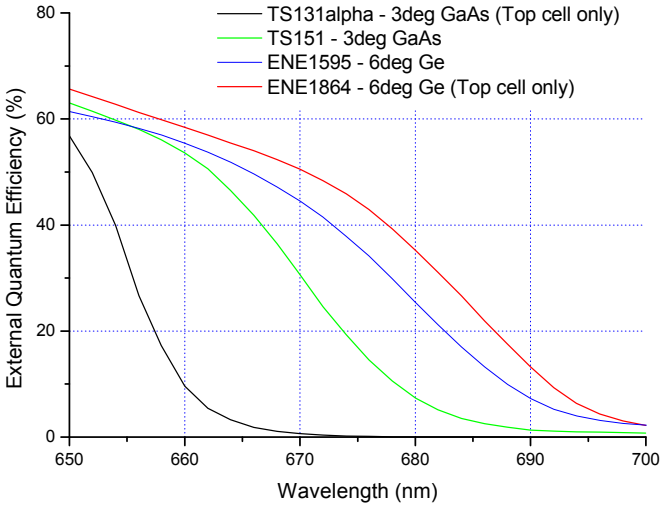


Figure 5.12: Top cell band edge dependence on substrate material and orientation.

Device TS151 exhibited a high degree of current matching similar to Qt1821AD but with a lower current output. The control device, ENE1864.1, is current limited by the GaAs bottom cell as expected for this type of tandem cell.

5.6 QE Modelling

Detailed models of the measured quantum efficiencies of the two current matched devices TS151 and Qt1821AD were performed in SOL. As can be seen in Figure 5.15 and Figure 5.14 both devices were fitted to within 3%. Particular notice was taken to accurately fit the quantum well exciton peak in order to enable accurate dark current predictions.

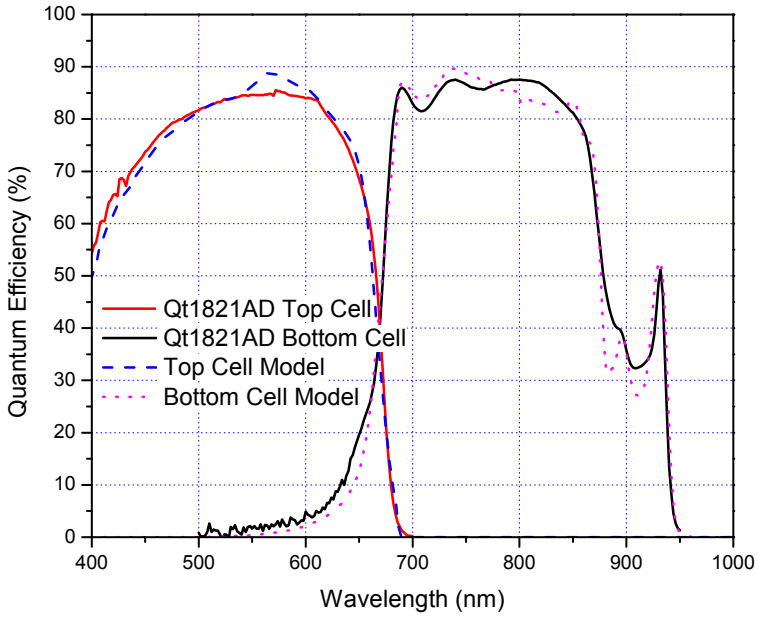


Figure 5.13: QE Modelling of TS151.

5.7 Dark Current Comparison & Modelling

Once the QE was accurately fitted, in order to fit the dark current the only two parameters adjusted were the minority carrier lifetime and the series resistance to match the high bias region. Figure 5.15 depicts the fitting of the dark current of device TS151. The model fits the data over a span of 10 orders of magnitude. A similar fit was obtained for device Qt1821AD as shown in Figure 5.16.

5.8 Efficiency Results & Modelling

Figure 5.17 depicts the measured efficiencies of the two devices under concentration. The efficiency of both devices peaked at 54x concentration due to high series resistance. The maximum efficiency recorded by TS151 was

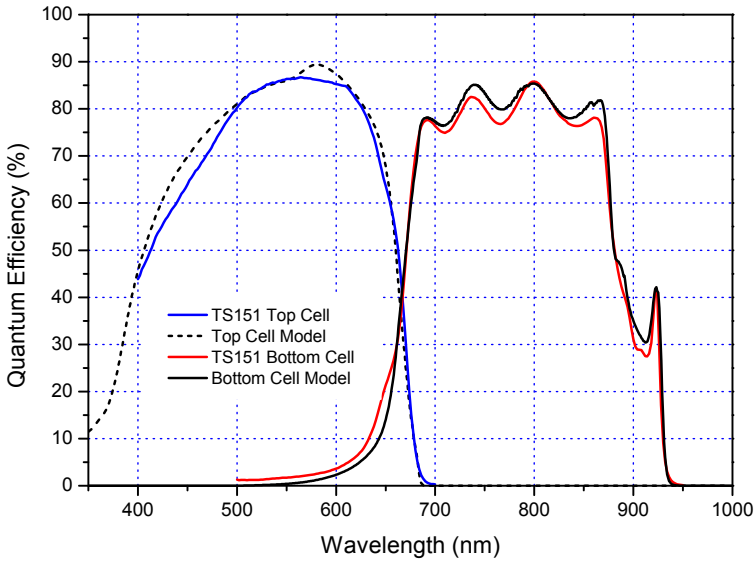


Figure 5.14: QE Modelling of Qt1821AD.

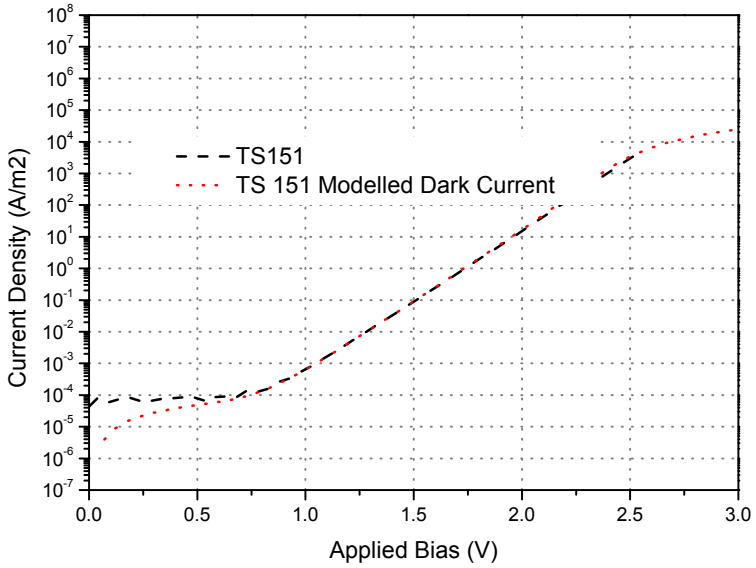


Figure 5.15: Dark Current Modelling of TS151.

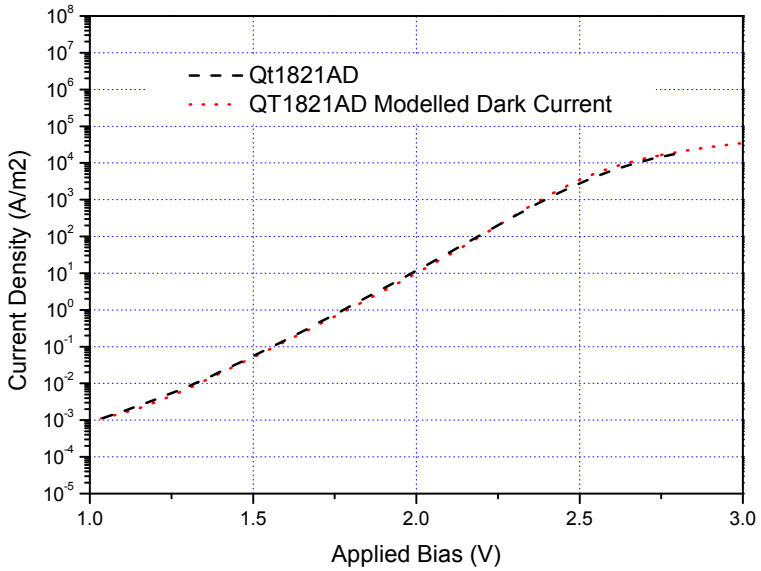


Figure 5.16: Dark Current Modelling of Qt1821AD.

30.6% which was the highest recorded efficiency at the time by an MQW solar cell.

The efficiency of number of cells for both devices were measured and differences up to 3% in absolute efficiency were recorded for TS151 and up to 5% for Qt1821AD. This appears to be consistent with concentrator cell wafer uniformity as reported in commercial wafer production [4]. Using SOL the efficiency of the devices can be modelled due to the high accuracy in dark current fitting. Figure 5.18 depicts the predicted efficiencies for the two devices. Also shown in the figure are the measured efficiencies for device Qt1821AD. A prediction on maximum possible efficiency based on the assumption of near zero series resistance. The maximum efficiency possible for Qt1821AD is 32.3%. Placing the device on an active Ge substrate which can contribute 5.2% (private communication with M. Lumb) an efficiency of 37.5% can be achieved. With two years development and the use of SOL, the company QuantaSol achieved a median wafer average of 39.7% efficiency

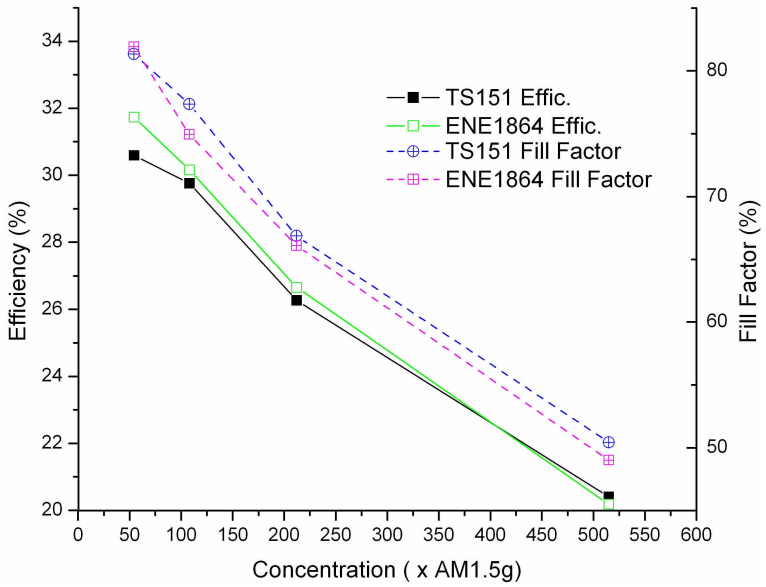


Figure 5.17: Efficiency comparison of TS151 and ENE1864.

with such triple junction cells [5]. This can be achieved if the minority carrier lifetime is increased from improved material quality. Growing the both junctions in a single reactor run will improve the material quality. The QE can become flatter and additional improvement to the anti-reflection coating will enhance the efficiency. The number of wells can be increased up to 100 [4] to achieve maximum efficiency.

5.9 Conclusions

The milestone efficiency of 30.6% has been achieved with a monolithic tandem solar cell containing strain balanced quantum well sub-cells. The power of SOL to accurately fit the quantum efficiency and to make predictions of real dark current data has been presented. Realistic efficiency predictions can be performed based on the confidence provided by the model. The MQW bottom cell was no longer the limiting current junction in the tandem cell.

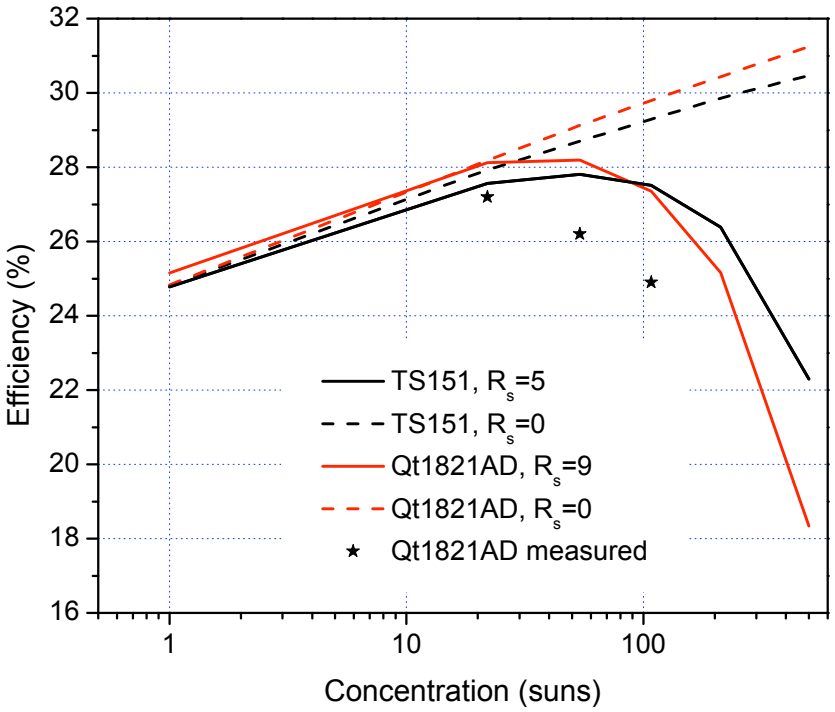


Figure 5.18: Efficiency prediction from SOL Modelling.

The top cell efficiency is greatly impacted by the underlying substrate and the growth orientation. Further study is required for the top cell growth in order to maximise the gains provided by the MQW bottom cell. A step towards that direction could be the incorporation of MWQ structures in the top cell. In this manner the band gap of both junctions can be fine tuned without being affected or limited by the underlying substrate.

Bibliography

[1] T. N. D. Tibbits, *Optimisation of strain-balanced quantum well solar cells for concentrator and multijunction (tandem) structures*. PhD thesis, Imperial College of Science, May 2006.

[2] M. G. Mauk, A. N. Tata, and B. W. Feyock, "Selectively-grown InGaP/GaAs on silicon heterostructures for application to photovoltaic–photoelectrolysis cells," *Journal of Crystal Growth*, vol. 225, no. 2-4, pp. 359–365, 2001.

[3] R. Williams, *Modern GaAs processing methods*. Boston: Artech House, 2nd ed., 1990.

[4] B. Browne, J. Lacey, T. N. D. Tibbits, G. Bacchin, T.-C. Wu, J. Q. Liu, X. Chen, V. Rees, J. Tsai, and J.-G. Werthen, "Triple-junction quantum-well solar cells in commercial production," in *AIP Conference Proceedings*, vol. 1556, pp. 3–5, 2013.

[5] K. W. J. Barnham, A. Dobbin, M. Lumb, and T. N. D. Tibbits, "Tuning the triple junction," *Coumpound Semiconductor Magazine*, vol. 17, pp. 32–35, March 2011.

Chapter 6

Concentrator Optics Design

GaAs based solar cells are expensive. Combining them with low cost light concentrating systems can reduce their electricity cost considerably. Chapter 5 demonstrated the advantages of tandem solar cells whose power conversion efficiency increases with concentration. A concentrator system consists of one or more optical components that concentrate direct and or diffuse light onto the solar cell. These optical components can either be imaging or non imaging optics or a combination of the two. High concentrations of 500x are needed as multi-junction cells are very expensive. Silicon based flat plate panel low prices are currently driving Concentrator PV (CPV) to higher concentrations of up to 1000x and there are concentrator systems based on III-V tandem solar cells that are market ready [1].

6.1 Concentrator System Overview

Concentrator systems are currently used exclusively for the purpose of large PV plants in regions of high direct normal insolation (DNI) as their system costs are high. An updated list of large concentrator PV systems is published by CPV Consotrium [2]. A novel approach, which was proposed by Dr. Massimo Mazzer, for the use of concentrators is examined in this thesis.

The approach involves use of concentrator systems in building integrated photovoltaics (BIPV).

The idea focuses on integrating concentrator systems in double glazing windows that are used in all-glass building facades. This implementation reduces the unwanted direct sunlight while allowing diffuse through for internal illumination with the building cooling demands also being reduced. The multi-functional benefits of lower air-conditioning and lighting demand and potentially use of cooling water changes the economics from simply undercutting silicon flat panels. However, this imposes a constraint on the back focal length (BFL) of the concentrator lens; the BFL must be in the range of 45 to 50mm. The concentration level is required to be at 1000x suns. This translates into having a lens optical aperture of $1000mm^2$ based on the standard $1mm^2$ concentrator cell design. The tracking system is assumed to have an accuracy of at least 0.5° therefore the lens focusing tolerances need to be set accordingly.

In order to achieve a commercially viable system the system cost should be kept to a minimum. Thus the lens utilised by the system should be inexpensive and easily manufactured. In order to achieve this glass lens designs are not considered but instead a plastic lens design is preferred. Typical plastic lenses are made up of polymethyl methacrylate (PMMA) and these are easily manufactured using an injection moulding process. This type of lenses have been proposed for solar concentrator applications for their long lifetime under sunlight and for begin transparent for the most of the solar spectrum [3][4].

A variant of this system would be a sun-tracking lens focusing on a stationary waveguide, which in turn would transmit the light to the solar cell. This system allows more flexibility in the position of the solar cell in the system structure allowing to remove the cell from the line of sight and into the frame. Furthermore the waveguide ensures there is more uniform light distribution on the solar cell. A concept system is depicted in Figure 6.1.

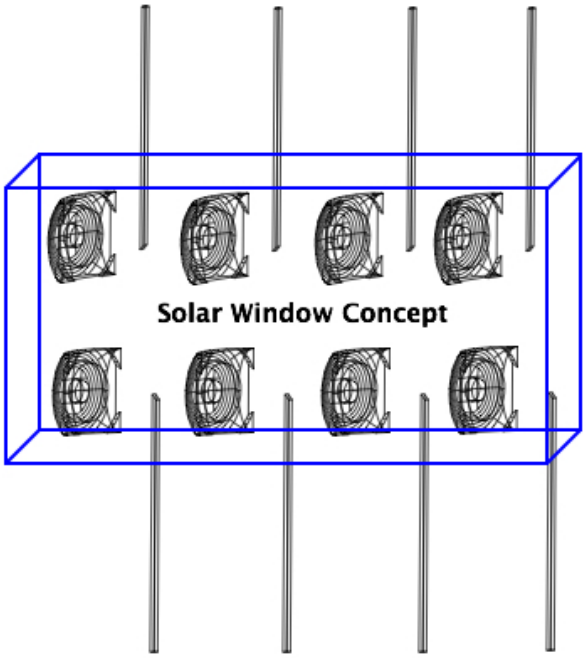


Figure 6.1: Solar window concentrator system concept.

6.2 Preliminary Designs

The most commonly used lens type in low-cost high-concentrator systems is the Fresnel lens. The Fresnel lens was developed by Augustine Fresnel and it exploits the idea that the front curved surface of a plano-convex lens is necessary in order to bend the light rays to a focus. The Fresnel lens imitates the curvature of the curved surface using triangular facets on the front surface of the lens thus reducing a semi-spherical lens to the well know flat fresnel lens. This idea however was originally formulated by Georges de Buffon in 1748 whilst studying methods to reduce cost and weight of lighthouse lenses [5]. The original idea by Buffon was to reduce the material used by removing excess material in disc sized forms from the rear side of the lens.
The Buffon lens design was proposed by Barry Clive of Optical Products Ltd

as an alternative design due to the lower manufacturing cost using PMMA plastic and the simplicity of the design compared to the Fresnel lens approach. The lens would be designed and optimised with ZEMAX, an optical design and analysis software. ZEMAX is a ray tracing software considered the industry standard for optical design and analysis [6]. It has the ability to handle complex optical systems and diffractive optics. Based on the requirements of the application which determined the size of the lens and the focal length, a convex lens was designed that satisfied these conditions. This lens was used as a 'blank' for the development of the Buffon lens. The radius of curvature and thickness of the lens were optimised depending on the design to obtain the highest transmission of sunlight.

6.2.1 ZEMAX light source and detector parameters

The design of a square lens with features of rotational symmetry proved to be a daunting task in ZEMAX. The design had to be squared to ensure all direct sunlight is focused on the square cells. To overcome this difficulty rotationally symmetrical lenses were designed and tested with a square collimated source in order to simulate a square lens. ZEMAX allows polychromatic sources to be entered using up to eleven wavelengths with weighted inputs. Figure 6.2 depicts the modified AM1.5g spectrum as used in the simulations. The light distribution is based on random ray placement on the source. The number of rays used is user defined and in this case 10,000 rays were used. The number of rays used was decided empirically after assessing output accuracy on repeated runs and reasonable processing time. The optical efficiency is defined as the percentage of rays reaching a detector.
The output efficiency of the lens was measured using a virtual 1mm x 1mm CCD detector with 100 x 100 pixels. The detector provided the output image efficiency as well as the light distribution on the detector. To obtain light distributions and output efficiency for a specific wavelength the source required to be changed to monochromatic as the detector only measures

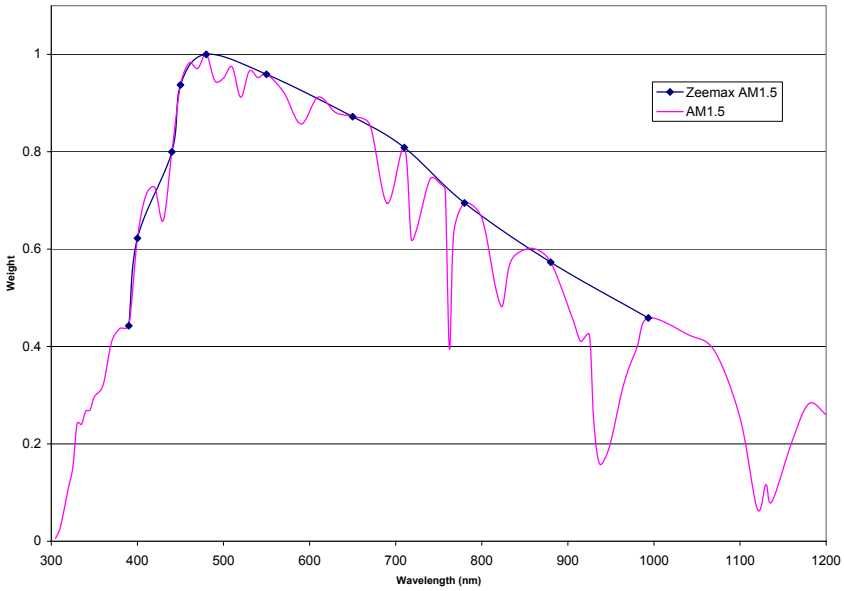


Figure 6.2: Modified AM1.5g Spectrum as used in ZEMAX.

intensity regardless of wavelength.

6.2.2 Buffon Concentrator Lens

In order to facilitate the design of the lens a set of nomenclature was created. The disc-shaped cut-outs of the Buffon lens would be referred to as 'steps' and they would be numbered in increasing order starting from the one closest to the curved surface of the lens. The two main design types were split into even step size and uneven step size designs. Even step size designs have steps whose width is the same for all the steps and the step radius increases linearly with step number. In uneven step designs both the width and the diameter of the steps are varied so that the lens material is the minimum possible whilst maintaining the structural integrity of the lens.
During the lens development stage a wide range of preliminary designs was

modelled. Four of these designs are presented as they cover the whole range of designs explored. These designs model the variation of optical efficiency with respect to step size and number of steps.
The following equations were used to determine to determine the step sizes in even steps designs:

$$W = \frac{t}{N+1} \tag{6.1}$$

where w is the step width, t is the lens thickness and N the number of desired steps.

$$R_n = n \times \frac{D}{2(N+1)} \tag{6.2}$$

where R_n is the n^{th} step radius, n is the step number and D is the lens diameter.
Table 6.1 below presents a summary of the four preliminary designs. The number of steps in the uneven step design was chosen from the equivalent step number even design, since this exhibited the highest efficiency. The uneven design improves greatly the structural stability of the lens and also the light distribution is more even without significant performance loss.

Lens	**Back Focal Length (mm)**	**Lens thickness (mm)**	**Total Track Length (mm)**	**Efficiency (%)**
4 even	46.9	13	59.9	86.6
14 even	46.9	13	59.9	87.9
42 even	49.1	9.8	58.9	87.8
14 uneven	45.5	13	58.5	87.7

Table 6.1: Summary of preliminary concentrator Buffon lens designs.

Figure 6.3 shows the preliminary lens designs and Figure 6.4 their modelled output intensities. As seen from Table 6.1 the increase in efficiency in more complex designs does not justify the increase in manufacturing complexity required to make the lenses. Also, as can be seen in Figure 6.4(a) which

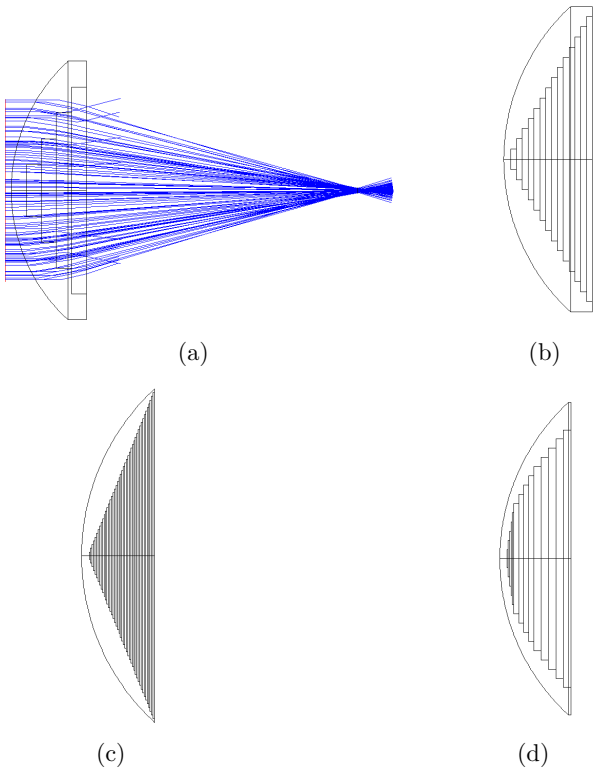


Figure 6.3: Preliminary concentrator lens designs. (a) Four even step design (b) Fourteen even step design (c) Forty-two even step design (d) Fourteen uneven step design

shows typical ray tracing by ZEMAX, the majority of losses comes from total internal reflections on the sides of the steps. The other major sources of losses are spherical aberrations. Spherical aberrations tend to increase with increasing radius of curvature and lens thickness.

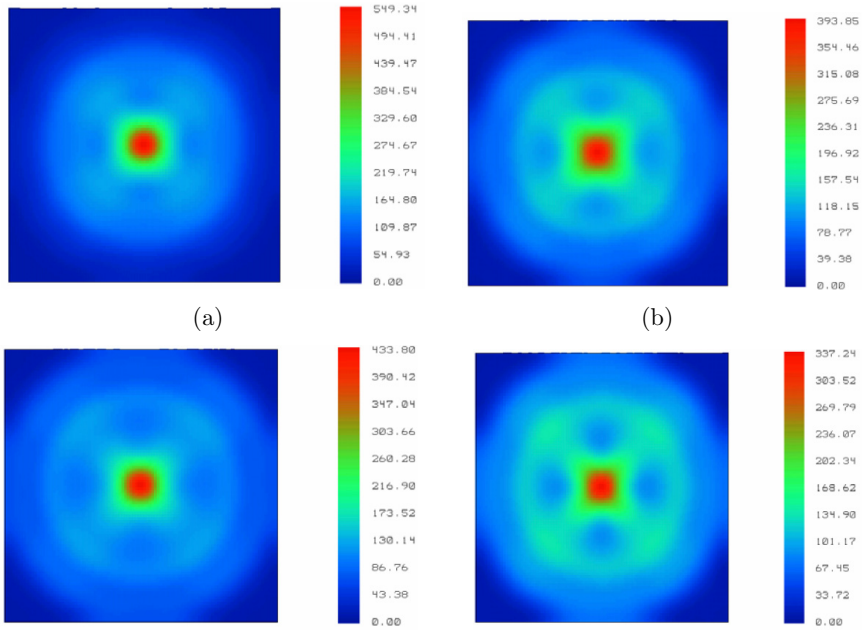


Figure 6.4: Output images for (a) four even step, (b) fourteen even step, (c) forty-two even step and (d) fourteen uneven step designs.

6.3 Optimised Buffon Lens

6.3.1 Optimised 'Blank' Lens

The first stage of optimisation involved optimising the plano-convex lens, which would be used as a 'blank' for the optimised Buffon lens. The front surface of the lens was optimised using ZEMAX's Optimisation function. This is a powerful function that allows lens parameters to be set as variables and optimised according to a merit function. In this case, the conic constant of the front surface was set as variable and the merit function was the minimum RMS Spot radius. The only constraint in the optimisation procedure

was that the total track of the system would be 50mm.

6.3.2 Step Side Angle Optimisation and Tolerances

The greatest efficiency drop was determined to originate from total internal reflection occurring at the sides of the Buffon step features. In order to compensate this the step sides were set parallel to the calculated angle of the rays traversing the lens at each corresponding side. The side angle of each step was altered individually in order to estimate the efficiency increase contribution from each alteration. Table 6.2 below summarises the obtained results.

Step No.	**Optimal step angle**	**Efficiency contribution**
1	3.3°	0.6%
2	10.3°	4.1%
3	14.4°	1.3%

Table 6.2: Efficiency contribution when having the step side at angle.

The total lens efficiency increases by 6% with the above configuration. The major contributor in the efficiency increase is the second step side angle. The first step angle is difficult to achieve if a manufacturing precision of ±0.1mm is assumed and it was therefore discarded as a feasible feature. It was however used in the following modelling in order to obtain the maximum achievable efficiency.

As the side angle of step No.2 has the most effect on efficiency the effect of angle tolerance on efficiency was examined.The side angle was varied by altering the outer step radius in 0.1mm steps. An increase of the outer radius translates into a shallower angle and similarly a decrease translates into a steeper side angle. The results are summarised in Table 6.3 below.

The above results show that if the manufacturing precision for the outer edge radius is within 2% the output efficiency will be affected less than 1%. The efficiency change is less than 0.1% for the ±1% range for radius precision.

Outer edge radius change (mm)	**% diff. in outer edge radius**	**Edge angle**	**% diff. of edge angle**	**Efficiency Change**
-0.3	-3%	15.3°	+48.0%	-1.5%
-0.2	-2%	13.6°	+32.2%	-1.0%
-0.1	-1%	12.0°	+16.2%	0%
0.1	1%	8.6°	-16.4%	0%
0.3	3%	6.9°	-32.9%	-0.6%
0.4	4%	5.2°	-49.6%	-1.3%

Table 6.3: Efficiency change with No. 2 step side angle change.

6.3.3 Cell Position Effects

The output efficiency of the lens was examined as a function of distance from the optimum image position in order to examine the tolerance of the system as far as image positioning. The output efficiency was measured on the $1mm^2$ CCD detector positioned on the imaging plane. The zero displacement is set at the point of maximum efficiency, which occurs 44.17mm behind the lens. As can be seen from the graph the efficiency is above 90% in the range of -0.4 to +0.6mm which corresponds to a tolerance of approximately 1% in image position determination.
As the image positioning tolerance is the predominant factor in the system efficiency other types of possible misalignments were not examined.

6.3.4 Lens Dimensions Tolerances

The optimised Buffon lens exhibits an ideal output efficiency of 93.3%. In a real world situation of mass produced lenses the objective is to maintain an output efficiency of above 90%. In order to achieve this the manufacturing tolerances need to be determined. Each dimension of the lens, the radius of curvature (r.o.c.), the conic constant and lens thickness, was varied from the ideal value and the efficiency change was noted.
In the case of the radius of curvature changes of the order of $\pm 2\%$ resulted

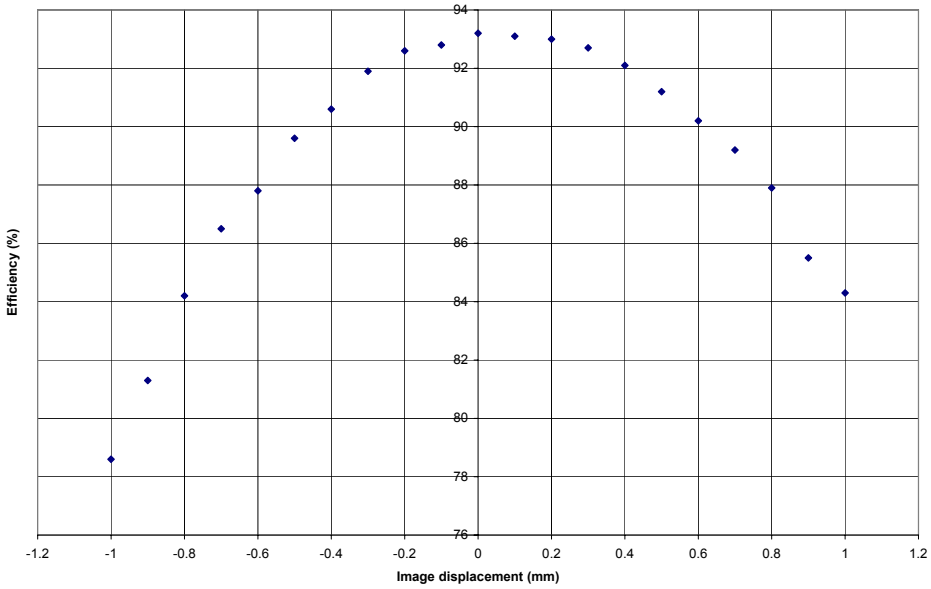


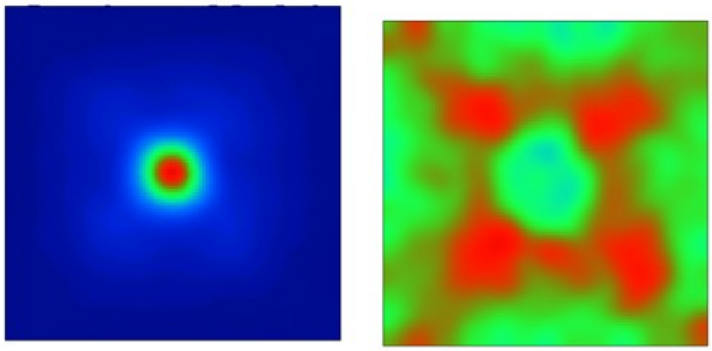
Figure 6.5: Effect of image position on output efficiency

in an efficiency drop from 93.3% to 79%. Changes of ±1% in the radius of curvature were assumed to be the highest tolerated error as in this case the efficiency decreases from 93.3% to 89.4%. On the other hand the conic constant plays little part in changes in efficiency. Even at large changes of +10% and the efficiency only dropped to 88.3%. The efficiency remains above 90% for up to ±9% change in the conic constant.

The lens thickness tolerance demonstrated the most prominent effect on output efficiency. A small change of the order of +0.2% (0.02mm) in thickness resulted to an efficiency of 86.5% i.e. a decrease of 6.8% in absolute efficiency. This result will be of great importance because it sets a precision limit to the manufacture of the lens thickness if the output efficiency is to be maintained above 90%. Negative changes in the lens thickness were not possible as the side lengths of the lens diminish with reduced thickness.

6.3.5 Light Distribution

The Buffon lens is not a typical imaging lens but as it can been seen in Figure 6.4 the light distribution at the focal point is more typical of an imaging optic. For concentrator cells the more uniform light distribution provided by non imaging optics is preferred in order to better utilise the whole of the cell active area effectively. With the addition of 15mm waveguide between concentrating lens and solar cell a uniform distribution can be achieved as seen in Figure 6.6 below. The uniformity of the light distribution can be further increased with increasing waveguide length.



(a) (b)

Figure 6.6: Output images (a) with lens alone and (b) with 15mm waveguide.

6.4 Waveguide Design

The waveguide design used consisted of a 2mm square cross-section waveguide with a mirrored, slanted face at one end and of total length of 10mm. Figure 6.7 below depicts the ZEMAX model setup.
The optimum angle for the slanted face was calculated using edge ray analysis and assuming total internal reflection (TIR) at the slanted edge interface.

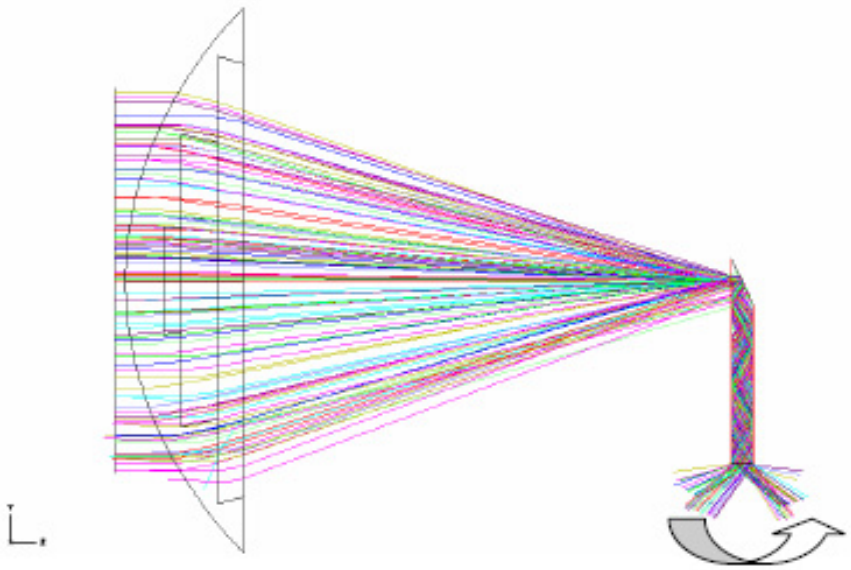


Figure 6.7: Waveguide ZEMAX model setup.

The range of angles of incidence considered was -22° to 82°. This range results from assuming a 44° converging beam from the lens and the waveguide pivoted by a maximum of 60°. The 60° maximum pivot angle was used assuming a system to be located at a latitude of 50° i.e London and therefore this is the maximum solar altitude angle. This calculation resulted in an optimum angle of 28.1° for the slanted face. During the modelling process a different optimum angle was found in ZEMAX using a mirrored slanted face at 32°. The reasons behind this change are described below. Results were modelled for both angles.

6.4.1 Waveguide Modelling

For the modelling the waveguide was used in conjunction with the optimised concentrator presented in §6.3. The purpose of the modelling was to optimise the waveguide shape and position using a sun tracking Buffon lens. The

Slanted face angle:	28.1°	32.0°
Degrees	**Output (%)**	
0	67.12	84.71
15	85.23	85.81
30	85.68	85.46
45	83.3	79.54
60	71.71	63.81

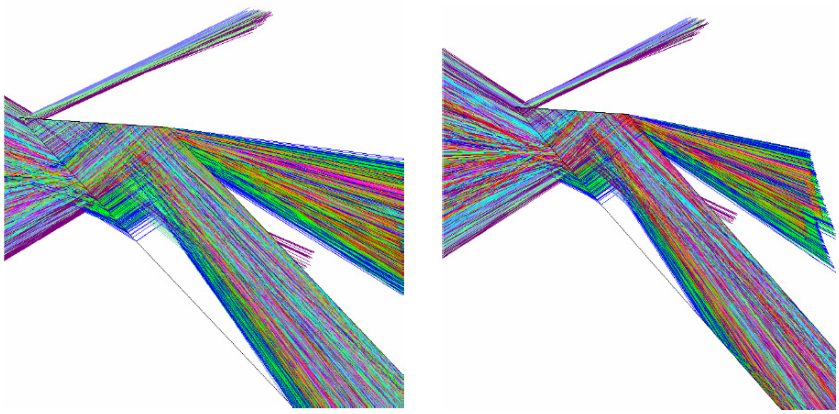
Table 6.4: Concentrator output efficiencies for PMMA waveguide.

waveguide was rotated during the modelling to mimic the effect of a tracking lens. The waveguide was placed at the circle of least confusion of the lens focus. The circle of least confusion is the smallest optical spot produced by the lens. Each ray trace routine used 10,000 rays and the simulation was the same as described in §6.3 for the optimised concentrator lens.

A series of ray traces were performed for different rotation angles of the waveguide. The rotation pivot was set on the front face of the waveguide with a distance from the edge equal to half the length of the slanted face. An anti-reflection coating was applied to the sides and bottom face of the waveguide. The slanted face was coated with a 95% mirror and the waveguide material used was PMMA. The virtual detector was placed on the bottom face of the waveguide and an air interface between the detector and waveguide was assumed. Table 6.4 below summarises the results for the two slant face angles. The light output of the lens, which is (94.24±0.01%), was used as the light input for the waveguide. All the efficiency outputs recorded refer to the total system efficiency.

Having the slanted face angle at 32° shows an improvement in efficiency at the 0° rotation angle of the order of 17%. On the other hand the 28.1° slanted face waveguide shows higher efficiency in the 45° to 60° rotation range.

In an attempt to increase the collection efficiency at 60° the waveguide was displaced by -0.1mm on the y-axis. The y-axis displacement refers to vertical displacement of the waveguide from the lens axis with the center of the



(a) (b)

Figure 6.8: Ray tracing diagrams of waveguide with vertical displacements of (a) 0.0mm and (b)-0.1mm at 60° rotation.

slanted face as the reference point. The effect of the displacement of the waveguide is to decrease the losses through the back of the waveguide as can be seen in Figure 6.8. There is a minor increase of rays missing the entrance of the waveguide but overall the efficiency is increased. These results are summarised in Table 6.5 below. The output efficiency is increased by 4% for both slant face angles at 60° rotation with the -0.1mm waveguide displacement.

Slanted face angle:	**28.1°**	**32.0°**
Degrees	**Output (%)**	
0	66.4	84.7
15	85.26	85.8
30	85.73	85.69
45	84.42	81.32
60	75.43	67.18

Table 6.5: Concentrator output efficiencies for PMMA waveguide with -0.1mm displacement.

The efficiency output for the 28.1° slanted face is not consistent through out and exhibits large losses at 0° rotation. This is due to TIR on the bottom surface of the waveguide where the rays exit due to the glass-air interface. These losses can be seen in Figure 6.9.

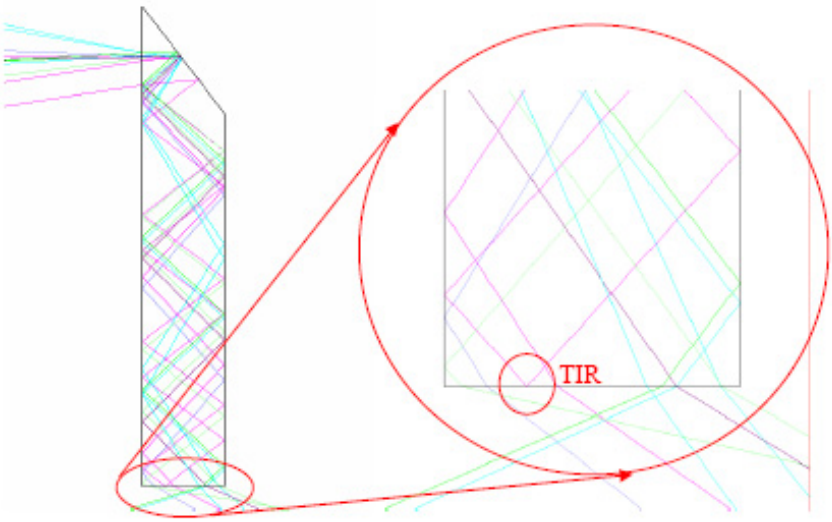


Figure 6.9: Total internal reflection losses at exit side of waveguide.

To investigate these losses further the simulations were repeated with the virtual detector placed slightly inside the waveguide to ensure optical coupling and to avoid TIR effects on the efficiency. Table 6.6 below shows a dramatic increase of 20% at 0° rotation for the 28.1° slant face angle. These results match the prediction for the optimum angle as they prove that the calculated 28.1° slant face angle is indeed the optimum.
The output efficiencies of the system were also modelled with an F2 glass waveguide. The F2 glass is a 'flint' type glass with a refractive index ranging from 1.61 to 1.63 in the visible spectrum [7]. The positioning of the waveguide was not altered. The slant face angle was changed to 26°, which was determined by the same edge ray analysis as before using this time the

refractive index of F2 glass.

Slanted face angle:	**28.1°**	**32.0°**
Degrees	**Output (%)**	
0	87.96	82.68
15	87.68	87.69
30	87.57	87.55
45	85.82	83.08
60	75.08	68.75

Table 6.6: Concentrator output efficiencies with PMMA waveguide with -0.1mm displacement and detector inside the waveguide

Slanted face angle:	**26.0°**	
Detector Position	**Outside**	**Inside**
Degrees	**Output (%)**	
0	38.32	88.00
15	72.8	87.64
30	85.66	87.44
45	85.2	86.72
60	78.06	79.45

Table 6.7: Concentrator system efficiencies with F2 glass waveguide.

The results, as shown in Table 6.7, show an increase in efficiency of 4.5% using the F2 glass waveguide with the detector inside the waveguide compared to the equivalent PMMA waveguide output. The only concern is the fact the TIR losses increase dramatically in the case of F2 glass waveguide. This has to be taken into account because the waveguide to solar cell coupling will be of greater significance in the case of F2 glass waveguide.

The final set of simulations for the waveguide was performed to determine the degree of attenuation for different waveguide lengths. The lengths chosen correspond to actual waveguide lengths to be used in the final concentrator design. The results are depicted in Table 6.8 below.

Slanted face angle:	26.0°		
Detector Position:	Inside		
Waveguide Length (mm)	52	104	156
Degrees	**Output (%)**		
0	86.82	85.27	83.69
15	86.57	85.2	83.83
30	86.41	85.21	83.9
45	85.85	84.61	83.39
60	78.47	77.43	76.52

Table 6.8: Concentrator system output efficiencies for various lengths of F2 glass waveguide.

The attenuation is approximately 1.5% per 50mm waveguide length which is adequate for the concentrator design.

6.4.2 Experimental Results

According to ZEMAX modelling the F2 glass waveguides were the best candidates for the concentrator design. To verify the waveguide modelled efficiencies a similar setup was constructed in the lab to characterise a 52mm, F2 glass waveguide. The waveguide characterisation was performed using a collimated beam of 1.8mm in diameter from a Bentham monochromator as seen in Figure 6.10 below. Using a pre-characterised silicon cell a reference scan was performed prior to attaching the cell using an index matching fluid to the waveguide. The scan was repeated for several waveguide angles. Figure 6.11 below depicts the recorded output efficiencies of the waveguide.
The experimental output efficiencies are lower than the modelled values. The interesting trend that appears though is that at 15° and 30° rotation angles the output efficiency is similar and much higher than 0° and 60° rotation angles. This trend is similar to ZEMAX results for F2 glass waveguide with the detector situated outside the waveguide as shown in Table 6.7. These losses were visible during the experiment at the cell-waveguide interface. This was

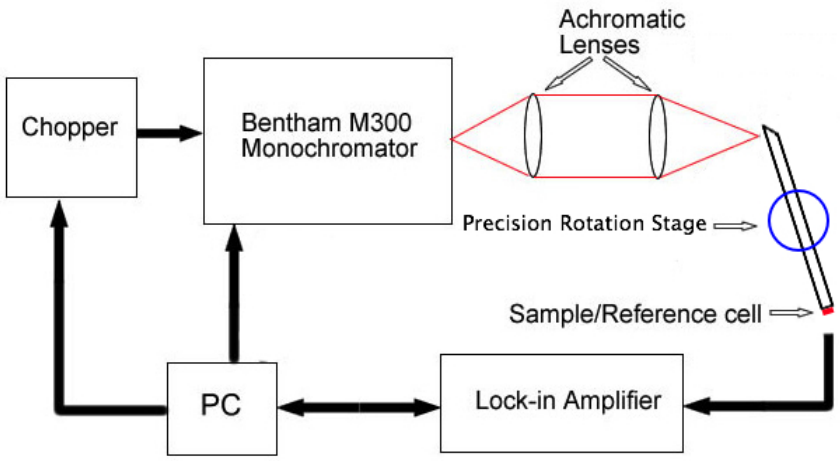


Figure 6.10: Experimental setup for F2 glass waveguide characterisation.

deemed as the major source of error and the reason behind the large discrepancy between model and experiment. The index-matching fluid did not provide a 'clean' coupling as bubbles forming on the sides of the waveguide near the interface allowed light to escape before reaching the detector. Another source of losses was due to the nature of the setup available, as it was also not possible to accurately position the waveguide to the optimum position with respect to the collimated beam. The results do exhibit though the efficiency trends as described by the modelling. With adequate cell-to-waveguide coupling and good waveguide positioning it should be possible to reproduce the modelled efficiencies to a higher accuracy.

6.5 Conclusions

The Buffon lens design is dependable alternative solution as a concentrator lens instead of convex or Fresnel lenses. The lens combines the characteristics of an ordinary convex lens along with the reduced material as in the case of the Fresnel lens. It offers a simpler manufacturing solution compared to the

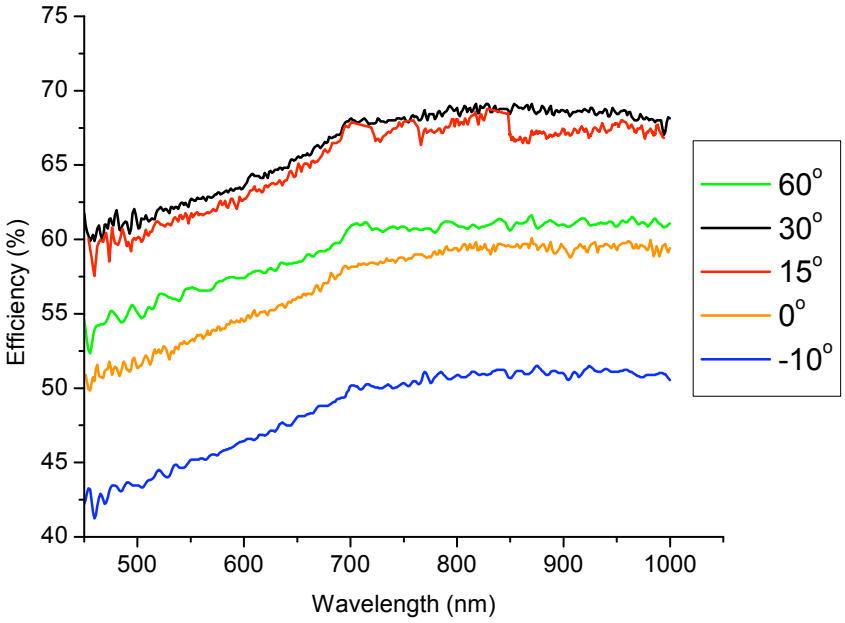


Figure 6.11: Experimental output efficiencies for a 52mm, F2 glass waveguide.

Fresnel lens and with the ability to use material such as PMMA the cost of such concentrating optics drops significantly. The design has however a few limitations; there is a need for high accuracy in manufacturing and system integration in order to achieve the theoretical output efficiencies.
Independently of the lens design the addition of the waveguide in the system design provides a number of benefits. The waveguide is a requirement in cases were uniform cell illumination is necessary. In addition to that, more flexibility in the system design is possible as the solar cell can be deployed in positions other than the concentrator lens focal point. The addition of the waveguide does not, however, alleviate the need for accurate placement at the lens focal point. Further investigation can be performed in waveguide design for example tapered waveguides, that can also be used to lift positioning

constrains and further enhance concentration.
Overall the system design as proposed is an ideal candidate for Building-Integrated PV (BIPV). The flexibility in design allows for a wide range of applications. The predominant usage is in the form of active glass facades that can be both aesthetically pleasing as well as contributing to the building's energy needs. Self-sustained buildings can lead the way to a renewable future.

Bibliography

[1] A. W. Bett, G. Siefer, C. Baur, S. Van Riesen, G. Peharz, H. Lechenmuller, and F. Dimroth, "Flatcon concentrator pv-technology ready for the market," in *20th European Photovoltaic Solar Energy Conference*, (Barcelona, Spain), 2005.

[2] CPV Consortium, "CPV Project Library." http://cpvconsortium.org/projects, 2015.

[3] L. G. Rainhart and W. P. Schimmel, "Effect of outdoor aging on acrylic sheet," *Solar Energy*, vol. 17, pp. 259–264, 1975.

[4] R. Leutz, A. Suzuki, A. Akisawa, and T. Kashiwaki, "Design of a nonimaging fresnel lens for solar concentrators," *Solar Energy*, vol. 65, no. 6, pp. 379–387, 1999.

[5] R. Leutz and A. Suzuki, *Nonimaging Fresnel Lenses*. Springer-Verlag Berlin Heidelberg, 2001.

[6] R. Fischer, *Optical System Design*. Mcgraw-hill, 2nd ed., 2008.

[7] Schott AG, *Schott Optical Glass Catalogue*. Schott AG, 2007.

Chapter 7

Conclusions

The most important achievement of this thesis is the milestone efficiency of 30.6% under 54x concentration achieved by a monolithic tandem solar cell containing strain balanced quantum well sub-cells. This was the first solar cell with quantum wells to exceed 30% efficiency. This thesis also reports the first demonstration of tandem cells containing quantum well sub-cells. The first characterisation and modelling of the quantum efficiency and dark current of such devices was demonstrated.

An efficiency of 32.3% at 500x concentration is predicted if low series resistance is assumed using the simulation software SOL. This is a promising result as it will correspond to 37.5% efficiency in a triple junction cell using an active Ge substrate. With the use of SOL and improvement of the carrier lifetimes, series resistance and reflectivity over 40% efficiency if possible as demonstrated by the company QuantaSol.

The main tool for modelling quantum efficiencies and predicting dark currents was presented in Chapter 4. By fitting the QE in the bulk region the crucial parameters D, the minority carrier diffusion coefficient, L, the minority carrier diffusion length and S, the surface recombination velocity, could be determined. It has been proven that using these parameters the ideal Shockley injection current could also be determined. The radiative current

is determined by fitting the quantum well QE. Thus the dark current at high bias, where ideality $n = 1$ dominates, is determined. To determine the dark current for the low bias region where ideality $n \approx 2$ dominates, a fit was performed using a single parameter, the carrier non-radiative recombination lifetime, the dark current can be fitted over many orders of magnitude.
SOL's ability to accurately predict the dark current of multi-junction devices can be used to design optimum cell combinations. It has been proven that efficiency enhancement is possible using MWQ devices. MQW devices do not have the typical constraint that monolithic tandems have of lattice matching. It is the tool for exploring further the realm of band gap engineering for multi-junction solar cells. MQW structures can be inserted in all junctions and thus achieve the maximum possible conversion efficiency.
In Chapter 6 a new optical concept was investigated for a building integrated PV design using the high efficiency multi-junction solar devices developed in this thesis. A Buffon lens design was developed and modelled as an alternative to convex and Fresnel lens designs. The Buffon lens designed had the focusing ability of a convex lens using less material similarly to the Fresnel lens but with simpler manufacturing process. The lens was modelled in conjuction with a waveguide to create a compact design that could be accommodated in the space of a double glazing window for glass facades. The use of PMMA as the material of choice for both the lens and the waveguide, the overall system cost was kept to a minimum. The concept has potential advantages since besides the production of electricity it can be used to minimise building cooling loads and help reach the goal of self-sustained buildings.

Appendix A

List of Publications

1st Author Papers

A. Ioannides, T. N. D. Tibbits, J. P. Connolly, D. B. Bushnell, K. W. J. Barnham, C. Calder, G. Hill, J. S. Roberts, G. Smekens, and J. Van Begin, "Advances in strain balanced quantum well tandem solar cells," in *22nd EUPVSEC Proceedings, Milan*, pp. 210–213, 2007

A. Ioannides, T. N. D. Tibbits, J. P. Connolly, D. B. Bushnell, K. W. J. Barnham, C. Calder, G. Hill, J. S. Roberts, G. Smekens, and J. Van Begin, "Strain balanced quantum well monolithic tandem solar cells," in *21st EUPVSEC Proceedings, Dresden*, pp. 321–323, 2006

A. Ioannides, T. N. D. Tibbits, J. P. Connolly, K. W. J. Barnham, C. Calder, G. Hill, J. S. Roberts, and G. Smekens, "Strain balanced quantum well monolithic tandem solar cells," in *4th World Conference PV Energy Conversion Proceedings, Hawaii*, pp. 753–756, 2006

Co-Authored Papers

J. G. J. Adams, B. C. Browne, I. M. Ballard, J. P. Connolly, N. L. A. Chan, A. Ioannides, W. Elder, P. N. Stavrinou, K. W. J. Barnham, and N. J. Ekins-Daukes, "Recent results for single-junction and tandem quantum well solar cells," in *Progress in Photovoltaics: Research and Applications*, vol. 19, pp. 865–877, 2011

K. W. J. Barnham, I. M. Ballard, B. C. Browne, D. B. Bushnell, J. P. Connolly, N. J. Ekins-Daukes, M. Fuhrer, R. Ginige, G. Hill, A. Ioannides, D. C. Johnson, M. C. Lynch, M. Mazzer, J. S. Roberts, C. Rohr, and T. N. D. Tibbits, "Recent progress in quantum well solar cells," in *Nanotechnology for Photovoltaics* (L. Tsakalakos, ed.), ch. 5, pp. 187–210, CRC Press, 2010

B. C. Browne, N. J. Ekins-Daukes, A. Ioannides, J. P. Connolly, I. M. Ballard, K. W. J. Barnham, T. N. D. Tibbits, M. Pate, M. Geen, G. Hill, C. Calder, R. Airey, G. Smekens, J. Van Begin, and J. S. Roberts, "Dual Multiple Quantum Well Solar Cells," in *23rd EUPVSEC Proceedings, Valencia*, pp. 168–172, September 2008

B. C. Browne, A. Ioannides, J. P. Connolly, K. W. J. Barnham, J. S. Roberts, and R. Airey, "Tandem quantum well solar cells," in *Photovoltaic Specialists Conference Proceedings, 2008. PVSC '08. 33rd IEEE*, pp. 1–5, May 2008

I. M. Ballard, A. Ioannides, K. W. J. Barnham, J. P. Connolly, D. C. Johnson, M. Mazzer, and R. Ginige, "Quantum well solar cells for concentrator applications," in *22nd EUPVSEC Proceedings, Milan*, pp. 761–764, 2007

M. Mazzer, K. W. J. Barnham, I. M. Ballard, A. Bessiere, A. Ioannides, D. C. Johnson, M. C. Lynch, T. N. D. Tibbits, J. S. Roberts, G. Hill, and C. Calder, "Progress in quantum well solar cells," *Thin Solid Films*, vol. 511-512, pp. 76–83, 2006

Appendix B

Device Descriptions & Modelling Parameters

The devices reported in this thesis are listed below in rough chronological order of fabrication. All the details provided regarding device structure are as reported by the grower unless otherwise noted. The main modelling parameters for each device are also listed.

B.1 Preliminary Devices

The preliminary devices Qt1772AD and Qt1772AU have an MQW incorporated in the bottom cell intrinsic region. Devices Qt1772BD and Qt1772BU do not have an MQW structure incorporated in the bottom cell and are control devices. The top cell structure was not disclosed by ENE due to commercial confidentiality. The top cell structure shown in Tables B.1, B.3, B.5 and B.7 is the predicted top cell structure as used in SOL for fitting the experimental data.

Layer	Material	Thickness ($\AA$)	Dopant Type	Dopant	Dopant Conc. (cm^{-3})
Top Cell					
Cap	$Al_{0.594}GaAs$	300	p	unknown	2 x 10^{18}
Emitter	$In_{0.515}GaP$	3000	p	unknown	1 x 10^{18}
Base	$In_{0.515}GaP$	8200	n	unknown	2 x 10^{18}
Bottom Cell					
Cap	GaAs	200	p+	C	2 x 10^{19}
Window	$Al_{0.8}GaAs$	300	p+	C	2 x 10^{18}
Emitter	GaAs	5000	p	C	2 x 10^{18}
Intrinsic	GaAs	12850	-	-	-
Base	GaAs	30000	n	Si	2 x 10^{17}
Buffer	GaAs	3000	n	Si	1 x 10^{18}
Substrate	GaAs	-	n+	Si	-
Bottom Cell Quantum Well Structure					
No. of Wells			50		
Quantum Well	$In_{0.1}GaAs$	83	-	-	-
Barrier	$GaAsP_{0.089}$	174	-	-	-

Table B.1: Qt1772AD device structure.

Recombination velocity		
	Top Cell	**Bottom Cell**
Region	**Velocity (m/s)**	
window	0	-
emmiter	7000	0
base	2000	0
	Series Resistance (Ω)	**Parallel Resistance (Ω)**
Top Cell	10	1 x10^{12}
Bottom Cell	0	1 x10^{12}
Recombination time (ns)		
	Top Cell	**Bottom Cell**
i-hole	10	10
i-electron	8	10
well-hole	-	10
well-electron	-	10

Table B.2: Qt1772AD modelling parameters.

Layer	Material	Thickness ($\AA$)	Dopant Type	Dopant	Dopant Conc. (cm^{-3})
Top Cell					
Cap	$Al_{0.594}GaAs$	300	p	unknown	2 x 10^{18}
Emitter	$In_{0.515}GaP$	1500	p	unknown	1 x 10^{18}
Base	$In_{0.515}GaP$	4700	n	unknown	2 x 10^{18}
Bottom Cell					
Cap	GaAs	200	p+	C	2 x 10^{19}
Window	$Al_{0.8}GaAs$	300	p+	C	2 x 10^{18}
Emitter	GaAs	5000	p	C	2 x 10^{18}
Intrinsic	GaAs	12850	-	-	-
Base	GaAs	30000	n	Si	2 x 10^{17}
Buffer	GaAs	3000	n	Si	1 x 10^{18}
Substrate	GaAs	-	n+	Si	-
Bottom Cell Quantum Well Structure					
No. of Wells			50		
Quantum Well	$In_{0.1}GaAs$	83	-	-	-
Barrier	$GaAsP_{0.089}$	174	-	-	-

Table B.3: Qt1772AU device structure.

Recombination velocity		
	Top Cell	**Bottom Cell**
Region	**Velocity (m/s)**	
window	0	-
emmiter	0	4000
base	900	0
	Series Resistance (Ω)	**Parallel Resistance (Ω)**
Top Cell	10	1 x10^{12}
Bottom Cell	0	1 x10^{12}
Recombination time (ns)		
	Top Cell	**Bottom Cell**
i-hole	10	10
i-electron	8	10
well-hole	-	10
well-electron	-	10

Table B.4: Qt1772AU modelling parameters.

Layer	Material	Thickness ($\AA$)	Dopant Type	Dopant	Dopant Conc. (cm^{-3})
Top Cell					
Cap	$Al_{0.594}GaAs$	300	p	unknown	2 x 10^{18}
Emitter	$In_{0.515}GaP$	1500	p	unknown	1 x 10^{18}
Base	$In_{0.515}GaP$	4700	n	unknown	2 x 10^{18}
Bottom Cell					
Cap	GaAs	200	p+	C	2 x 10^{19}
Window	$Al_{0.8}GaAs$	300	p+	C	2 x 10^{18}
Emitter	GaAs	5000	p	C	2 x 10^{18}
Base	GaAs	30000	n	Si	2 x 10^{17}
Buffer	GaAs	3000	n	Si	1 x 10^{18}
Substrate	GaAs	-	n+	Si	-

Table B.5: Qt1772BD device structure.

Recombination velocity		
	Top Cell	**Bottom Cell**
Region	**Velocity (m/s)**	
window	0	-
emmiter	5000	0
base	1000	800
	Series Resistance (Ω)	**Parallel Resistance (Ω)**
Top Cell	10	1 x10^{12}
Bottom Cell	0	1 x10^{12}
Recombination time (ns)		
	Top Cell	**Bottom Cell**
i-hole	10	10
i-electron	8	10

Table B.6: Qt1772BD modelling parameters.

Layer	Material	Thickness ($\AA$)	Dopant Type	Dopant	Dopant Conc. (cm^{-3})
Top Cell					
Cap	$Al_{0.594}GaAs$	300	p	unknown	2 x 10^{18}
Emitter	$In_{0.515}GaP$	1500	p	unknown	1 x 10^{18}
Base	$In_{0.515}GaP$	4700	n	unknown	2 x 10^{18}
Bottom Cell					
Cap	GaAs	200	p+	C	2 x 10^{19}
Window	$Al_{0.8}GaAs$	300	p+	C	2 x 10^{18}
Emitter	GaAs	5000	p	C	2 x 10^{18}
Base	GaAs	30000	n	Si	2 x 10^{17}
Buffer	GaAs	3000	n	Si	1 x 10^{18}
Substrate	GaAs	-	n+	Si	-

Table B.7: Qt1772BU device structure.

Recombination velocity		
	Top Cell	**Bottom Cell**
Region	**Velocity (m/s)**	
window	0	-
emmiter	5000	0
base	1000	800
	Series Resistance (Ω)	**Parallel Resistance (Ω)**
Top Cell	10	1 x10^{12}
Bottom Cell	0	1 x10^{12}
Recombination time (ns)		
	Top Cell	**Bottom Cell**
i-hole	10	10
i-electron	8	10

Table B.8: Qt1772BU modelling parameters.

B.2 MQW Tandem Solar Cells

The following devices consist of an MQW bottom cell grown at Sheffield and a top cell overgrowth performed at ENE. The exact growth details of the top cell were not disclosed thus the top cell device structure shown are the modelling parameters used for each device.

Layer	**Material**	**Thickness** ($\AA$)	**Dopant Type**	**Dopant**	**Dopant Conc.** ($\mathbf{cm^{-3}}$)
Top Cell					
Window	$Al_(0.8)GaAs$	300	p+	unknown	2 x 10^{18}
Emitter	$In_{0.485}GaP$	5000	p	unknown	1 x 10^{18}
Intrinsic region	$In_{0.485}GaP$	1300	-	-	-
Base	$In_{0.485}GaP$	5200	n	unknown	2 x 10^{18}
Bottom Cell					
Window	$Al_{0.8}GaAs$	300	p+	C	3 x 10^{18}
Emitter	GaAs	5000	p	C	5 x 10^{18}
Intrinsic	GaAs	12850	-	-	-
Base	GaAs	30000	n	Si	2 x 10^{17}
Buffer	GaAs	3000	n	Si	1 x 10^{18}
Substrate	GaAs	-	n+	Si	-
Bottom Cell Quantum Well Structure					
No. of Wells			50		
Quantum Well	$In_{0.11}GaAs$	83	-	-	-
Barrier	$GaAsP_{0.089}$	174	-	-	-

Table B.9: Qt1808U device structure.

Recombination velocity		
	Top Cell	**Bottom Cell**
Region	**Velocity (m/s)**	
window	0	3000
emmiter	0	2000
base	4000	0
	Series Resistance (Ω)	**Parallel Resistance (Ω)**
Top Cell	10	1 x10^{12}
Bottom Cell	5	1 x10^{10}
Recombination time (ns)		
	Top Cell	**Bottom Cell**
i-hole	8	10
i-electron	8	10
well-hole	-	10
well-electron	-	10

Table B.10: Qt1808U modelling parameters.

Layer	**Material**	**Thickness ($\AA$)**	**Dopant Type**	**Dopant**	**Dopant Conc. (cm^{-3})**
Top Cell					
Window	$Al_(0.65)GaAs$	300	p+	unknown	2 x 10^{18}
Emitter	$In_{0.48}GaP$	1000	p	unknown	1 x 10^{18}
Intrinsic region	$In_{0.48}GaP$	3400	-	-	-
Base	$In_{0.48}GaP$	5700	n	unknown	2 x 10^{18}
Bottom Cell					
Window	$Al_{0.8}GaAs$	300	p+	C	2 x 10^{17}
Emitter	GaAs	5000	p	C	2 x 10^{17}
Intrinsic	GaAs	20560	-	-	-
Base	GaAs	35000	n	Si	1 x 10^{18}
Buffer	GaAs	3000	n	Si	1 x 10^{18}
Substrate	GaAs	-	n+	Si	-
Bottom Cell Quantum Well Structure					
No. of Wells			50		
Quantum Well	$In_{0.125}GaAs$	83	-	-	-
Barrier	$GaAsP_{0.089}$	174	-	-	-

Table B.11: Qt1821AD device structure.

Recombination velocity		
	Top Cell	**Bottom Cell**
Region	**Velocity (m/s)**	
window	0	0
emmiter	0	0
base	5000	0
	Series Resistance (Ω)	**Parallel Resistance (Ω)**
Top Cell	0	1 x10^{12}
Bottom Cell	15	4.5 x10^{9}
Recombination time (ns)		
	Top Cell	**Bottom Cell**
i-hole	5	5
i-electron	5	5
well-hole	-	5
well-electron	-	5

Table B.12: Qt1821AD modelling parameters.

Layer	**Material**	**Thickness ($\AA$)**	**Dopant Type**	**Dopant**	**Dopant Conc. (cm^{-3})**
Top Cell					
Window	Al(0.594)GaAs	300	p+	unknown	2 x 10^{18}
Emitter	$In_{0.48}GaP$	1000	p	unknown	1 x 10^{18}
Intrinsic region	$In_{0.48}GaP$	3400	-	-	-
Base	$In_{0.48}GaP$	5700	n	unknown	2 x 10^{18}
Bottom Cell					
Window	$Al_{0.8}GaAs$	300	p+	C	2 x 10^{17}
Emitter	GaAs	5000	p	C	2 x 10^{17}
Intrinsic	GaAs	20560	-	-	-
Base	GaAs	35000	n	Si	1 x 10^{18}
Buffer	GaAs	3000	n	Si	1 x 10^{18}
Substrate	GaAs	-	n+	Si	-
Bottom Cell Quantum Well Structure					
No. of Wells			50		
Quantum Well	$In_{0.11}GaAs$	83	-	-	-
Barrier	$GaAsP_{0.089}$	174	-	-	-

Table B.13: TS151 device structure.

Recombination velocity		
	Top Cell	**Bottom Cell**
Region	**Velocity (m/s)**	
window	0	0
emmiter	15000	20
base	5000	20

	Series Resistance (Ω)	**Parallel Resistance (Ω)**
Top Cell	1	3 x10^{9}
Bottom Cell	5	1 x10^{10}

Recombination time (ns)		
	Top Cell	**Bottom Cell**
i-hole	1	10
i-electron	1	10
well-hole	-	10
well-electron	-	10

Table B.14: TS151 modelling parameters.

B.3 Control Devices

Two control devices were grown by ENE. The devices were grown on a germanium substrate. Device ENE1864.1 top cell was grown with device TS151 as a control cell. The device structures shown are the deduced structure from the device modelling as the growth details were not available.

Layer	**Material**	**Thickness** ($\AA$)	**Dopant Type**	**Dopant**	**Dopant Conc.** ($\mathbf{cm^{-3}}$)
Top Cell					
Window	$Al_(0.594)GaAs$	430	p+	unknown	2.3 x 10^{18}
Emitter	$InGa_{0.46}As$	1000	p	unknown	1 x 10^{18}
Intrinsic region	$InGa_{0.46}P$	2000	-	-	-
Base	$InGa_{0.46}As$	5700	n	unknown	1.8 x 10^{17}
Bottom Cell					
Window	$Al_{0.8}GaAs$	430	p+	unknown	2 .3x 10^{18}
Emitter	$Al_{0.1}GaAs$	2000	p	unknown	2.3 x 10^{18}
Base	$Al_{0.1}GaAs$	50000	n	unknown	3 x 10^{17}
Substrate	Ge	-	n+	unknown	-

Table B.15: ENE1595.4 device structure.

Recombination velocity		
	Top Cell	**Bottom Cell**
Region	**Velocity (m/s)**	
window	1000	2000
emmiter	1000	0
base	5000	0
	Series Resistance (Ω)	**Parallel Resistance (Ω)**
Top Cell	1	3 x10^{12}
Bottom Cell	5	3 x10^{12}
Recombination time (ns)		
	Top Cell	**Bottom Cell**
i-hole	1	10
i-electron	1	10

Table B.16: ENE1595.4 modelling parameters.

Layer	**Material**	**Thickness ($\AA$)**	**Dopant Type**	**Dopant**	**Dopant Conc. (cm^{-3})**
Top Cell					
Window	Al$_{(}$0.594)GaAs	400	p+	unknown	2 x 10^{18}
Emitter	InGa$_{0.47}$As	1000	p	unknown	1 x 10^{19}
Intrinsic region	InGa$_{0.47}$P	2000	-	-	-
Base	InGa$_{0.46}$As	5700	n	unknown	2 x 10^{18}
Bottom Cell					
Window	Al$_{0.7}$GaAs	300	p+	unknown	2 .3x 10^{18}
Emitter	GaAs	5000	p	unknown	2.3 x 10^{18}
Intrinsic	GaAs	4000	-	-	-
Base	GaAs	20000	n	unknown	3 x 10^{17}
Substrate	Ge	-	n+	unknown	-

Table B.17: ENE1864 device structure.

Recombination velocity		
	Top Cell	**Bottom Cell**
Region	**Velocity (m/s)**	
window	5000	0
emmiter	1000	2000
base	0	0
	Series Resistance (Ω)	**Parallel Resistance (Ω)**
Top Cell	0	1 x10^{12}
Bottom Cell	0.5	1 x10^{12}
Recombination time (ns)		
	Top Cell	**Bottom Cell**
i-hole	1	1
i-electron	1	1

Table B.18: ENE1864 modelling parameters.

B.4 Top Cell only Devices

Device TS131 was grown at Sheffield using the Thomas Swan MOCVD machine. Up to that time it was not possible to grow InGaP devices with the existing equipment. Future monolithic tandem grown was depending on the success of this attempt.

Layer	**Material**	**Thickness** ($\AA$)	**Dopant Type**	**Dopant**	**Dopant Conc.** (cm^{-3})
Top Cell					
Window	Al$_{(}$0.594)GaAs	300	p+	unknown	2 x 10^{18}
Emitter	$In_{0.48}GaP$	1000	p	unknown	1 x 10^{18}
Intrinsic region	$In_{0.48}GaP$	3400	-	-	-
Base	$In_{0.48}GaP$	5700	n	unknown	2 x 10^{17}
Substrate	GaAs	-	n+	Si	-

Table B.19: TS131 device structure.

Recombination velocity	
Region	**Velocity (m/s)**
window	0
emmiter	1000
base	5000
Series Resistance (Ω)	**Parallel Resistance** (Ω)
1	3 x10^{9}
Recombination time (ns)	
i-hole	3
i-electron	3

Table B.20: TS131 modelling parameters.